

461420
217 8991
TA class 1890

**ACOUSTIC MEASUREMENTS ON REAL AND
SYNTHETIC RESERVOIR ROCK**

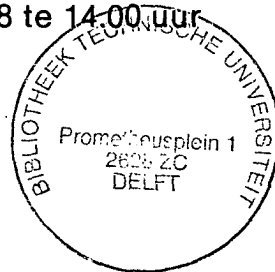
ISBN 90-9002609-6
Druk: ALEVO - Delft

ACOUSTIC MEASUREMENTS ON REAL AND SYNTHETIC RESERVOIR ROCK

PROEFSCHRIFT

ter verkrijging van de graad van doctor aan de
Technische Universiteit Delft, op gezag van de
Rector Magnificus, prof. drs. P.A. Schenck,
in het openbaar te verdedigen ten overstaan van
een commissie aangewezen door het College van Dekanen
op dinsdag 13 december 1988 te 14.00 uur

door



Rudolf Visser
mijnbouwkundig ingenieur
geboren te Zeist

TR diss
1690

Dit proefschrift is goedgekeurd

door de promotoren:

Prof. ir. J.J. van der Vuurst de Vries

en

Prof. A.M. Ziolkowski M.A., Ph.D., MSc (Econ.)

7. In zijn behandeling van de Welge constructie toont Dake niet aan waarom de op deze wijze verkregen saturatieverdeling (van belang voor de berekening van de waterdoorbraaktijd bij olieverdringing), uniek is bepaald.
(L.P. Dake, Fundamentals of reservoir engineering, Amsterdam (etc), Elseviers Scientific Publ. Cy., 1978, pp 360 en 361)
8. Dat bezuinigingen in de monumentenzorg bij de restauratie van een bouwwerk de weegschaal doen doorslaan naar consolidatie in plaats van reconstructie, is waarschijnlijk het enige positieve gevolg ervan.
9. Catalogusautomatisering veroorzaakt in vele bibliotheken een verschraling van de informatieontsluiting, al dan niet van tijdelijke aard.
10. Het duidelijke verband dat er bestaat tussen de kleigrond en het voorkomen van romaanse kerken in Friesland, toont aan dat, niettegenstaande de nadelige gevolgen voor kleiige oliereservoirs, de aanwezigheid van klei ook positieve kanten heeft.

Stellingen

behorende bij het proefschrift van R.Visser.

1. Het zonder meer overnemen van de eigenschappen van nabijgelegen kleilagen bij de petrofysische evaluatie van een kleihoudend reservoir, zou, gezien mogelijke verschillen in mineralogie en ook distributie van de kleien, met meer terughoudendheid moeten geschieden.
(dit proefschrift,
R. Visser, K.A.T. Bours and J.P. van Baaren, Effective porosity estimation in the presence of dispersed clay, presented at SPWLA 29th Ann. Log. Symp., San Antonio, 1988.)
2. Het toetsen van uit log-waarden verkregen formatie-eigenschappen aan gemeten kernwaarden, draagt in hoge mate bij aan de betrouwbaarheid van de petrofysische evaluatie.
3. Als de servicemaatschappijen meer openheid zouden betrachten omtrent de condities waaronder de door hen gepresenteerde gegevens zijn verkregen, zou dit een efficiënte verwerking van deze gegevens ten goede komen.
4. Bij het bepalen van de porositeit van cilindervormige gesteente-monsters bestaande uit grote korrels, dient men terdege rekening te houden met de oppervlakte/volume verhouding van het monster i.v.m. eventuele aan het oppervlak optredende verstoringen in de korrel-structuur.
5. Het ondergronds opslaan van radio-actief afval, zelfs in daartoe minder geschikte geologische formaties dan steenzout, is veruit te prefereren boven langdurige bovengrondse opslag.
6. In laag-permeabele reservoirs met slecht verbonden poriën, verdient het de voorkeur de porositeit te meten m.b.v. de Boyle-methode in plaats van de wet-and-dry-weight methode.
(dit proefschrift)

voor mijn vader

Contents

LIST OF SYMBOLS	7
I. INTRODUCTION	
I.1 General introduction	11
I.2 Description of the project	12
I.3 Outline of this thesis	14
II. FIELD EXAMPLES ACOUSTIC WAVETRAIN LOGGING	
II.1 Introduction	17
II.2 Acoustic logging	18
II.3 Shaly sandstone formation	20
II.3.1 Petrophysical evaluation	20
II.3.2 Wavetrain interpretation	29
II.4 Dolomite formation	42
II.4.1 Petrophysical evaluation	42
II.4.2 Wavetrain interpretation	44
II.5 Discussion of results	46
III. ARTIFICIAL SANDSTONE	
III.1 Introduction	49
III.2 Review of synthetic cores	50
III.3 Sample requirements	53
III.4 Chemical aspects of the consolidation methods	54
III.5 Sample construction	57
III.5.1 Compaction of the grains	58
III.5.2 Drainage of the sandpack	59
III.5.3 Consolidation methods	61
III.5.4 Selection of sand	65

III.6	Sample description	66
III.7	Irregularities in the samples using Silica-lock	74
III.7.1	Description of the irregularities	75
III.7.2	Possible causes of fracturing	77
III.7.3	Attempts to reduce the effect of expansion of the sample during consolidation	81
III.7.4	Attempts to reduce the effect of shrinkage of the cement	83
III.7.5	Conclusion	86
III.8	Sample properties	87
III.9	Comparison of artificial samples with natural rock	93
IV. MODELLING OF ACOUSTIC WAVETRAINS		
IV.1	Introduction	96
IV.2	Wave propagation in porous media	97
IV.2.1	Biot theory	99
IV.2.2	Formation parameters	101
IV.3	Modelling of acoustic waves in a liquid/porous solid configuration with a flat boundary	104
IV.3.1	Configuration	105
IV.3.2	Wave equations	106
IV.3.3	Pressure response in the fluid	108
IV.3.4	Incident field	109
IV.3.5	Reflected field: full frequency range	111
IV.3.6	Numerical considerations	113
IV.3.7	Reflected field: high frequency limit	116
IV.3.8	The convolutions	119
IV.3.9	Numerical results	122
V. ACOUSTIC MEASUREMENTS		
V.1	Introduction	129
V.2	Data acquisition system	130
V.3	Transmission measurements	134
V.3.1	Description of the experiments	134
V.3.2	Velocity determination	137
V.3.3	Attenuation determination	141
V.3.4	Accuracy	144

V.4	Refraction measurements	145
V.4.1	Configuration	146
V.4.2	Optimisation of the measurements	147
V.5	Measurement results	148
V.5.1	Samples	148
V.5.2	Results	150
V.5.3.	Modelling	156
V.6	Summary of results	159
VI.	CONCLUSIONS	161
	RECOMMENDATIONS	163
	REFERENCES	165

Appendices

A.	Biot theory; numerical description	168
B.	Fourier transforms	172
C.	Calculation of reflection coefficient	173
D.	Transducer characteristics	181
	SUMMARY	185
	SAMENVATTING	187
	NAWOORD	189
	CURRICULUM VITAE	191

List of symbols

α, β	horizontal Fourier transform parameters	(s/m)
$\alpha(\omega)$	attenuation coefficient	(1/m)
$\epsilon, \epsilon(\omega)$	tortuosity	
γ	vertical propagation coefficient	(s/m)
δ	structural factor (Biot)	
δ_{ij}	Kronecker delta	
η	viscosity	(kg/msec)
λ	wavelength	(m)
ϕ	porosity	(fr. BV)
ϕ_t	total porosity	(fr. BV)
ϕ_{eff}	effective porosity	(fr. BV)
ϕ_N	neutron porosity	(lms ^t p.u.)
Φ_v	volume density of injected fluid volume	
$\phi_v(t)$	volume injection function	(m ³)
ρ	density	(kg/m ³)
$\rho_{11}, \rho_{12}, \rho_{22}$	mass coefficients (Biot)	(kg/m ³)
σ_{ij}	average stress in solid part of porous medium	(N/m ²)
ω	frequency	(rad/sec)
$\kappa, \lambda, \xi, \psi$	transform parameters	
∇	$\frac{\partial}{\partial x} \frac{i}{x} + \frac{\partial}{\partial y} \frac{i}{y} + \frac{\partial}{\partial z} \frac{i}{z}$	
B_{cp}	compaction factor (Wyllie equation)	
$bF(\omega)$	damping factor (Biot)	(kg/m ³ s)
D_{dom}	dominant grain size	(micron)
D_{50}	medium grainsize at 50 % cum. weight fraction	(micron)
$G(t)$	Green's function, response to a step in the rate of change of volume injection	(1/m)
$G'(t)$	Green's function, response to an impulse in the rate of change of volume injection	(1/ms)
$HI_{cl\ dry}$	hydrogen index of dry clay fraction	
J_0	zero order Bessel function	
K_b	bulk modulus of skeleton	(N/m ²)
K_f	bulk modulus of fluid part of porous medium	(N/m ²)
K_s	bulk modulus of composite	(N/m ²)
K_L	bulk modulus of half-space filled with liquid	(N/m ²)

N	shear modulus of porous medium	(N/m ²)
P,Q,R	elastic parameters (Biot)	(N/m ²)
P	pressure	(N/m ²)
Q	quality factor	
R _L	reflection coefficient for the relected wave	
R _O	resistivity of formation 100 % saturated with water	(Ohmm)
R _w	resistivity of formation water	(Ohmm)
S	average stress in fluid part of porous medium	(N/m ²)
S _h	hydrocarbon saturation	(fr. PV)
S _O	trask sorting	
S _w	water saturation	(fr. PV)
S _{wirr}	irreducible water saturation	(fr. PV)
T	surface permeability	
T _{arr}	arrival time	(sec)
T ₊ , T ₋ , T _S	transmission coefficients	
<u>U</u>	particle displacement in fluid part of rock	(m)
V	velocity	(m/s)
V _{sh}	shaliness	(fr. BV)
d, trs	horizontal distance transmitter - receiver	(m)
f	frequency	(Hz)
h	thickness	(m)
h _r , z _r	height above interface of receiver	(m)
h _t , z _t	height above interface of transmitter	(m)
k	permeability	(m ²)
m	cementation factor	
s	Laplace transform parameter	(1/s)
t	time	(sec)
Δt	interval transit time	(μsec/ft)
<u>u</u>	particle displacement in solid part of rock	(m)
x,y,z	carthesian coordinates	
r,θ	polar coordinates	

Superscripts

- i → incident field
- r → reflected field

Subscripts

+, p	→	fast compressional wave
-, psl	→	slow compressional wave
b	→	bulk
L	→	half-space filled with liquid
Lmst	→	limestone
Sst	→	sandstone
c	→	compressional wave
fl	→	fluid in the pores
ma	→	matrix
s	→	shear wave
sh	→	shale
t	→	time

I. INTRODUCTION

I.1 General introduction

Information on subsurface layers is commonly obtained by borehole measurements. The measurements are performed by logging tools which are lowered into the hole. When pulled up again, the tools record certain physical quantities of the surrounding formations at very small depth intervals. A continuous display of these recordings is called a log.

Logs are run in almost every well drilled. The costs associated with logging are large: they make up 5 - 10 % of the total well costs.

The logs are used to determine the petrophysical properties of the formations of interest. Some ten different logs are run in one borehole, such as Gamma Ray, resistivity, nuclear and acoustic logs. Each one is related to a different physical property of the rock. However, not every possible information on rock parameters can be obtained at present. Especially the acoustic behaviour of rocks is under-utilized in formation evaluation although it shows great potential for giving additional information on many rock parameters.

Acoustic behaviour of rocks is studied by way of acoustic logging tools. The tools send out acoustic pulses, which are picked up again after they have travelled several feet along the borehole through the formation. Acoustic logs are run in two versions: the standard "Sonic" or "Acousti"-log and the full waveform log. The sonic or acoustilog records only the arrival time of the fastest compressional wave returning at the receiver. The full waveform log records the total acoustic trace returning at the receiver.

Since its introduction in the early 1960's, the sonic log has been widely used as a porosity indicator. It is also employed to calibrate seismic reflection data and to obtain a qualitative indication of the mechanical rock properties, e.g. rock strength. The amplitude of the compressional wave is also used to obtain an indication of the quality of the cementbond in cased boreholes. Recent publications suggest the application of acoustic logs in the interpretation of fractured reservoirs (Liu, 1986, Brie et al., 1988).

The second version of the acoustic logs, the full waveform log, records a much larger data set. At certain depth increments it records all acoustic waves propagating along the borehole in time as well as in amplitude. Each of these waves gathers information about the reservoir on its way, so the total wavetrain package reflects the acoustic characteristics of the formation through which it has travelled.

A proper interpretation procedure therefore could provide accurate quantitative estimates of several reservoir parameters, among others: values of total and effective porosity, lithology, rock strength and even permeability. But despite the promising potential, the full wavetrain is hardly used in formation evaluation because it is very difficult to extract the information from the recorded wavetrains. And despite large efforts made by many people in recent years, the interpretation of the wavetrains has not reached the commercial application stage.

The reason for this is found in the complexities of the received wavetrain and the reservoirs to be evaluated. The presence of mudcake, irregular borehole diameter, mud invading into the formation, etc., all influence the recorded wavetrains to such an extent that the contribution of a number of rock parameters is not clear. Furthermore, almost any two rock samples obtained from cores or outcrops will differ in more than one aspect. An empirical approach to study the acoustic behaviour by comparing field data, thus encounters large difficulties in the assignment of a difference in acoustic response to one single rock property. At best, a broad, general trend can be found.

I.2 Description of the project

To overcome these problems, a laboratory study was started at the faculty of Mining and Petroleum Engineering at Delft University of Technology in 1983. The project was supported financially by the European Economic Community under contract number TH/01.35/83.

The project is called "Acoustic measurements on reservoir rock" and aims at improving the interpretation of the wavetrains in the broadest sense.

For the project an empirical way is adapted to obtain its goal, whereby acoustic measurements are performed on a range of rock samples, differing in one aspect only. The difference in acoustic response of the samples then is linked to that specific rock property. The experiments are performed under both atmospheric and in-situ conditions.

The empirical approach requires that the properties of each sample are fully known and that many samples are available, which differ in one property only. Such a range of samples can hardly be found from natural rocks. It was therefore decided to construct and use artificial rocks instead. Of course, these artificial rock samples have to exhibit characteristics similar to natural reservoir rocks to enable the results to be extrapolated to real logs. Construction of such synthetic sandstone rock samples constitutes a fundamental part of the project. Simultaneously the theoretical aspects of the projects were studied and the required research facilities were designed.

The objectives of the project can be listed as follows:

- 1) Development of a theoretical model to predict and interpret the measured acoustic signals.
- 2) Development of a procedure to construct suitable artificial rock samples.
- 3) Measuring microseismograms at atmospheric and in-situ conditions on a range of natural and synthetic rock samples with varying properties.
- 4) Optimizing the measurement and evaluation technique of the acoustic wavetrain experiments.
- 5) Linking the acoustic responses to the sample properties.
- 6) Applying the results of this study to field data and obtain rock properties from the wavetrains, such as permeability, different types of porosity and mechanical rock strength.

To achieve these objectives, the following research facilities had to be designed:

- 1) A measurement system for atmospheric experiments.
- 2) A high pressure/high temperature cell, a so-called borehole simulator.

To realize all these objectives, the total project was split into two parts. The first part covered the design and construction of the research facilities, field examples, the theoretical modelling and

initiated the measurements on synthetic rock samples under atmospheric conditions. It was rounded off successfully in January 1988. The second part was started in Oct. 1988 and will continue the measurements under atmospheric conditions, the measurements under in-situ conditions on natural and synthetic rock samples and the application of the results to field data.

1.3 Outline of this thesis

As the title already suggests, this thesis covers most of the work on the first part of the project. The design and construction of the borehole simulator fall outside the scope of this paper.

The present study investigates field data from boreholes, obtained from commercial full waveform logs, as well as laboratory measurements on synthetic rock samples. The term "reservoir rock" as used in the title of this thesis, therefore has to be seen in the broadest sense. It refers to natural reservoir formations as well as artificially created rock samples. The thesis also includes the theoretical aspects of the project and a thorough study into the construction of artificial rock samples. The separate topics of the project are reflected in the layout of this thesis. Each chapter is devoted to one subject and together they give a detailed account of the work carried out so far on the project. The current chapter gives a general introduction to the present study and states the objectives.

Chapter two presents the results of two field studies. Two wells were studied in which a full waveform log was run. One well is drilled in a shaly sandstone reservoir, the other penetrates a dolomite formation. An extensive petrophysical evaluation was carried out to describe both reservoirs in detail. The standard petrophysical methods failed to account correctly for the shale fraction in the sandstone reservoir, so a special evaluation procedure was developed to give a proper description of this formation. An attempt was made to correlate the recorded wavetrains with the petrophysical description. The results of this correlation are given and the limitations of the study on acoustic behaviour using natural reservoir rocks are discussed.

Chapter three treats the construction of the artificial rock samples needed for the acoustic experiments. Three different methods to produce synthetic samples, are discussed. The problems encountered during the processes and their solutions, are treated extensively. The general properties of the resulting samples are given. The chapter ends with a comparison between the artificial samples and natural rocks.

Chapter four comprises the theoretical aspects of the project. Theoretical models which predict the acoustic signals that will be recorded in the experiments, are developed and acoustic time-pressure traces are calculated for a configuration similar to our measurement set-up. As a basis for the models, the Biot theory of propagation of acoustic waves in porous media is used. The influence of several rock parameters upon the recorded wavetrains is investigated. A parameter study is performed to determine the optimum measurement configuration. Chapter five reports on the acoustic experiments. It combines the results of all previous chapters. The measurements on artificial samples and the system itself are described. The acoustic responses are correlated with the sample properties and compared with the theoretical predictions.

The thesis ends with a listing of the conclusions drawn from the present study. Recommendations for the follow-up project are given.

II. FIELD EXAMPLES ACOUSTIC WAVETRAIN LOGGING

II.1 Introduction

In this chapter the application of acoustic wavetrains to formation evaluation is investigated in two field examples. The field examples clearly indicate the limitations of using natural reservoir formations for acoustic research.

Two wells are studied, drilled in different reservoir formations. Both formations are gas bearing but the lithology is completely different. One formation is a shaly sandstone while the other is a tight dolomite reservoir.

Both wells were drilled in the early 1980's. A complete set of logs was run and both formations were completely cored with a recovery of almost 100 per cent. Core measurements were available to check the results calculated from the logs.

Prior to the interpretation of the wavetrain data an extensive petrophysical evaluation was made of each of the two wells in order to characterize the logged formations in detail. In the case of the shaly sandstone reservoir a special log analysis procedure had to be used to evaluate the formation properly, because a problem was encountered regarding the shale fraction present in the formation. The mineralogy of the shale fraction was not constant over the reservoir interval. This influenced the log response of the shale fraction and the standard evaluation procedure did not result in an accurate reservoir description. Therefore, a new evaluation method had to be developed to properly define the properties of the shale fraction within each subinterval of the reservoir. This work was presented at the 26th Annual Logging Symposium of the Society of Professional Well Log Analysts in Dallas, June 1985 (Visser and van Baaren, 1985).

In the following, a short description of the acoustic logging in the example wells is presented first. Then the two investigated wells are discussed separately.

II.2 Acoustic logging

Measurement configuration

The acoustic wavetrains were recorded in the two field examples with a "long-spaced" sonic sonde. The tool contains two pairs of transducers separated by a distance of 8 feet.

The transducers of each pair are spaced 2 feet apart (Fig 2.1).

In the two field examples four different modes were recorded with transmitter-receiver spacings of respectively 10, 8, 12 and 10 feet. The acoustic signals of mode 1 and 4 have travelled the same distance through the formation (10 feet) and should therefore be identical, which provides a measure of the consistency of the log readings.

A wavetrain was recorded every 6 inches in depth as the tool was pulled along the formations.

Each recorded mode is displayed in a "Variable Density Log", fig 2.2. In

this log black bands correspond to positive amplitudes, white bands to negative. The magnitude of the amplitudes is represented by varying shades of grey.

Borehole compensation

The data represented in the logs are direct recordings. They have been influenced by various environmental effects, such as mud, mudcake, borehole rugosity, fractures, tilting of the sonde etc. Most of these effects can be eliminated by applying a so-called borehole compensation procedure. Since only four mode recordings were available for the field examples, the borehole compensation has been carried out as illustrated in fig. 2.1. The arrival times of a wave in two different mode recordings were subtracted. This resulted in an interval transit time over a formation interval of 2 feet corresponding to the fat lines in fig 2.1. The four modes of recording thus determined three interval transit

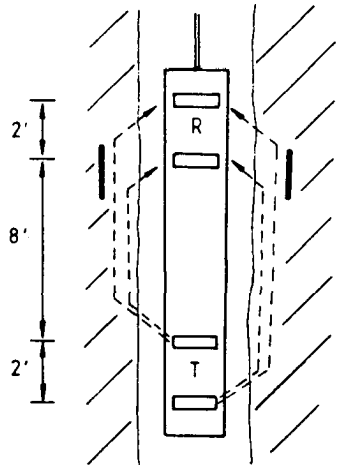


Fig 2.1
Acoustic logging sonde

times, each one recorded with the tool in a different location in the borehole. These times were averaged.

No procedure exists that will compensate the amplitudes of the recorded acoustic traces. Besides containing possible information about the reservoir, the amplitudes of the measured waves will be affected too by the previously listed environmental effects.

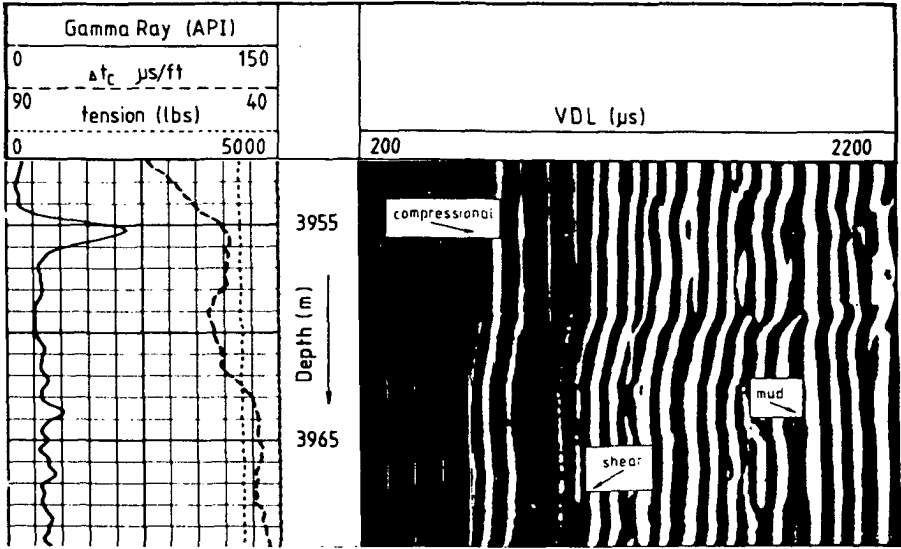


Fig 2.2 Variable density display of the recorded wavetrains. At the left, the Gamma Ray log is displayed together with the borehole compensated transit time of the compressional wave.

The shear and compressional wave arrival times used in the field examples have been handpicked from the variable density log. A borehole compensation has been applied to the data as outlined above. The resulting interval transit times of the compressional waves correlate well with the values obtained by the standard BHC Sonic in an independent logging run.

II.3 Shaly sandstone formation

The first field example is a shaly sandstone reservoir which has a rather complex lithology. Mixtures of clay minerals in various proportions are present in the formation. The standard evaluation procedures cannot distinguish between these mixtures and a special procedure had to be devised to obtain an accurate reservoir description.

Since a detailed knowledge of the formation is essential to interpret the recorded wavetrains correctly, the petrophysical evaluation of the well is discussed here extensively. The consequences for the wavetrain interpretation are given in the next section.

II.3.1 Petrophysical evaluation

Description of the reservoir

The formation is a gas-bearing, calcareous shaly sandstone. The reservoir interval is 19 m., which has been completely cored with a recovery of almost 100 percent. There is no gas-water contact present in the well under consideration.

The formation has been deposited in a shallow marine environment which slowly changes into a deeper marine sediment. The sand contains upwards gradually more clay particles and clay streaks until the deposit passes into shales which form the caprock. The average amount of shale present is approximately 25 percent BV (bulk volume). At the time of deposition strong bioturbation took place and the initial thin sequences of sand and shale were thoroughly mixed. Consequently, the shale fraction is present in thin laminae as well as dispersed throughout the pore space of the reservoir.

The total porosity encountered in the well ranges from 10 to 21 percent BV. The watersaturation in the flushed zone is approximately 70 % .

Several thin bands of calcareous conglomerates occur in the formation. They consist of material eroded from nearby highs. Probably due to this influx of foreign material, the properties of the shale fraction in the formation are not constant. In every formation subinterval the shale fraction appears to be characterized by a different set of log values.

Statement of the problem

Before the log recordings of the reservoir can be interpreted in terms of porosity and lithology, they have to be corrected for the influence of the shale fraction present in the formation. For this correction it is usually assumed in well log analysis that the shale fraction within the reservoir possesses the same characteristics as nearby thick shale layers. This implies that the log values recorded opposite overlying shale layers can be used to correct the log values in the reservoir itself.

But in this particular sandstone formation this approach is not appropriate. The shale layers forming the caprock just above the reservoir show a wide range in recorded log values and it is not possible to derive the shale properties appropriate for the reservoir section.

The extreme values recorded opposite these shales are for the different logs:

Gamma Ray (°API)	CNL (p.u.)	FDC (g/cc)	Sonic (µs/ft)
100	20	2.51	95
114	41.5	2.40	115

The variation in the log values opposite the shales is illustrated in fig 2.3. It is a crossplot of density (FDC) versus neutron porosity (CNL).

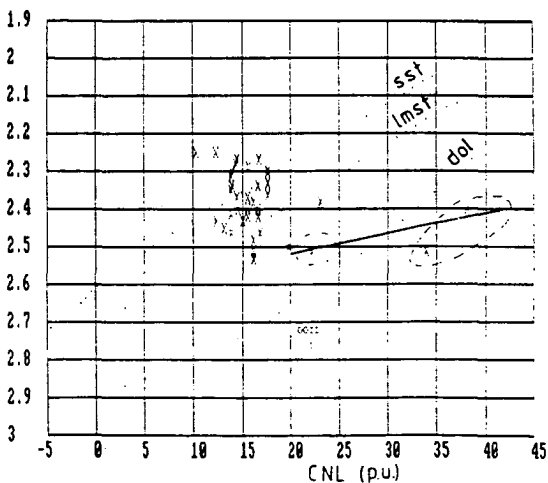


Fig 2.3
Density-Neutron crossplot.
Log values are squared and multiplexed.
Shale layers are encircled.
Dashed lines refer to pure lithologies, i.e.:
sst = sandstone
lmst = limestone
dol = dolomite

All log values recorded over the total reservoir interval including the caprock, are plotted. The logs have been squared and multiplexed, but otherwise not corrected. The log readings opposite the caprock are encircled. The plot shows clearly the impossibility to establish the 100 % shale point unambiguously.

Furthermore, the use of one specific shale point in the evaluation does not give satisfactory results as shown in fig 2.4. The crossplot shows the volume percentage sandstone derived from two combinations of two logs: the density and neutron logs on one hand and the neutron and sonic logs on the other. The rock matrix is assumed to consist of a combination of sandstone and limestone (based on the core description). The log values used to construct this plot were corrected for the influence of shale using the average properties of the caprock. The two combinations of logs do not provide the same results when compared layer by layer. Each combination more or less indicates a sandstone containing some limestone, but they do not agree with each other.

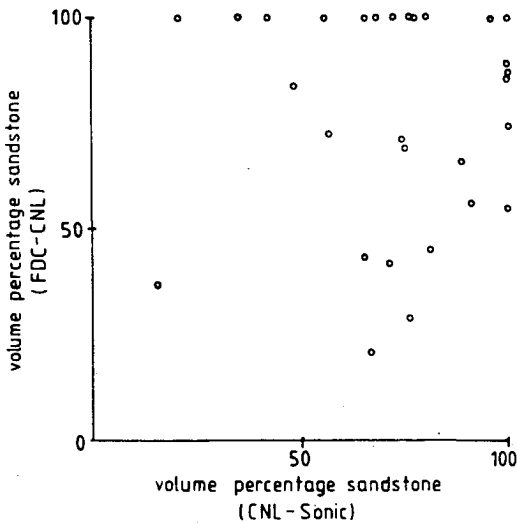


Fig 2.4
Vol. percentage sandstone derived from the combined density and neutron logs versus vol. percentage sandstone derived from neutron and sonic logs. Logs were corrected for shale using the average log readings opposite the caprock, (i.e. one shale point).

If another 100 % shale point is chosen from the observed range, the correlation between the two log combinations does not improve significantly. The wide scatter in the plot remains, only this time other sub-intervals of the reservoir correlate well. This points to the fact that different shale points should be used to correct different subintervals

of the reservoir for shale, to obtain a maximum correlation between the rock composition derived from Density/Neutron and from Neutron/Sonic log combinations. In other words: the type of shale present in the reservoir is not the same for each subinterval.

Evaluation procedure

If the shale point is not unique for the whole reservoir section, the question arises: "Which shale point is valid for which reservoir subinterval?". Unfortunately, a GammaRay Spectrolog which could provide information about this, was not run in this well. Therefore the shale properties had to be extracted from the existing logs. This was achieved by matching the porosity and lithology obtained from the FDC-CNL and Sonic-CNL crossplots for each layer by way of adjusting the 100 % wet shale properties (Visser and van Baaren, 1985).

The evaluation method can be expressed in the following mathematical form. The responses of the FDC, CNL and Sonic logs are given by:

$$\rho_b = \phi \rho_{f1} + V_{sst} \rho_{sst} + V_{lmst} \rho_{lmst} + V_{sh} \rho_{sh} \quad (2.1)$$

$$\phi_N = \phi \phi_{Nf1} + V_{sst} \phi_{Nsst} + V_{lmst} \phi_{Nlmst} + V_{sh} \phi_{Nsh} \quad (2.2)$$

$$\Delta t = \phi \Delta t_{f1} + V_{sst} \Delta t_{sst} + V_{lmst} \Delta t_{lmst} + V_{sh} \Delta t_{sh} \quad (2.3)$$

$$1 = \phi + V_{sst} + V_{lmst} + V_{sh} \quad (2.4)$$

where: ϕ = effective porosity

$\rho_b, \phi_N, \Delta t$ = log readings of density, neutron and sonic log

$\rho_{f1}, \phi_{Nf1}, \Delta t_{f1}$ = log reading of 100 % pore fluid

$V_{sst}, V_{lmst}, V_{sh}$ = volume fractions of sandstone, limestone and shale

Due to the unknown shale point this set of four non-linear equations contains 7 unknowns: $\phi, V_{sst}, V_{lmst}, V_{sh}, \rho_{sh}, \phi_{Nsh}$ and Δt_{sh} .

To be able to solve these equations a relation has to be found between the 100 % shale responses of the three logs. As already shown in fig 2.3, the log responses vary widely opposite the overlying shale layers. If we now assume that any shale fraction within the formation itself is characterized by a mixture of the shales above the reservoir,

all possible shale points are represented by a straight line connecting the extreme log values in the caprock. The line is drawn in fig 2.3 and can be expressed as:

$$\rho_{\text{bsh}} = 2.51 - (\phi_{\text{Nsh}} - 20) * .0051 \quad (2.5)$$

with ρ_{bsh} = density log response to shale (g/cc)
 ϕ_{Nsh} = neutron log response to shale (p.u.)

A similar expression is found from the logs for the relation between the shale response of the neutron and sonic logs in this particular well.

The number of unknowns in equations 2.1 - 2.4 now is reduced to five and one more independent relation is required to solve the set. This extra equation is provided either by the porosity measurements on the cores, or by an independent shaliness indicator such as the Gamma Ray log. The Gamma Ray was used to provide the extra relation. It gives an estimate of the prevailing shaliness according to:

$$V_{\text{sh}} = (GR - GR_{\text{cl}}) / (GR_{\text{sh}} - GR_{\text{cl}}) \quad (2.6)$$

with: V_{sh} = volume percentage of shale present in the layer
 GR = response of Gamma Ray log ($^{\circ}$ API units)
 GR_{cl} = response of GR opposite the clean formation
 GR_{sh} = response of GR opposite 100 % shale (in this case also subjected to the variation opposite the shale layers)

Now the set of equations is completely determined.

An extra complication in this well is the presence of gas in the pores. The gas influences the log readings, so the log readings have to be corrected for gas-effect as well as for shale. Therefore the above equations had to be solved in an iterative way. In each step of the iteration the porosity was calculated from eqs. 2.1 - 2.4. The porosity in its turn determines the amount of gas correction needed for the well logs, using a watersaturation of the invaded zone of 70 % . After that, eqs 2.1 - 2.4 provide a new estimate of the porosity. The iteration was stopped when the porosities computed in two successive steps, did not differ more than .5 porosity per cent.

Results of the evaluation procedure

Applying the evaluation method to the reservoir interval of interest provided the porosity, lithology, shaliness and the corresponding location of the 100 % wet shale point for each layer. The range in different shale points thus established can be grouped into five specific values (table 2.1). The use of one of these five 100 % wet shale points to determine the formation properties in a particular layer gives sufficiently precise results.

Table 2.1 Range in 100 % wet shale log responses as determined by the evaluation procedure for the neutron, density and sonic logs (compressional wave).

ϕ_{Nsh} (lmst p.u.)	ρ_{bsh} (g/cc)	Δt_{sh} (μ s/ft)
20	2.51	95
25	2.48	100
30	2.46	105
35	2.43	110
41.5	2.40	115

The new method of determining the shale properties within the reservoir itself, instead of following the standard procedure of reading the values from the logs in a nearby thick shale layer, results in a much better correlation between the log-derived parameters. Fig 2.5 shows the volume percentage sandstone derived from a combination of FDC and CNL versus the amount of sandstone derived from a combination of CNL and Sonic logs. In this plot the logs were corrected using the appropriate shale points as determined by the special evaluation method. Compared with fig 2.4 (where the logs were corrected using the standard one shale point), the improvement is evident. Using the new method, not only the correlation between the logs is much better, but the log-derived lithology correlates well with the lithology observed in thin sections made from the cores (Visser and van Baaren, 1985).

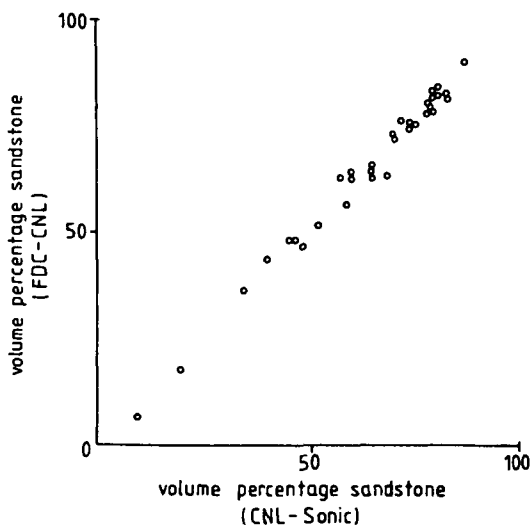


Fig 2.5
 Vol. percentage sandstone derived from the combined density and neutron logs versus vol. percentage sandstone derived from neutron and sonic logs. Logs were corrected for shale using the new evaluation procedure, (i.e. five shale points).

Apart from a better, more detailed lithology description, the method results in a more accurate estimate of the porosity (Visser and van Baaren, 1985). The calculated total porosity is now in very good agreement with the independently measured core porosities. As a consequence, the method also affects the calculated quantity of gas in place. The hydrocarbon saturation calculated with the Waxman-Smiths equation is, using the conventional and the proposed shale correction method, respectively:

$$1 \text{ shale point} : \sum S_h^* \phi = 3.80$$

$$5 \text{ shale points} : \sum S_h^* \phi = 3.44$$

So, the amount of hydrocarbons calculated using the standard procedure is 10.5 percent too high.

Types of shale present in the reservoir

Having established the validity of different shale points for different parts of the reservoir, it is still necessary to explain why the properties of the shale fraction vary. To clarify the phenomenon, three possible causes have been investigated: shale distribution, silt-index and mineralogy of the clays, of which the last one is considered to be the most important.

- a) shale distribution

The distribution of the shale fraction has been calculated from an FDC-CNL crossplot (Poupon, Clavier et al. 1970) and is shown in fig 2.6.

The total volume percentage of shale present in the formation is subdivided into its dispersed, structural and laminar fractions.

Inspection of this plot shows that, roughly speaking, half of the total shale volume is dispersed shale, one-third is structural and one-sixth is laminar shale. Although the total shale content changes with depth, the relative quantities of the three types of distribution remain more or less the same (except for those areas where the core description indicates heavy bioturbation; here the quantity of laminar shale almost reduces to zero). And as the dispersed, structural and laminar fractions remain present in the same relative amounts, the log properties of the total shale fraction should not vary significantly. So it may reasonably be assumed that the differences in shale properties can not be explained by shale distribution effects.

- b) Silt index

Although in general the shale properties vary with changing silt content, silt is probably not responsible for the different shale points in this well. Dispersed shale does not contain silt. So any silt

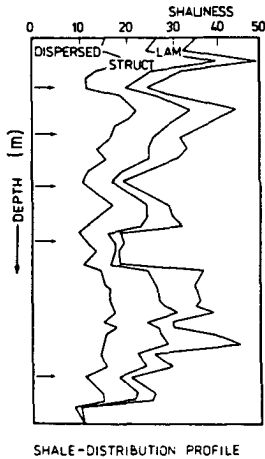


Fig 2.6
Volume percentage shale in the reservoir versus depth. The total volume of shale is subdivided into its dispersed, structural and laminar part. The arrows indicate areas of extensive bioturbation observed on the cores. Depth interval = 21 m.

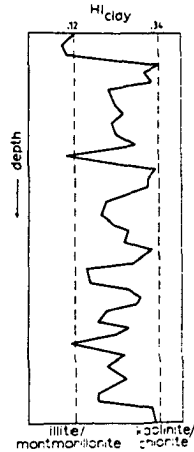


Fig 2.7
Hydrogen Index of the dry shale fraction versus depth. The hydrogen index has been calculated according to eq. 2.7. Depth interval = 21 m.

present has to be contained in the structural and laminar shale fractions. To explain the range in shale properties observed in the well, silt would have to be abundantly present. Even to such an extent that all the structural and laminar shale fractions would have to exist exclusively of silt. This is very unlikely; the more so as hardly any silt is evident in the thin sections made from the cores.

- c) Clay mineralogy

The third possible cause for the varying shale properties that was investigated, is the mineralogy of the shales. The mineralogy can be characterized by its hydrogen index, which may be expressed as follows (Juhasz, 1979):

$$HI_{cl\ dry} = \frac{\phi_N - \phi_t}{V_{sh} * (1 - \phi_{tsh})} \quad (2.7)$$

where

- HI_{cl dry} = hydrogen index of the dry clay mineral mixture
- V_{sh} = shale content (fraction BV)
- φ_N = Neutron porosity, corrected for gas (not for shale!)
- φ_t = total porosity
- φ_{tsh} = total porosity of the wet shale fraction

The hydrogen index has been calculated for each layer of the reservoir using the total porosity of the appropriate shale points. This porosity has been computed from the density values of the shale points using a dry shale density of 2.65 gr/cc.

The resulting HI-profile is displayed in fig 2.7 . The hydrogen index of the shales in the formation ranges from 0.1 to 0.34. Thus the shales consist of various mixtures of clay minerals as illite/montmorillonite (HI = 0.12) and chlorite/kaolinite (HI = 0.32).

Cation exchange capacity values measured on the cores correlate well with the implied clay mineralogy suggested by the HI-profile, confirming the varying clay mineralogy, which therefore appears to explain the varying shale properties over the reservoir interval.

II.3.2 Wavetrain interpretation

In the following section the wavetrain data recorded in the sandstone formation are correlated with the results from the petrophysical evaluation in the previous paragraphs. Indications from the wavetrains that point towards the presence of varying shale properties, are discussed. The influence of shale upon the interpretation of the wavetrains is treated in detail and attention is given to the required corrections to the data. The wavetrains are interpreted in terms of lithology and porosity. At the end of this chapter, a combined lithology/porosity crossplot is presented that provides accurate estimates of the formation parameters.

Indications for a varying shale point from the wavetrain

The shear (Δt_s) to compressional (Δt_c) transit time ratio is essentially a constant for a given lithology (Pickett 1963, Nations 1974). Experimental values range from 1.6 for sandstones to 1.9 for limestones.

In fig 2.8 the Δt -ratio determined in this well is plotted alongside the grain densities measured on the cores. The Δt -values were handpicked from the wavetrain log and they were borehole compensated as described in section II.2.

The ratio curve not corrected for shale agrees well with the lithology suggested by the measured densities. The curve which results from applying a shale correction to the

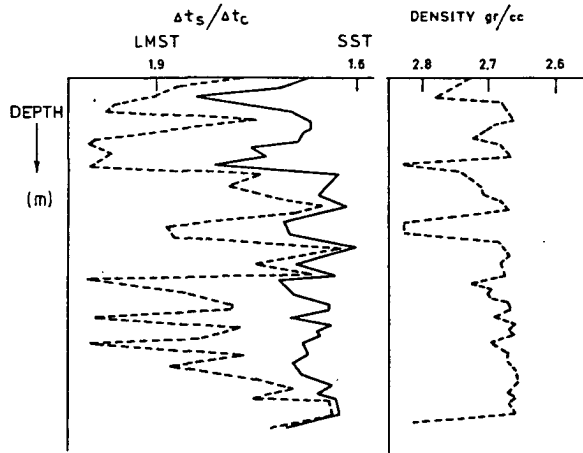


Fig 2.8
 $\Delta t_s / \Delta t_c$ versus grain density measured on cores
 ----- corrected for shale
 (one 100% wet shale point)
 _____ not corrected
 Depth interval = 21 m.

log data using one shale point, shows a much worse correlation. (The applied volumetric shale correction is discussed in the next section). The $\Delta t_s/\Delta t_c$ ratio reaches unrealistic values up to 2.0 in some parts of the reservoir, while in others the correlation remains good. Considering another shale point from the range observed opposite the shale layers does not improve the correlation; the same inconsistency remains, but other parts of the reservoir now correlate well with the density measurements. This same phenomenon was noticed with the petrophysical evaluation discussed in the previous chapter; a shale correction using one shale point makes the correlation between the parameters worse. If the results of the petrophysical evaluation are applied and a range of shale points is used to correct the acoustic logs for shaliness, where each reservoir interval is characterized by its own specific shale properties, the correlation between the transit times and the grain densities improves considerably (fig 2.9).

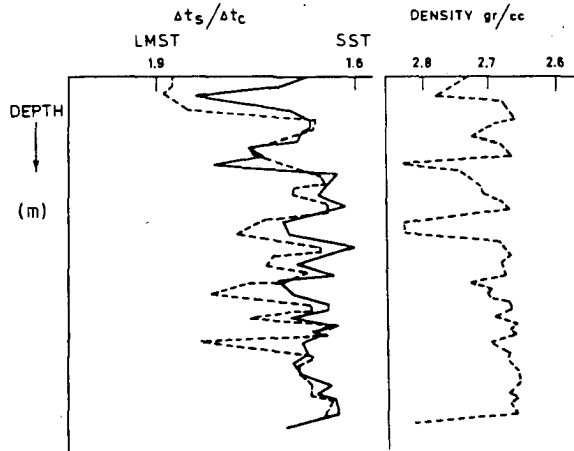


Fig 2.9
 $\Delta t_s/\Delta t_c$ versus grain density measured on cores
 ----- corrected for shale (five 100% wet shale points)
 _____ not corrected
 Depth interval = 21 m.

Figures 2.8 and 2.9 show clearly that the $\Delta t_s/\Delta t_c$ ratio gives a qualitative indication of the validity of the shale correction. The traditional correction results in an unrealistic transit time ratio (fig 2.8), while the improved correction (fig 2.9) shows a much better

correlation with the measured core densities. The $\Delta t_s/\Delta t_c$ ratio arrived at without any correction, also yields a good correlation. Which of the two $\Delta t_s/\Delta t_c$ -profiles shown in fig 2.9 is the most representative, cannot really be demonstrated by the comparison to grain densities.

Corrections applied to the acoustic data

As was shown in the previous section, the shale correction is critical to interpret the acoustic data correctly. The results of this acoustic field study strongly depend upon the type of shale correction used. It is thus important to describe the followed procedure in detail, so an extensive coverage is given here of the applied correction.

A second factor which influences the acoustic wavetrains, is the presence of gas in the formation. Although this influence is in this case of minor importance in comparison with the shale correction, it should be accounted for, too.

- Gas effect

Compressional wave velocity is sensitive to the compressibility of the fluid that saturates the pores. As the compressibility of this fluid increases, as it will with the addition of gas, the compressional wave velocity decreases. Shear wave velocity is not sensitive to the saturating fluid. So, before interpreting the wavetrain data, the gas effect upon the compressional wave has to be accounted for.

Raymer, Hunt and Gardner (1980) propose a decrease of 4 $\mu\text{s}/\text{ft}$ to correct the transit time for gas in a fully gas saturated reservoir. However, since the depth of investigation of the sonic log is very shallow, the investigated part of the formation will normally not be saturated with gas due to the invasion of mud filtrate. In the field example considered here, the flushed zone gas saturation varies between 0 and 50 percent of the pore volume. Accordingly, a gas correction was applied which varies with the gas saturation of the flushed zone. The compressional transit times were corrected by -3 $\mu\text{s}/\text{ft}$ for a 50 % gas saturation, the correction diminishing with decreasing gas saturation. In general, the correction amounts to approximately -2 $\mu\text{s}/\text{ft}$ over the interval of interest.

The exact magnitude of the applied correction is debatable, but the correction is relatively small and will affect the calculated transit time ratio only to a limited degree. A change in Δt_c of $-2 \mu\text{s}/\text{ft}$ results in a shift of approximately 2.5 % in the calculated ratio ($\Delta t_c = 85 \mu\text{sec}/\text{ft}$, $\Delta t_s = 143 \mu\text{sec}/\text{ft}$). The inaccuracy of the recorded transit times is about $1 \mu\text{sec}/\text{ft}$, so inaccuracies introduced by the gas correction lie in the same order of magnitude as the natural scatter of the acoustic data.

- Shale correction

The shale correction of the data is much more important. The presence of shale influences both compressional and shear waves. And even though only small amounts of shale are usually present, the reduction in velocity associated with it is large; the shale content is second in importance only to porosity in reducing wave speeds. Both the type of distribution and the mineralogy of the shale affect the acoustic properties of the shale fraction. In our field example both effects play a role in the shale correction.

Very little has been published about the way the shale distribution affects the recorded wavetrain. It is clear though, that the wavetrain is affected differently by laminar and structural shale on the one hand, and dispersed shale on the other. Laminated and structural shales are subjected to the overburden pressure. During burial most of the water contained in the shales is driven out in successive stages of compaction until a hard shale streak remains. Dispersed clay on the other hand, is formed by precipitation of ions from the formation fluid in the pore space. No pressure differential is exerted on them and they can grow freely in the pores, frequently forming the well-known blooming structures. The completely different geometry of the shales distributed in the three different ways, results in unequal acoustic characteristics.

It is however very difficult to determine these characteristics for each type of distribution separately. The petrophysical evaluation in our examples shows that the shale fraction is always a mixture of the three types of distribution (fig 2.6). Consequently, a log reading cannot be obtained for each distribution separately. The acoustic log readings, therefore, were corrected for the shale effect using the following general volumetric correction regardless of the distribution:

$$\Delta t = (\Delta t_{\log} - V_{sh} * \Delta t_{shale}) / (1 - V_{sh}) \quad (2.8)$$

where

Δt = interval transit time of the formation as if no shale were present, ($\mu\text{s}/\text{ft}$).

Δt_{\log} = borehole compensated transit time as read from the log

Δt_{shale} = transit time of 100 % shale

V_{sh} = amount of shale present (fraction bulk volume)

The equation was used for compressional as well as shear waves. When correcting the shear wave for shale, all Δt -values in eq. 2.8 refer to shear waves. When correcting the compressional wave, all Δt -values are compressional. The quantity of shale to be used in the equation, is taken from the results of the evaluation procedure described in section II.3.1, equations 2.1 - 2.4.

The equation assumes that the shale fraction is present in horizontal streaks perpendicular to the direction of propagation of the acoustic waves. This assumption is valid for laminar shale and, to a somewhat lesser degree, for structural shale. It is questionable whether it also describes the effect of dispersed shale adequately. Mineralogical effects are accounted for in equation 2.8 by way of the Δt_{shale} -values, the shear and compressional wave transit times in 100 % shale. The improved evaluation method postulates the presence of five shale mineral mixtures in the well, each one possessing its own shale point. Determining the shale points automatically results in a compressional Δt_{shale} -value for each shale mineral mixture. The method does not provide these values for the shear wave, but they can easily be correlated. The signature of the shear wave on the VDL-logs is rather blurred in the overlying shale layers, but the shear transit times in the shales lie approximately between 165 and 185 $\mu\text{s}/\text{ft}$. Knowing that five shale points are present and correlating with some layers of which the lithology is exactly known, the five different shear transit times could be determined. The respective Δt_{shale} -values for the shear and compressional waves are given in table 2.2. The table also lists the shear to compressional transit time ratio belonging to each shale mineral mixture together with their hydrogen index. The transit time ratio appears to vary with the mineralogical composition of the shale. The shales with a low hydrogen index (illite/ montmorillonite) exhibit a high transit time ratio and a low ratio is found for shales with a

high hydrogen index (chlorite/kaolinite). Mineral mixtures in-between show a transit time ratio proportional to the constituents.

Table 2.2 Shear and compressional transit times for the five shale mineral mixtures present in the reservoir.

	compr. Δt_{shale}	shear Δt_{shale}	Δt -ratio	Hydrogen Index
1	95 $\mu\text{s}/\text{ft}$	163 $\mu\text{s}/\text{ft}$	1.72	.12
2	100	168.5	1.69	.18
3	105	174	1.66	.23
4	110	179.5	1.63	.27
5	115	185	1.61	.33

Lithology determination from the wavetrains

The shear (Δt_s) to compressional (Δt_c) transit time ratio essentially is a constant for a given lithology. For the formations most commonly encountered in oil or gas exploration, the ratio has values of (Pickett 1963, Nations 1974):

sandstone	$\Delta t_s / \Delta t_c = 1.6$
dolomite	$= 1.8$
limestone	$= 1.9$

These constants are experimental values determined on reservoir rocks on a worldwide basis. They are valid for clean (no shale content), waterbearing formations.

The gas- and shale-corrected compressional and shear transit times of our field example are plotted in fig 2.10. The transit times were corrected for shale with equation 2.8, using the appropriate shale values of table 2.2, and the shaliness derived from the petrophysical evaluation. The constant lithology lines are drawn according to the experimental values of Nations (1974). The plot shows a sandstone reservoir containing on average some 25 % limestone. Some of the layers

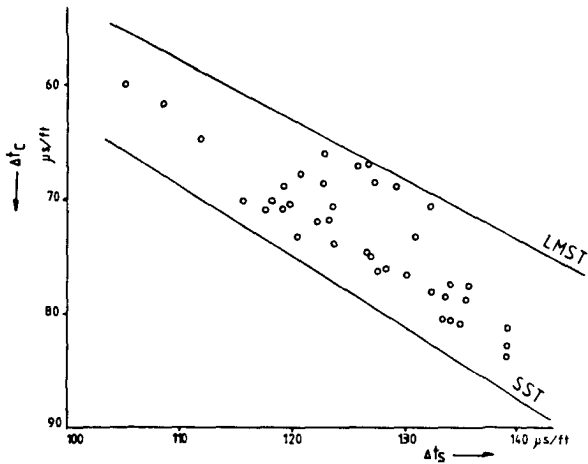


Fig 2.10
 Δt_s versus Δt_c .

Transit times have been corrected for shale.
 SST = sandstone
 LMST = limestone

plot close to the limestone line. They correspond to the conglomeratic influx of carbonates. By linear interpolation the composition of the matrix can be determined from the plot. The resulting percentage sandstone has been plotted versus the percentage sandstone determined from a Neutron-Density crossplot in fig 2.11. The agreement is good; all layers are grouped around the 45° line. This good agreement is remarkable considering that the established lithology is very sensitive to the $\Delta t_s/\Delta t_c$ -ratio. The dashed lines in fig 2.11 correspond to the quantity of sandstone calculated with an error of 1 % in the transit time ratio. The accuracy in the transit time ratio as a result of reading the compressional and shear wave arrival times from the VDL-log, already amounts to 1.5 % . So none of the layers plotted in fig 2.11 exceeds the scatter in the

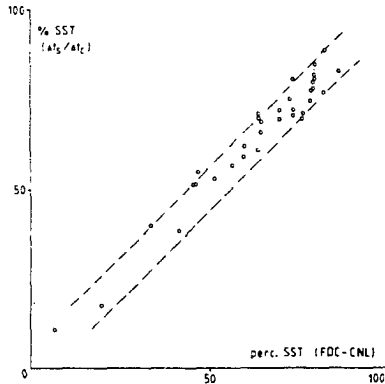


Fig 2.11
 Volume percentage sandstone derived from acoustic wave-trains vs. vol. perc. sst from lithology crossplots. Dashed lines refer to lithology calculated with an inaccuracy of 1 % in the transit time ratio.

log measurements. This result confirms the validity of the applied shale correction procedure. It also shows that a quantitative lithology analysis using the wavetrains alone, is as accurate as a combination of two other independent lithology indicators in this field example.

Lithology determination from the wavetrains without shale correction

The previous section showed that a good estimate of the lithology can be obtained from the wavetrains. However, a very elaborate shale correction was required to obtain the desired results. It is therefore interesting to investigate how the wavetrain behaves without any shale correction at all.

The shear-to-compressional-wave transit time ratio determined for the five shale mineral mixtures (ref. Table 2.2), does not differ largely from the ratio expected for a clean sandstone matrix ($\Delta t_s/\Delta t_c = 1.6$). Furthermore, the uncorrected wavetrain ratio correlates well with the core density measurements as described at the beginning of this chapter (ref. fig 2.8). These two facts indicate that it should be possible to make a reasonable estimate of the lithology from the wavetrains, even if they are not corrected for shale. This assumption is confirmed by fig 2.12, where the transit times not corrected for shale, have been crossplotted.

The plot shows a sandstone containing some limestone. It indicates a sandstone percentage which is only an average 10 volume percent too high in comparison with the shale corrected lithology plot (fig 2.10). So the quantitative lithology indication is good. The transit time ratio read straight from the VDL-log appears to give a good "quick look"-indication of the matrix lithology in this shaly sandstone example, without the (usually) elaborate shale correction.

The uncorrected log values plot closer together in fig 2.12 than the corrected ones in fig 2.10. This is caused by the type of porosity by which the plots are influenced. As is explained in the following sections, the plot corrected for shale indicates the effective porosity in the reservoir, whereas fig 2.12 relates to the total porosity.

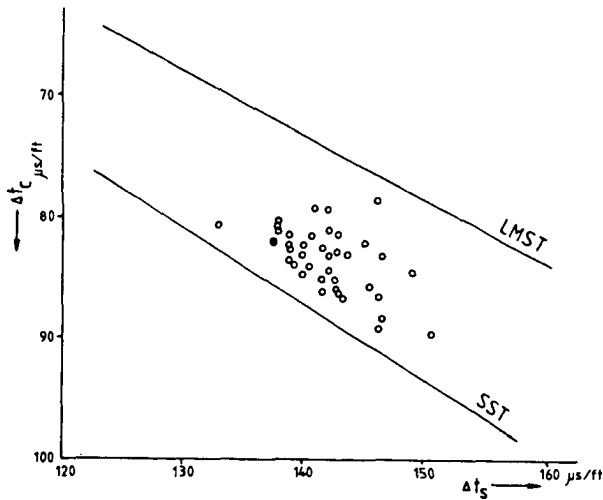


Fig 2.12 Δt_s versus Δt_c .

Transit times not corrected for shale.

Porosity determination from the wavetrains

The transit times of the compressional and shear waves in a formation are determined by the lithology as well as by the porosity of that formation. In order to make a correct prediction of the porosity from the wavetrains, this lithology dependence has to be eliminated first. For this purpose the "Wyllie time-average equation" (Wyllie et al, 1956) was used. It is the equation most commonly used in the oil industry to relate the Δt -compressional to porosity:

$$\Delta t_c = \phi \Delta t_{fl} + (1 - \phi) \Delta t_{ma} \quad (2.9)$$

with Δt_c = compressional transit time, ($\mu\text{s}/\text{ft}$)
 Δt_{fl} = transit time pore fluid, (= 185 $\mu\text{s}/\text{ft}$)
 Δt_{ma} = transit time matrix, ($\mu\text{s}/\text{ft}$)
 ϕ = porosity, (fraction BV)

The equation relates the transit time of the compressional wave to the porosity while incorporating the lithology dependence of the acoustic data. It is valid for clean lithologies, not for shaly reservoirs. The porosity featuring in eq 2.9, corresponds to the interconnected porosity. A correction factor has to be included if any secondary non-interconnected pores are present.

The equation was established only for compressional waves. It cannot be used to derive the porosity from the shear wave. Liquids do not sustain shear waves, so a Δt_{f1} does not exist for shear waves.

The compressional and shear wave transit times recorded in our shaly sandstone formation are plotted versus the porosity in figs 2.13 and 2.14, respectively. The shale effect is eliminated from the plotted transit times as well as from the porosity.

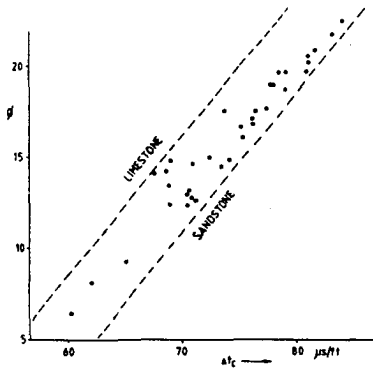


Fig 2.13
Compressional Δt versus porosity
Data are corrected for shale.

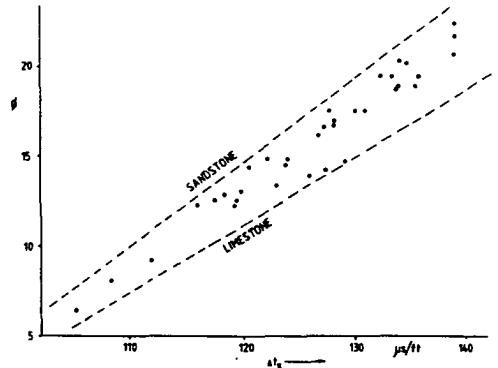


Fig 2.14
Shear Δt versus porosity.
Data are corrected for shale.

The lithology dependence of the acoustic waves is indicated in both plots by drawing the $\Delta t - \phi$ relationship for sandstone and limestone. The Wyllie equation was employed to construct this relationship for the compressional wave, using a matrix transit time of 55.5 $\mu\text{s}/\text{ft}$ for sandstone and of 47.5 $\mu\text{s}/\text{ft}$ for limestone. A relation similar to the Wyllie equation, which relates the shear Δt to porosity does not exist. The lithology lines drawn in fig 2.14 are derived from the compressional transit times, using a $\Delta t_s/\Delta t_c$ ratio of 1.6 for sandstone and 1.9 for limestone.

The transit times in both plots were corrected for shale using the volumetric shale correction given by eq 2.8. The plotted values represent the reservoir as if no shale were present.

The porosity (ϕ) was corrected for shale effects, too. The plotted values represent the porosity calculated as if no shale were present. They were calculated from the effective porosity determined with the petrophysical evaluation procedure (eqs. 2.1 - 2.4), according to:

$$\phi_{\text{eff}} = \phi * (1 - V_{\text{sh}}) \quad (2.10)$$

where

ϕ_{eff} = actual effective porosity given by eqs 2.1 - 2.4, (vol. %)

V_{sh} = shaliness given by eqs 2.1 - 2.4, (fr. BV)

ϕ = porosity as if no shale were present, (vol. %)

Figures 2.13 and 2.14 show a well-defined trend of the compressional and shear wave transit times with porosity. The variation with lithology, however, is large in both plots. In order to make an accurate porosity estimation from the transit times, the lithology of the formation has to be known fairly accurately.

The relation between transit time and porosity is steeper for the compressional than for the shear wave. This is in agreement with the observations made by Pickett (1963) and Nations (1974). A small inaccuracy in transit time will affect the derived porosity less when using the shear wave than when using the compressional wave. On the other hand, the first arrival of the shear wave often is difficult to determine on the logs, which will result in a larger inaccuracy in the calculated transit time. Taken together, the two effects will probably cancel out and it does not offer any advantages to derive the porosity from the shear wave instead of from the compressional.

Combined porosity-lithology crossplot

In the previous section it was noted that the lithology of the formation has to be known to make an accurate porosity estimate from the wavetrains. The lithology itself can also be derived from the wavetrains, as shown earlier. So the obvious solution is to combine the porosity and lithology determination in one crossplot.

In fig 2.15 Δt_c has been plotted versus Δt_s . The Δt -values are corrected for shale. The lines denoting a constant lithology are graduated for porosity using the Wyllie time average equation. In doing so, it was assumed that the porosity is equally distributed among the two lithologies. The graph is valid for "clean" lithologies, containing no shale.

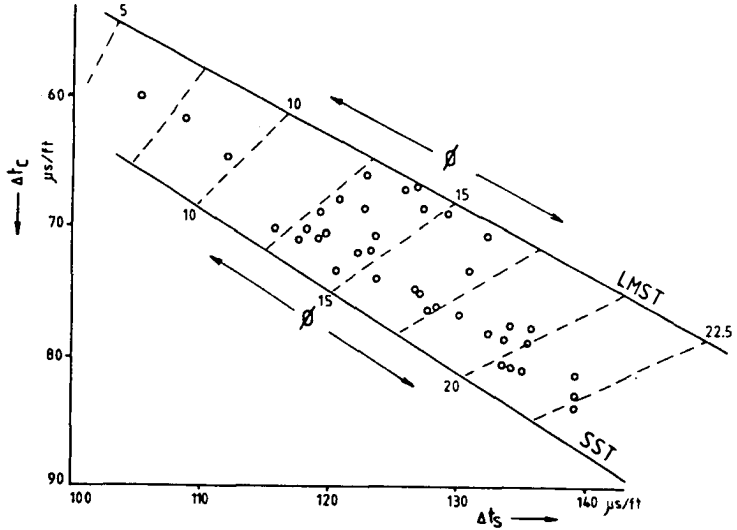


Fig 2.15
 $\Delta t_s / \Delta t_c$ -ratio to lithology transform graduated for porosity.

The lithology indicated by the plotted layers has already been discussed in the previous paragraph.

The porosity values following from the porosity graduation were converted to total porosity and compared with the core porosities in fig 2.16. The conversion was carried out according to:

$$\phi_t = \phi * (1 - V_{sh}) + V_{sh} * \phi_{tshale} \quad (2.11)$$

with ϕ_t = total porosity

ϕ = porosity derived from fig 2.15

V_{sh} = shale fraction present

ϕ_{tshale} = amount of water contained in the shales

The V_{sh} and ϕ_{tshale} values used in the equation, were derived from the petrophysical evaluation (eqs 2.1 - 2.4). The ϕ_{tshale} was calculated from the appropriate wet shale point as determined by the improved evaluation procedure, using a dry shale density of 2.65 gr/cc for each shale type. The conversion is necessary because fig 2.15 is valid for shale-free formations only. It yields porosity values for the shale-free portion of the formation. The porosity values measured on the cores, on the other hand, correspond to the total porosity of the formation; i.e. they include the effective porosity of the formation as well as the porosity associated with the shale fraction.

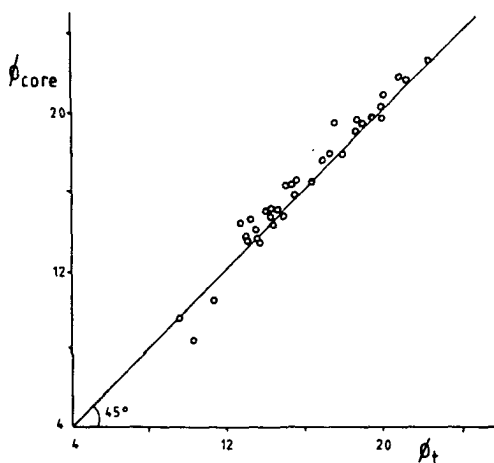


Fig 2.16
Total porosity derived
from wavetrains versus
core porosity.

Fig 2.16 shows that the acoustically derived total porosity values compare very well with the porosity derived from the cores, especially if one takes into account that the core porosities have been measured on small plugs (1 inch diam.), whereas the transit times are average values over a two-foot formation interval.

The general trend in the graph indicates the core porosities to be slightly higher, which is probably due to pressure relaxation of the core material. The core measurements are carried out under atmospheric circumstances, whereas the reservoir itself is subjected to the overburden pressure. The atmospherically measured porosities can be some 0.5 to 1 porosity percent higher than the in-situ porosities, which are derived from the acoustic transit times.

II.4 Dolomite formation

The second field example is a very homogeneous gas-bearing dolomite reservoir, part of the Zechstein-2 carbonates. The formation consists exclusively of dolomite. No contaminations of any kind are present.

The interpretation of the wavetrain logs recorded in this well is hampered by the presence of non-interconnected porosity and by the presence of many fractures in the formation. Furthermore, the porosity encountered in the reservoir is very low. These effects added together, make it impossible to draw any definite conclusions from this field study.

The discussion of this formation proceeds in the same manner as in the previous field example. The petrophysical evaluation of the reservoir is given first, followed by the wavetrain interpretation.

II.4.1 Petrophysical evaluation

Description of the reservoir

The reservoir is characterised by a pure dolomite lithology. The cap- and baserock both consist of thick anhydrite layers. The dolomite is separated from the anhydrite caprock by a shale streak with a thickness of approximately 1 metre.

The reservoir formation is very tight; the porosity ranges from 1 - 3 % BV, and permeabilities measured on the cores are around 1 mDarcy. Due to dolomitisation some secondary porosity is present.

The well was completely cored with a recovery of 100 percent. A full logging suite was run in the well. Core measurements are also available.

The formation is heavily fractured. Some 70 fractures can be recognized on the cores as well as on a Fracture Identification Log. This explains the relatively high gas production-rate obtained during a production test.

The reservoir characteristics are:

net reservoir thickness	:	42.7 m.
average porosity ($\Sigma\phi^*h/\Sigma h$)	:	1.8 % BV
average watersaturation	:	50 %
porosity column ($\Sigma\phi^*h$)	:	.8 m.
S_h column ($\Sigma\phi^*h*S_h/\Sigma\phi^*h$)	:	.4 m.

Due to the very low porosity values the accuracy of these numbers is poor. The error in the porosity estimates is at least ± 0.5 % BV, so the values only give a qualitative indication of the reservoir.

The well has been drilled deviated; the maximum deviation encountered is 15.3 degrees. The formation of interest was intersected at an angle of approximately 2 degrees, so no deviation correction is necessary for the reservoir section.

Types of porosity encountered in the formation

The range in porosity values encountered in this homogeneous formation is very small, i.e. 0.5 - 3 % BV. As a consequence, the matrix density is high, which results in a relatively high degree of scatter in the various porosity logs.

A comparison of the log-derived porosities with the core measurements shows that the core porosities are significantly lower. The log derived porosities range from 0.5 to 3 % BV, while the core porosities range from 0.2 to 1.1 % BV. This discrepancy was found to be caused by poorly connected porosity in the reservoir.

On the cores the porosity was measured by the wet-and-dry-weight method, where the submerged weight of a saturated core sample is compared to the dry weight in order to calculate the grain volume. If some of the pores are connected by very narrow pore throats, the saturation may not be complete, resulting in too large grain volumes and hence too low porosity values. The Density and Neutron logs however, indicate the total porosity, regardless of the pores being interconnected or not.

The presence of poorly connected pores has been checked by porosity measurements using the Boyle meter on core plugs. The Boyle meter uses gas pressure to determine the porosity and is not influenced by very

narrow pore throats. This method gave a porosity of 2.5 % BV, whereas the wet-and-dry-weight method measured only 0.5 % BV on the same plug. The Boyle meter thus confirms that some of the porosity is poorly interconnected. The amount of poorly connected porosity is small but it is relatively high compared to the primary porosity in this tight formation.

As the porosity values derived from the Neutron log agree well with those measured by the Boyle meter, the Neutron log is assumed to give the correct porosity and the Neutron porosity is used in the following.

II.4.3 Wavetrain interpretation

Lithology determination

The transit times of the shear and compressional waves are crossplotted in fig 2.17. The pure lithology lines in this plot have been drawn in accordance with the experimental values of Nations (1974); i.e. $\Delta t_s/\Delta t_c$ is equal to 1.8 for dolomite and 1.9 for limestone.

The transit times recorded in this dolomite reservoir do not indicate the lithology as accurately as they did in the previous sandstone field example. The plot clearly shows a carbonate reservoir, but indicates a large limestone content, whereas the formation consists almost exclusively of dolomite.

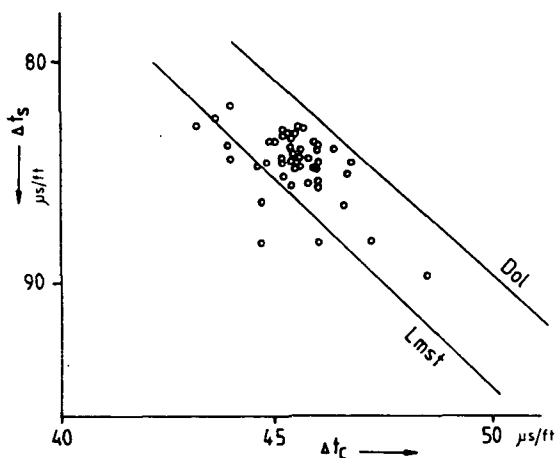


Fig 2.17 Shear Δt versus compressional Δt in the dolomite formation.

X-ray diffraction and röntgen fluorescence analysis confirmed that the reservoir consists almost exclusively of dolomite with very small fractions of limestone and traces of quartz. The latter mineral probably filled some of the fractures in the formation.

The pure dolomite lithology is not reflected in the $\Delta t_s/\Delta t_c$ -ratio. At most, the transit time ratio only gives a qualitative indication of the lithology in this well.

Porosity determination

The transit times of the compressional and shear waves are plotted versus the porosity in figs 2.18 and 2.19 respectively. The plotted porosities are taken from the Neutron log and include primary as well as poorly interconnected porosity. The "Wyllie time-average equation" (eq. 2.9) is drawn for the compressional wave, using a matrix transit time of 43.5 $\mu\text{s}/\text{ft}$. Although the Wyllie-equation is not valid for shear waves, a similar expression can be obtained for the transit time of the shear wave by calibrating Δt_s from Δt_c using a constant ratio of 1.8. This line is drawn in fig 2.19.

Fig 2.18 shows that using the Wyllie equation to obtain the porosity from the compressional wave will result in values that are slightly too low. This is probably caused by the non-connected pores to which the compressional wave does not respond. The Wyllie equation indicates porosities between 0 and 2.5 percent BV, which is slightly higher than the

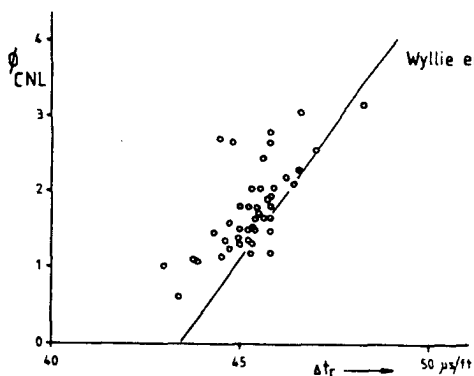


Fig 2.18
Compressional Δt versus porosity

core porosities but lower than the porosities given by the Neutron log. Application of the calibrated "Wyllie equation" to the shear wave would yield too high porosity estimates in comparison with the Neutron log (fig 2.19). The many fractures in the reservoir section may have increased the calculated shear transit time.

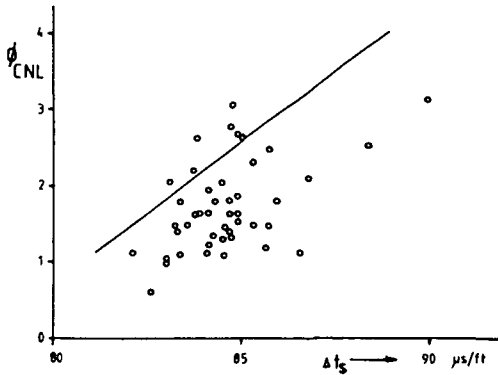


Fig 2.19
Shear Δt versus porosity
Line is calculated from
Wyllie equation in com-
bination with a $\Delta t_s/\Delta t_c$
ratio of 1.8.

Both porosity plots show quite a bit of scattering due to poorly inter-connected porosity and the presence of many fractures. The effect of these factors upon the wavetrains is only qualitatively known, thus making a quantitative interpretation of the acoustic waves impossible in this well. And in any case, the formation is too homogeneous and therefore the range in encountered porosities too small, to be able to observe any well defined trend.

II.5 Discussion of results

The two field studies clearly indicate the limitations of using natural reservoir formations for acoustic research. But they also show some of the potential applications of the sonic wavetrain in formation evaluation. In the shaly sandstone formation the shale and hydrocarbon corrected shear-to-compressional transit time ratio gave accurate estimates of the porosity and lithology. The wavetrains also indicate that the properties of the shale fraction are not constant in the formation; it may offer additional information for evaluating complex shaly reservoirs. In the dolomite formation the Δt_c appears to give an indication of the connected porosity.

The trends however, only became visible after extensive reworking of the recorded data. The shaly sandstone example required an extensive shale correction to the data set in order to determine the matrix properties. In this particular field example the corrections could be worked out and the same approach may be applicable to other wells in

the same field. But it will be very difficult to compare the results with other fields which may require a completely different shale correction. The same goes for the results from the dolomite reservoir, where the exact influence on the wavetrain of the poorly connected porosity and the fractures can only be guessed at.

Due to these circumstances it would be premature to base any definite conclusions on the interpretation of only these two field examples. Further field studies of shaly reservoirs should be performed to check the conclusions reached here and to explore the possible applications of the wavetrains in shaly formations any further. On the same grounds it is important to investigate some more carbonate formations. Preferably, these formations should have a wide porosity range to overcome the limitations of the dolomite example.

Field studies are not able to reveal the precise correlation between a specific rock parameter and the recorded wavetrain, because too many unknowns are present. Geometrical effects of the borehole left aside, no two formations are alike. An empirical approach to investigate acoustic behaviour by comparing field data, always encounters great difficulties in ascribing certain characteristics of the wavetrain to a particular reservoir property. The correlations are always obscured by the many factors that influence the wavetrains in an unknown manner, viz.:

- 1) In general the rock is not homogeneous over a length of 2 feet, being the vertical resolution of the acoustic recording. The acoustic data are average readings and are hard to compare with core data, which are measured on small plugs (1 inch diam.).
- 2) Local effects upon the wavetrain have to be taken into account, such as wash-outs, borehole size, borehole rugosity, mud, mudcake, fluid content of the formation (gas), stress effects.
- 3) In general it is not possible to find two rock samples differing only in one specific property. The bulk rock parameters constitute a combination of several smaller effects.

From field data, at best a broad, general correlation can be found between the recorded acoustic data and the petrophysical parameters of the formation. To study the acoustic behaviour of rocks in detail, it was therefore decided to go back to the laboratory. By performing experiments on artificially made rocks most, of the above mentioned effects can be isolated. Environmental effects are eliminated and, if made properly, the artificial rock samples are homogeneous and the properties of the samples are under control. Having established correlations between the acoustic measurements and the sample parameters, the obtained relations can then be applied to well-data to improve the wavetrain interpretation in the field.

III. ARTIFICIAL SANDSTONES

III.1 Introduction

The field examples of the previous chapter showed that at best a very general correlation between acoustic parameters and formation characteristics may be derived in an experimental approach using natural cores. Too many rock properties vary between specimen to be able to obtain specific results. The use of artificial rock samples was therefore indicated. When a proper consolidation technique is employed, homogeneous samples with known properties can be prepared. Also, by varying the base materials of the samples, it is possible to vary the formation characteristics of interest. This provides the opportunity to construct a range of rock specimen varying in one aspect only; that aspect can then be linked to the acoustic response of the rock samples. In order to subsequently extrapolate any correlations between acoustic and synthetic rock parameters to natural reservoir formations, it is essential for the samples to resemble natural rocks. The samples should exhibit all the intrinsic characteristics of a natural reservoir rock. A laboratory procedure was developed for the construction of artificial rock samples that fulfill this requirement. A consolidation technique is used, which resembles the natural process of cementation of reservoir formations. First a dense packing of loose sand grains is prepared and then the grains are cemented at the grain contacts to form a porous rock.

Three types of cementing material have been tested, viz.:

- silica produced from silicontetrachloride, so-called silica-lock,
- silica produced from methylsilicate, and
- araldite.

The araldite cement proved to be the most appropriate one. Despite considerable efforts, reproducible, completely homogeneous rock samples could not be obtained using the silica-lock method, although the existing inhomogeneities did not appear to influence the acoustic response of the samples significantly.

In this chapter first a review is given of the various published methods used to produce synthetic cores. Then the requirements that the

samples have to fulfill to be suitable for our acoustic experiments, are listed. The chemical aspects of the consolidation process and the consolidation procedures themselves, are treated. Extensive coverage is given to the inhomogeneities generated in the samples using the silica-lock method and to the various experiments performed in order to eliminate the irregularities. The chapter ends with a general description of the sample properties and a comparison with natural rock.

III.2 Review of synthetic cores

Artificially made porous media have been used by several investigators for acoustic or resistivity measurements. The porous media reported in this context range from commercially available metalliferous materials to laboratory-made sandstones consisting of loose grains cemented together. In the following a succinct review of the synthetic cores reported in the literature will be given to see which cores will suit our needs best. Since we in our project are interested in materials resembling natural reservoir rocks as closely as possible, the review will be limited to quartz grains glued together somehow.

Grains mixed with cement

Synthetic rock samples consisting of quartz sand grains mixed with commercially available cement, have been used for acoustic and resistivity measurements by Viksne et al (1961) and Mandel et al (1957).

The dry sand-cement mixture is stirred until homogeneous. After addition of water the wet mixture is subjected to pressure for 5 minutes after which the cement is allowed to set. The advantage of this method is that the amount of cement can be varied. By regulating the quantity of cement, porosities between 2.1 and 30.4 % were obtained.

A disadvantage of the method is the uncontrollable location of the cement within the sample. It seems unlikely that the method will result in samples with a homogeneous porosity distribution. A second serious shortcoming of this method is the resulting coating of the quartz grains by a thin film of cement. No grain-to-grain contacts are present in the produced samples and above a cement content of 17.5 % the grains

even started to float in a cement matrix. This results in a compressional velocity of the samples which strongly depends upon the manufacturing pressure of the cores. Another drawback of the method is that it is only applicable for small sized samples. The pressure required to compact the sand-cement mixture in practice sets a limit to the size of the samples that can be manufactured. For larger samples it would also be difficult to obtain a homogeneous sand-cement mixture and thus a homogeneous sandstone sample.

Glass beads

Plona (1980,1982) employed synthetic rocks made of glass beads (diam. 177-210 μm) sintered at the grain contacts by heating. The length of time in the oven determines the degree to which the porosity decreases from its initial value of 38 %, corresponding to a dense random packing of hard spheres.

As with the samples of Viksne et al, the porosity of the glass bead samples is variable. In contrast to the previous method, the grains are here cemented at the grain contacts and there is no cement filling up the pores. But again only relatively small core samples are possible and it is difficult to obtain homogeneous samples, especially larger ones. Furthermore, due to the perfect roundness of the glass beads, the packing characteristics differ from those of natural sandstones.

Mortar

Lebreton et al (1978) used large samples made of mortar for their acoustic measurements. Mortar (cement, sand, water, additive) was poured in a large pit with dimensions 5' x 5' x 40', and allowed to harden.

Very large samples can be manufactured with this method but it seems impossible to produce them homogeneously. The packing of the grains will be very bad and can not be controlled in any way. The permeability of the samples is mainly caused by fractures and the porosity is created by vugs and channels.

Silica-lock

In 1980, Davies and Meijs published the silica-lock method for consolidating sand grains. The method was developed to prevent sand production in unconsolidated gas wells. The silica-lock method consists of flowing vaporized silicon tetrachloride through a waterwet sandpack. At the grain contacts in the sand, water is held by capillary forces. The silicon tetrachloride reacts with this irreducible watersaturation to form amorphous silica, thus cementing the grains together.

The method is well suited for manufacturing artificial sandstone samples. It does not disturb the packing of the treated sand as only vapour is flowed through the sandpack. The dimensions of the sample are not limited to a certain size. Before treatment, the small amount of irreducible water in the sandpack is concentrated around the grain-to-grain contacts. So the amorphous silica formed during the process is only present in small quantities around the grain contacts. The grain-to-grain contacts themselves are not disturbed in any way. Since the quantities of silica formed during the process are small and this material is concentrated mainly at the grain contacts, the process results in a very small reduction in porosity and permeability.

A disadvantage of the process is the violent reaction of silicon tetrachloride with water. It requires stringent safety precautions in the laboratory.

Epoxy resin

Another process developed to overcome sand trouble in producing wells by consolidating loose sand uses an epoxy resin to "glue" the sand grains together (Havenaar and Meijs, 1963). As with the silica-lock method, the process leads to consolidated sands without significant reductions in permeability or porosity.

The resin is applied in the form of a solution to the dry sandpack. From the dilute solution a limited amount of resin is deposited predominantly around the grain contacts, thus glueing the grains together. A disadvantage of this procedure is that the resulting cement is not heat resistant.

The consolidation methods described above, all have their advantages and shortcomings. The consolidation processes developed to cure sand production (i.e. the last two) resemble natural sandstone rock best.

III.3 Sample requirements

The empirical approach of the project sets serious limitations to the artificial rock samples that can be used in our experiments. On the one hand it is required that one specific rock property can be singled out to be correlated with the variations in acoustic response, on the other hand the samples should resemble natural reservoir rock as closely as possible. The requirements to which the samples have to conform can be specified as follows:

- 1) The samples have to resemble actual reservoir material as closely as possible.
- 2) The consolidation process must be such that one property of the sample can be changed, keeping all other rock parameters more or less constant. For instance, it has to be possible to change the size of the grains making up the sample while all other parameters (such as porosity, roundness, sorting, cementation) remain the same.
- 3) The grains of the samples should be rock supporting, i.e. no thin film of cement should be present between the grain contacts..
- 4) The cementbond ideally should have the same acoustic characteristics as the grains (or at least the characteristics should be known exactly).
- 5) It has to be possible, within limits, to regulate the amount of cement.
- 6) The cement should be evenly distributed throughout the sample.
- 7) The rock properties of the samples must be known in detail.

- 8) The specimens have to be homogeneous in all directions (isotropic).
- 9) The samples have to be reproducible.
- 10) The dimensions of the manufactured samples have to be variable. Small samples need to be made for transmission measurements while the refraction measurements require large specimens (40×40×40 cm) to eliminate the disturbing influence of reflections from the sample edges.
- 11) The specimens should have enough strength to allow physical handling.
- 12) The samples should be water- and oil-resistant.
- 13) The samples should be sufficiently pressure- and heat-resistant to allow measurements under in-situ circumstances.

Comparing the above listed requirements with the consolidation methods reported in the literature, the Silica-lock method and the method using epoxy resin cement produce the best results. Provided the loose sand grains are properly packed prior to cementation, both methods produce artificial samples which closely resemble natural sandstone reservoir rock. The properties of the samples can be fully controlled and the dimensions of the samples are not limited in any way. These methods have therefore been selected for the acoustic research project.

III.4 Chemical aspects of the consolidation methods

Three alternative chemical processes were used to consolidate the loose sand. They are:

- 1) Reaction of vaporized silicontetrachloride with a connate water saturation in the sand to form amorphous silica at the grain contacts. (silica-lock process).
- 2) A process equal to silica-lock but using an organic silica compound as a reagent.

- 3) Imbibing the sandpack with a solution of araldite, an epoxy resin, and allowing the resin to harden at the grain contacts, thus forming a bond of high mechanical strength.

Of the three methods, both the silica-lock and the araldite method produce well-consolidated rock samples. The samples constructed by the silica-lock method however showed macroscopic fracture-like irregularities. Although acoustically the samples appear to behave homogeneously, the irregularities make them less reliable for fundamental research. To overcome the problems with the silica-lock method, an alternative silica compound was tested as a consolidating agent; methylsilicate. But this organic silica compound produced brittle samples which were too delicate for normal handling.

Silicontetrachloride

The silica-lock process is based upon the hydrolysis of silicontetrachloride:



The reaction is complete and progresses very fast and violently. During the reaction large amounts of gaseous hydrochloric acid are formed. The violent character of the reaction with water and the strong hydrochloric acid production require stringent safety precautions when handling silicontetrachloride.

The conversion of SiCl_4 into amorphous silica progresses along several intermediate stages. First the hydrolysis reaction of SiCl_4 takes place. The resulting silicic acids then polymerize into a gel in which water is trapped. Finally the gel is dehydrated and turned into a hard amorphous silica acting as a cement bond between the sand grains in the sample.

During hydrolysis of SiCl_4 a chlorine atom together with a hydrogen atom from the water split off as gaseous HCl . The open place in the SiCl_4 structure formerly occupied by the chlorine atom is taken by a hydroxyl group. This process is repeated until hydrolysis is complete. (Donker, 1986).

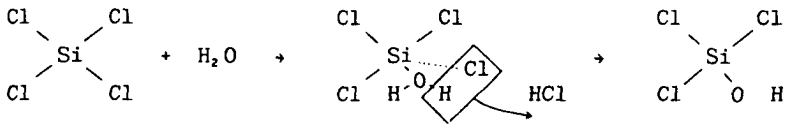


Fig 3.1 Hydrolysis of silicontetrachloride

The hydrolysis of silicontetrachloride is very fast and violent. The endproducts of the hydrolysis probably are $\text{Si}(\text{OH})_4$, (= orthosilicic acid H_2SiO_4 ,) and/or meta silicic acid H_2SiO_3 ,. Silicon does not form classical double bonds with oxygen. The silicic acids produced by the hydrolysis polymerize to form siloxane chains and networks.

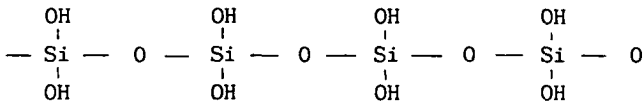
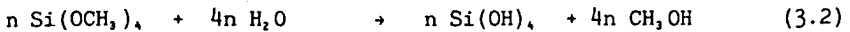


Fig 3.2 Polymerization of H_2SiO_3

Water is trapped inside the growing siloxane network and a gel is formed. The silicagel is a strong bonding agent that can bridge the distance between the particles of the sandstone sample. The initially jelly-like gel is dehydrated spontaneously (= syneresis) and by evaporation of water until a hard, dense cement remains. The dehydration is accompanied by shrinkage of the silica network.

Methylsilicate

The hydrolysis of methylsilicate is:



During the reaction the same silicic acids are formed as with the silica-lock process. The silica particles polymerize and form a gel binding the sand grains of the sample. Methanol however is produced instead of Hydrochloric acid. This alcohol has a lower surface tension than water and this could positively influence the shrinkage effects of the cement. The rate of hydrolysis of methylsilicate is very much slower than that of Silicon tetrachloride. The reaction can be

accelerated strongly by using an acid or a base as catalyst. As a result the rate of reaction can be controlled to a certain degree. A disadvantage of the use of methylsilicate as a bonding agent is that methylated silicon compounds are very toxic.

Araldite

A third consolidation method tested is the addition of an epoxy resin to the loose sandstone grains. A mixture of commercially available araldite AY103 and hardener HY956 is added to the sand grains as an adhesive. The mixture hardens and glues the grains together.

The hardening process of araldite commences as soon as it is mixed with the hardener. This seriously inhibits a homogeneous distribution of cement throughout the sample. To solve this problem the araldite was mixed with acetone. The solution has a low viscosity and it retards the hardening process strongly.

The consolidation of loose sand using araldite is a relatively simple method. No stringent safety precautions are required as the reaction is a slow hardening process and the araldite is not toxic. Using acetone as a solvent yields no undesired side-effects and results in a controllable process.

III.5 Sample construction

Artificial sandstone samples were constructed in different dimensions. Refraction measurements require large samples to prevent reflections from the sides of the sample interfering with the desired signals. For those measurements large cubic blocks were manufactured with ribs of 40×40×40 cm. Transmission measurements require only thin slices of core material. For these experiments it is sufficient to construct cylindrical samples with a diameter of 14 cm and a length of 15 cm.

Simply because of the dimensions, it is much easier to make the smaller cylindrical samples than the large blocks. Therefore only four large samples were manufactured up till now, each with a different grain size. All other sample construction experiments were carried out using the smaller cylindrical dimensions.

The construction process of the artificial rock samples proceeds in three separate stages. First the sand grains are compacted to obtain a homogeneous sample. Then the sandpack is saturated and drained to obtain a connate fluid saturation at the grain contacts. Finally the sand is consolidated by flowing silicontetrachloride through the sample or by evaporating the acetone from the araldite/acetone mixture.

III.5.1 Compaction of the grains

The packing of the sand grains is important to obtain a homogeneous and reproducible rock sample.

The vessel in which the cylindrical samples are consolidated is shown in fig 3.3. The container can be sealed with a lid to allow consolidation using silicontetrachloride in a later stage of the process. At the bottom of the vessel a 2 cm thick layer of very fine glass beads with a diameter of 35-70 μm is placed in order to drain the pack consisting of coarser sand grains. The main body of the container is filled with the sand grains that will form the rock sample. The sand grains are separated from the fine glass beads by a perforated plate to prevent the two grain sizes from mixing during the compaction process.

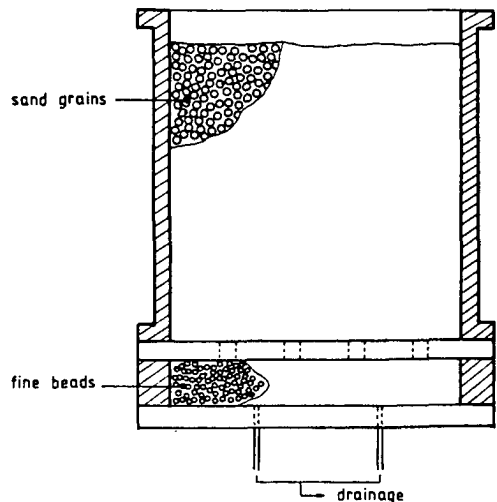


Fig 3.3
Consolidation vessel.

The loose sand grains in the vessel are compacted to the highest degree of compaction to get a good packing of the grains and to assure the reproducibility of the samples.

Three techniques were tested to compact the sand:

- vibration of the container.
- the 7-sieves technique.
- raining-in of the grains in the water-filled container.

The first and second techniques resulted in the lowest porosity of the sandpack and thus in the best compaction. The first technique is the simplest and consequently all cylindrical samples were compacted by vibrating the sample container on a vibration table, together with gentle hammering on the side of the container. During the process the degree of compaction is monitored by measuring the weight and volume of the sand in the container. In this manner a porosity of the unconsolidated sandpack of 38-39 % was reached for all samples.

The large cubic samples were compacted by a Stiletto vibrator table which vibrates with a frequency of 50 Hz, with a variable amplitude of vibration.

III.5.2 Drainage of the sandpack

The cement must be present only at the grain contacts in order to obtain homogeneous rock samples with predictable reservoir characteristics which are comparable to natural formations. The consolidation fluid (water or araldite/acetone), therefore, has to be present only at the grain contacts too. This can be achieved by creating an irreducible fluid saturation in the unconsolidated sandpack. The capillary forces then assure that the remaining fluid is located at the grain contacts only.

A connate fluid saturation in the sand is obtained by employing a thin layer of fine sized glass beads at the bottom of the consolidation vessel (fig 3.3), making use of the difference in capillary pressure characteristics of the fine and the coarser sandbeds, as shown in fig 3.4. If a certain pressure differential is applied to the total sandpack, the fine grained layer will remain fully saturated while the coarser fraction is drained almost to its irreducible saturation, provided no pressure jump exists over the interface dividing the two fractions.

First the consolidation vessel containing the compacted sand is fully saturated by imbibition from the bottom of the vessel. The flow-rate is slow to prevent the liquid from lifting the compacted sand. After the sand has been fully saturated, a pump is connected to the fine-sized glass beads compartment. The pump slowly sucks liquid from the fine-grained layer. The capillary pressure characteristics of the fine beads strive to maintain the saturation of the layer at 100 percent, so liquid is drained from the coarser grain pack located above.

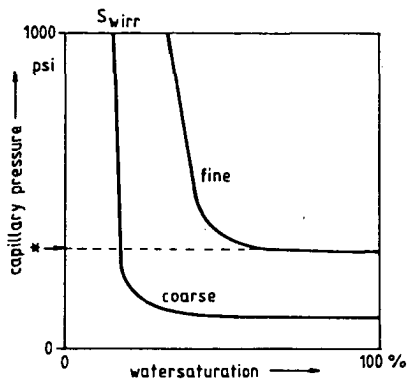


Fig 3.4
Capillary pressure curves of fine and coarser grains.
* → pressure exerted on the coarse sand by the fine beads during drainage.

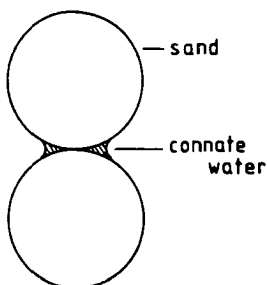


Fig 3.5
Water distribution after drainage.

Pumping liquid from the fine grain pack ultimately results in a connate water saturation in the sand grains that will be consolidated to form the rock sample. At that moment the saturation in the fine sized layer is much higher (fig 3.4), but this is irrelevant as the only function of the fine beads is to drain the coarse sand pack.

During the drainage process care has to be taken that the flow-rate of the pump remains small. The liquid has to be drained in a continuous flow from the sample. If a break-through of air towards the pump occurs, the drainage will stop and can not be restarted again; the sample then becomes useless.

The drainage process results in a homogeneous connate water saturation in the sandpack (fig 3.5). Drainage end-effects are only present in the thin layer of fine sized grains below the actual rock sample.

The connate water is located at the grain contacts. The quantity of water remaining in the pores after drainage amounts to 10 - 15 percent of the pore volume of the sandpack.

III.5.3 Consolidation methods

After the sand is given a connate water saturation, it is consolidated. This process is discussed separately for the three consolidation methods that were used.

Silicontetrachloride

The laboratory set-up for the consolidation of rock samples using silicontetrachloride is shown in fig 3.6. Because of the toxic properties of SiCl_4 , it is a closed circuit consisting of a nitrogen pressure cylinder, a vessel containing liquid SiCl_4 , a sample container and a vessel for the neutralization of the produced HCl . Safety switches are included in the set-up to be able to shut off the SiCl_4 -supply in case of emergencies.

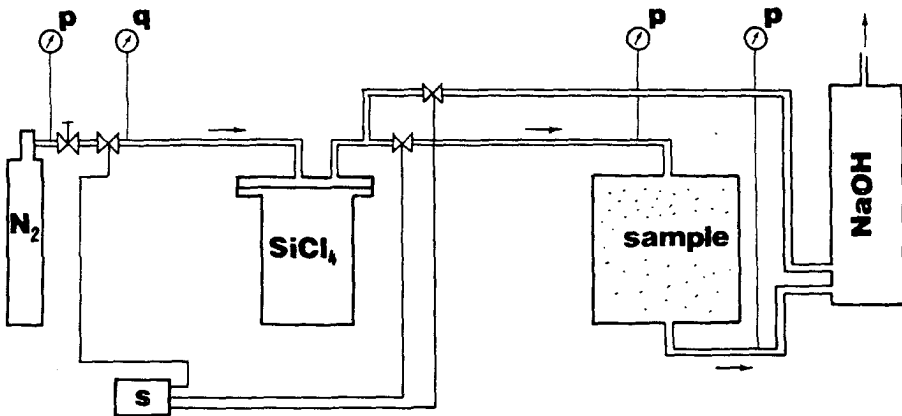
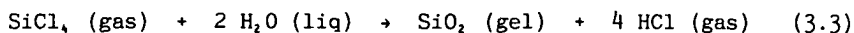


Fig 3.6 Experimental set-up for the consolidation of sand grains by the silica-lock method.
p,q = pressure and flow meters
s = safety switch

In the process nitrogen acts as a carrier gas for the different reaction products. From the pressure cylinder the nitrogen is lead through a vessel containing liquid SiCl_4 . The nitrogen carries SiCl_4 -vapour along through the unconsolidated sand. The sand is prepared beforehand so that it contains only an irreducible watersaturation. The connate water reacts with the SiCl_4 to form an amorphous silica cement.

During the consolidation experiments two distinct zones were observed in the sand:

- a zone of dry appearance where the reaction takes place:



- a yellowish zone moving ahead of the reaction front.

In this zone heat production occurs due to the dissolution of HCl in the connate water. HCl is formed as a by-product of the consolidation reaction. The acid is initially liberated into the gas phase and is carried along by the nitrogen carrier gas. Further downstream the HCl is dissolved in the water contained in the porespace, i.e.



The dissolution of HCl in water is an exothermic process; it is accompanied by heat production. The yellowish colour of the zone is caused by the presence of iron in the sand.

The amount of HCl formed at the consolidation reaction is large. The transformation of 1 ml water into amorphous silica produces 2.5 litre of HCl in the gas phase. As a result, the zone of HCl-dissolution rapidly moves away from the reaction front and the connate water in the whole sample is quickly saturated with HCl. The excess quantity of HCl is channelled through a vessel containing NaOH which neutralizes the acid.

The construction of synthetic rock samples using the silica-lock method is quite an elaborate process, especially for the large cubic blocks. Starting from the packing of the grains it takes just over a week in time to consolidate a large rock sample.

Araldite

As far as araldite cement is concerned the consolidation procedure is very simple. To make sure that the grains are bonded only at the grain contacts, a drainage technique is used as with the silica-lock method. The sand is fully saturated with an araldite solution and then drained to its connate fluid saturation.

The hardening process of araldite commences as soon as it is mixed with the hardener. This seriously inhibits a homogeneous drainage of the sample. After approximately 30 minutes the araldite is already too

adhesive to the grains and too viscous to be drained from the sample. Especially in larger specimens this results in a considerable difference in araldite content between the top and bottom of a sample. To overcome this, araldite is mixed with acetone. The resulting solution has a low viscosity and it retards the hardening process strongly. In this way an irreducible saturation can be obtained in the entire sample.

An additional advantage of the presence of acetone is the neutralization of the heat production during the hardening process of the araldite. The produced heat is effectively compensated by the evaporation of the acetone from the mixture, which is an endothermic process. During hardening, the sample does not noticeably become warmer.

Another advantage of the use of acetone is that it allows the amount of cement in the sandstone samples to be controlled. After drainage, the volume of liquid held at the grain contacts by capillary forces is virtually independent of the viscosity of the saturating liquid. As acetone can be mixed in any ratio with araldite, this ratio to a large extent determines the quantity of araldite at the grain contacts.

After the sand is drained to its connate water saturation with the araldite/acetone mixture, the layer of fine-sized beads is removed from the container. Air is flowed through, allowing the acetone to evaporate and the araldite to harden. The hardening process takes about three weeks for the large samples.

The smaller, cylindrical samples are dried in a heated air oven at 50 °C for maximum bondstrength. After three days in the oven these samples are completely consolidated.

Methylsilicate

Only small samples were produced to test a consolidation process using methylsilicate. The samples were prepared in glass tubes having a diameter of 39 mm and a length of 15 cm.

After compaction, the sand was saturated with a 1 N HCl-solution, the acid functioning as a catalyst for the consolidation reaction. The sand was drained to its connate fluid saturation level and methylsilicate was pumped very slowly through the tube. The flow provided an excess quantity of methylsilicate in the sand and it also removed the methanol, produced as a by-product of the reaction, from the sample.

The flow was stopped after approximately three hours and the sample dried by flowing air through the sand for four days.

The resulting synthetic rock sample was fully consolidated but very brittle; grains could easily be scraped off the sides of the sample. The brittleness of the sample probably resulted partly from the evaporation of methylalcohol from the hardening gel. The end of the reaction was hard to determine; successive experiments, however, allowing longer reaction times, still resulted in brittle samples. Another possibility is that the flow of methylsilicate through the sand partially replaced connate water, leaving less water and thus less cement at the grain contacts.

A combination of methylsilicate together with silica-lock was tested as an alternative method. First the sand was consolidated using methylsilicate, resulting in a homogeneous but brittle sample. After that, an additional treatment with the silica-lock method was applied to the same sample to give it strength. This did not prove to be successful. Problems were encountered during the saturation and drainage of the sample consolidated with methylsilicate. At first, saturation took place at normal rates but it slowed down considerably after a few minutes. Drainage of the sample afterwards failed almost completely, leaving a watersaturation of approximately 50 % of the pore volume instead of the usual 10 -15 % . It appeared that the silica deposited by means of the methylsilicate is not quite stable. The reaction appeared to be partly reversible; the dried silica cement absorbed water and became a gel again. The absorption of water caused the cement to swell, thus decreasing the permeability by partly blocking the pores. Permeability tests using a liquid permeameter confirmed the significant reduction in permeability.

The methylsilicate method, therefore, is not suitable to consolidate synthetic sandstones. The produced samples are too friable to be properly manageable. Moreover, the apparent tendency of the silica cement to absorb water again, thus turning into a gel, precludes the use of methylsilicate in combination with the silica-lock method as a consolidation process.

III.5.4 Selection of sand

The sand used to manufacture the rock samples is the commercially available "Maaszand" (purchased from Sigrano bv.). The sand is very pure and clean, consisting for 99.4 % of quartz with minor traces of Fe_2O_3 , Al_2O_3 , and K-, Na-, Ca-oxides. The matrix density of the sand is 2.65 gr/cc.

Four tons of sand have been sieved in four grain size fractions, using sieves of 106, 150, 212 and 300 μm . A sieve analysis of each fraction is shown in fig 3.7.

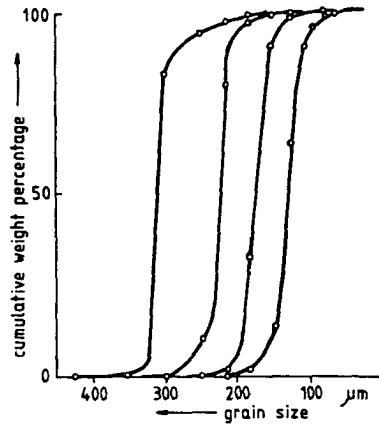


Fig 3.7
Sieve analysis of the four sand fractions used to manufacture rock samples.

The four fractions are very well to extremely well sorted. The medium grain size and the Trask sorting for the four fractions are:

fraction:	1	2	3	4
D_{50}	320 μm	230 μm	170 μm	130 μm
S_0	1.02	1.04	1.07	1.09

The Trask sorting is defined as $S_0 = \sqrt{(S_{25}/S_{75})}$, where S_{25} and S_{75} refer to the grain diameters at the cumulative weight fractions of 25 and 75 % in the sieve analysis. The roundness of the grains is subrounded to subangular.

III.6 Sample description

This section presents the results of the three consolidation processes. Scanning electron microscope photographs of the produced samples are shown and the samples are discussed in general. The specific rock properties of the samples are discussed in section III.9.

At the end of this chapter a summary is given, stating all advantages and disadvantages of the three consolidation methods.

Silicontetrachloride method

The construction of artificial sandstones employing the silica-lock method resulted in well-consolidated samples. The method effectively replaces the connate water present on the surface of the sand grains and concentrated at the intergranular contact points by a strong silica cement. The produced rock specimens have a high mechanical strength and have excellent reservoir characteristics.

Figs. 3.8 a,b and c are Scanning Electron Microscope (SEM) pictures of a sand consolidated with silicontetrachloride. The amorphous silica can be seen to form thin coatings on the sand grains and to be placed in small areas around the grain contact points. This is exactly what is desired to retain the reservoir characteristics of the sand pack. The pore structure is hardly affected by the cement.

The quantity of cement is directly linked to the water saturation before the silicontetrachloride treatment. Higher connate water saturations results in the formation of larger quantities of cement. Of the four different sand fractions used to manufacture rock samples, the fraction containing the smallest grains therefore was expected to have the highest cement content after consolidation due to its capillary characteristics. However, a change in cement content was hardly noticeable among the four grain size fractions. Addition of propanol to the connate water to minimize the surface tension of the fluid did not result in a significant reduction of the cement content either.

Fig 3.8a

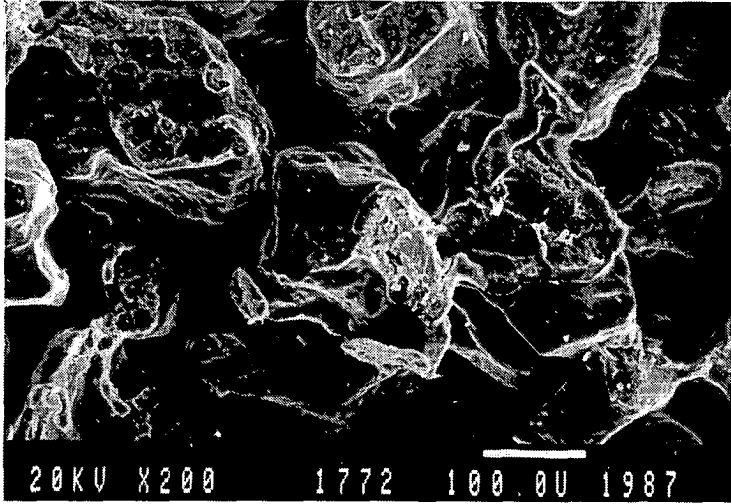


Fig 3.8b



Fig 3.8 SEM photographs of sand consolidated with silicon tetrachloride.
a. magnification 200 ×
b. detail, magnification 1200 ×
c. magnification 2000 ×.

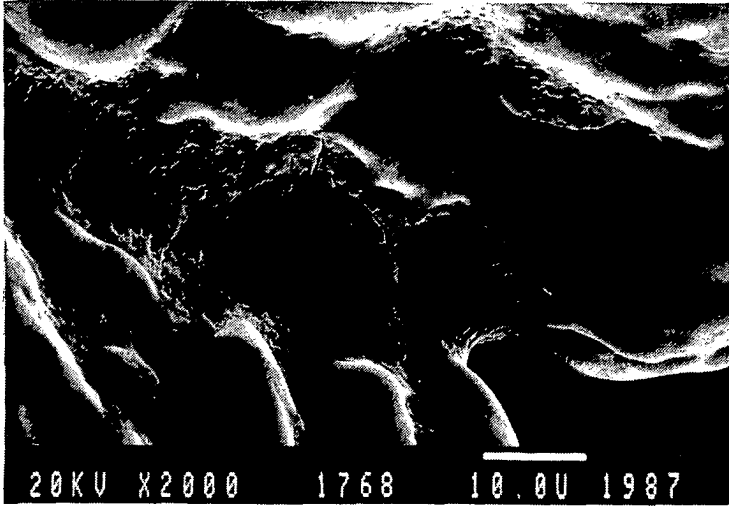


Fig 3.8c

The only way to increase the cement content of a sample seems to be to carry out several silica-lock treatments on the same rock sample. Each successive treatment increases the amount of cement in the sample and the procedure has to be repeated until the desired quantity of cement is reached.

In the cement itself fractures are present (fig 3.8 b and c). The cracks are caused by either the expansion of the silica gel in the first stage of the consolidation, or the shrinkage tensions due to the dehydration of the gel. The fractures are omnipresent; no cementbonds can be found which do not exhibit these cracks. Although all bonds are broken, the samples as a whole remain a coherent mass. No reduction in strength is observed, no grains come off the surface of the samples. It implies that the cracks only occur at the outward surface of the cement. The inner part of the cement remains intact binding the grains together.

Besides the cracked cementbonds, the samples also show fracture-like irregularities on a macroscopic scale. Specimens manufactured in narrow glass tubes often break into several pieces during consolidation. In larger specimens the irregularities are apparent as crack-like structures or disturbances in the packing of the sand grains. A more

detailed investigation into the nature and possible causes of these irregularities is given in the next section.

Although the fractures seemingly do not influence the strength and the acoustic properties of the rock specimens, they still make the samples less suited for acoustic research purposes. The presence of crack-like structures introduces inhomogeneities in the rock samples. The width of the fractures is very small and is not detected by the acoustic waves due to the wavelengths used in the acoustic experiments (.5 - 1 cm), but the lateral extent of the fractures may seriously limit a propagating wavefront. In any case, the results obtained from a cracked rock sample remain slightly suspect.

An advantage of the samples produced by the silica-lock method is that they are temperature-resistant, so that experiments under in-situ circumstances may be performed in the future.

Methylsilicate method

SEM-photographs showing a synthetic sandstone which is consolidated employing methylsilicate are given as figs 3.9 a and b.

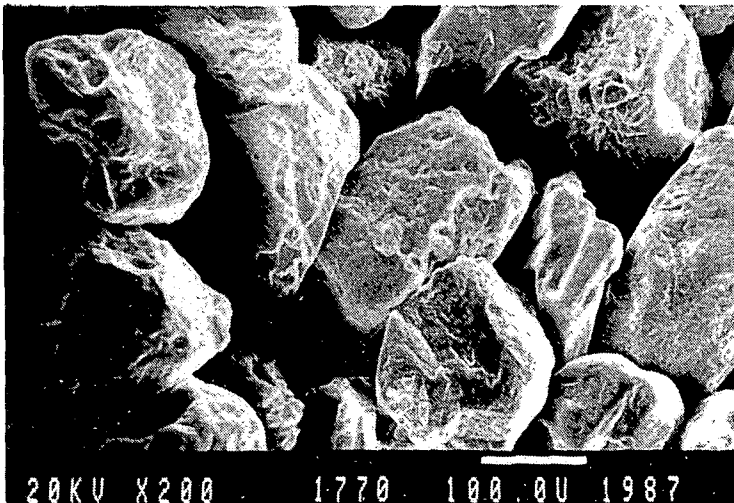


Fig 3.9a

Fig 3.9 SEM photographs of sand consolidated with methylsilicate.
a. magnification 200 x
b. detail. magnification 1000 x.

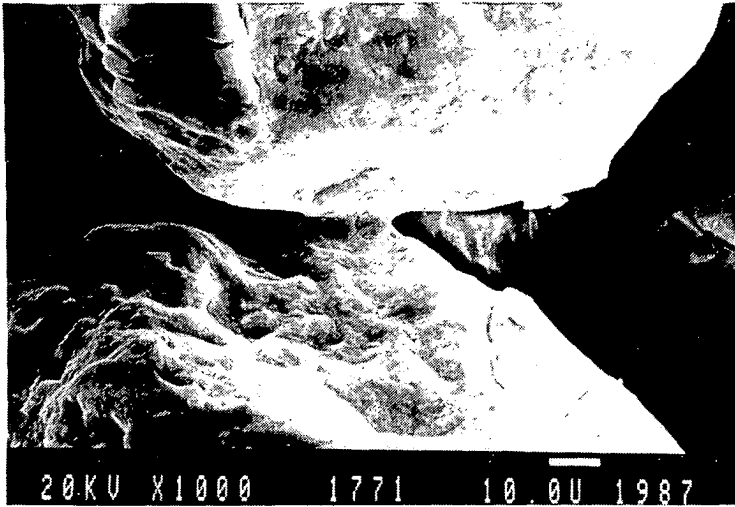


Fig 3.9b

As with the silica-lock method, the sand grains are covered with a thin coating of silica. But very little bonding material is present between the sand grains (fig 3.9b). This lack of cement explains the brittleness observed in the samples constructed using the methylsilicate process.

The grains as well as the preparation of the unconsolidated sand pack are identical for the silica-lock and the methylsilicate method. The absence of bonding material therefore has to be associated with the reaction process of the methylsilicate itself.

During the hydrolysis of methylsilicate, methanol is formed as a by-product of the reaction. The presence of this alcohol in the pores slows down the rate of hydrolysis until the reaction ultimately stops. To eliminate this problem the methylsilicate was pumped very slowly through the sandpack during the consolidation process. The fluid flow should carry the produced methanol away and remove it from the sand, so the alcohol no longer would obstruct the reaction. However, part of the methanol apparently dissolved in the connate water, thus lowering the surface tension and changing the capillary conditions at the grain contacts. As a result, not only the alcohol was removed from the sand by the fluid flow, but presumably part of the connate water too,

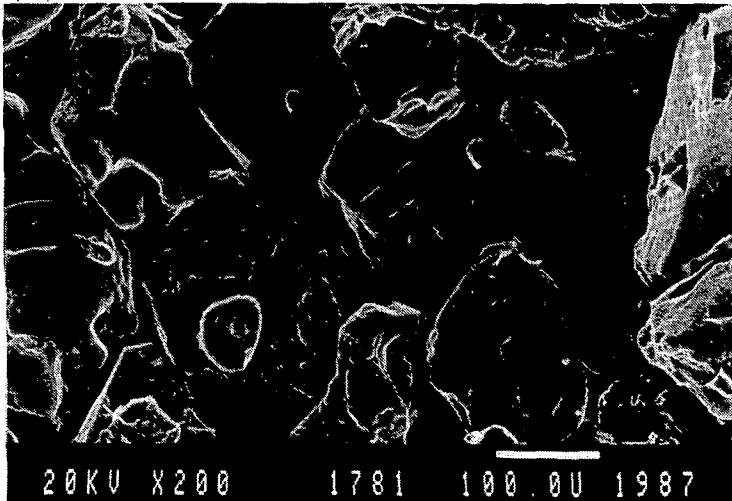
leaving little water at the grain contacts to be converted into silica cement. The cement itself also shows shrinkage cracks (fig 3.9b).

Araldite method

In comparison with the previous two consolidation methods, cementing the sand grains with araldite as a bonding material is relatively problem-free. The produced samples are well-consolidated and have a high mechanical strength. Figs 3.10 a and b are SEM-photographs of a sample. The araldite is present around the grain contacts and as coating on the individual sand grains, thus preserving the reservoir characteristics of the sand pack.

A disadvantage of the method is the completely different composition of cement and sand grains. Araldite is an epoxy resin while the grains consist of quartz. The overall sample is a two-component grain structure which may affect the prediction of certain reservoir characteristics. All bulk rock properties of the samples should therefore be measured explicitly instead of deriving them from relations between rock parameters given in the literature. Another disadvantage of araldite cement is that no experiments can be performed at higher temperatures. The cement is not heat-resistant; the samples can not be used for in-situ experiments. As opposed to the silica cement it is easy to produce samples solely consisting of araldite cement. It is thus possible to determine the properties of the pure cement.

Fig 3.10a



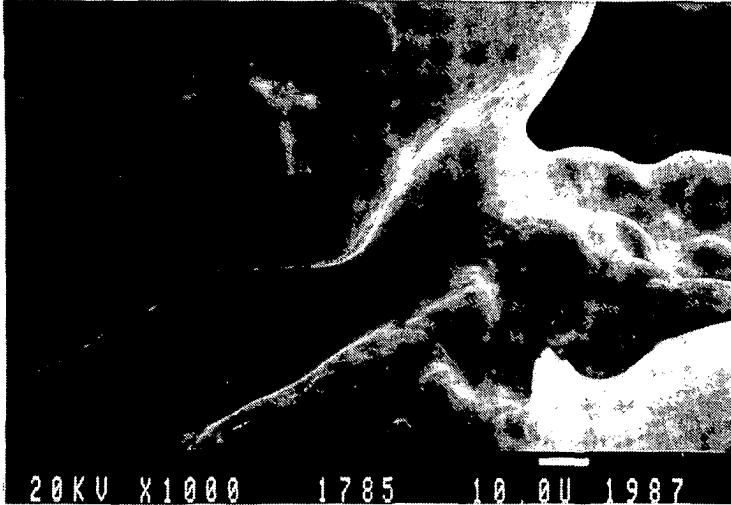


Fig 3.10b

Fig 3.10 SEM photographs of sand consolidated with araldite.
a. magnification 200 ×
b. magnification 1000 ×

The quantity of cement in the samples can be varied within certain limits by mixing the araldite and acetone in various proportions. The acetone is added to the araldite to retard the hardening process and to lower the viscosity of the mixture. After drainage of the fully saturated unconsolidated sand pack, the amount of araldite/acetone mixture remaining at the grain contacts is more or less constant at 10 - 15 % of the pore volume. The acetone evaporates from the mixture leaving the araldite to harden and form the cement. So the quantity of cement depends on the initial proportion in which the araldite was mixed with the acetone. The amount of cement can only be varied a few percent of the total bulk volume of the sample but this is enough to change the mechanical strength of the rock samples.

An attempt to construct a sample by saturating the sand with pure araldite with no acetone added failed because of early hardening. The sample would have had no porosity because all the pores would have been filled with araldite. This would have presented a good opportunity to study the effect of araldite cement in the sand. But the experiment failed because as soon as the araldite was mixed with its hardener, it began to harden and the sand would not saturate anymore.

Table 3.1 The advantages and disadvantages of the samples produced by the three consolidation methods.

(+ = advantage, - = disadvantage)

To all three methods applies:

- + sand grains are rock supporting
- + homogeneous cement distribution
- + homogeneous porosity and permeability distribution
- + samples not limited in size

consolidation method: silica-lock

- + hard sandstone sample
- + cement consists of silica
- + high-temperature resistant
- +/- amount of cement variable
- microscopic cracks in cement
- cement can not be produced separately
- crack-like irregularities in the samples
- consolidation method toxic

consolidation method: methylsilicate

- + homogeneous
- + cement can be produced separately
- very brittle
- consolidation reaction partly reversible
- cement not water-resistant
- no further consolidation technique can be applied
- consolidation method very toxic

consolidation method: araldite

- + homogeneous
 - + hard sandstone
 - + amount of cement variable
 - + cement can be produced separately
 - cement consists of araldite (an epoxy resin)
 - cement is not high-temperature resistant
-

Summary

The advantages and disadvantages of the samples produced by the three investigated consolidation methods are listed in table 3.1.

The consolidation method using methylsilicate is not suitable. The produced samples are too brittle and the consolidation reaction is partly reversible. Upon saturation with water, the cement swells which results in blocked pore throats.

The silica-lock method and the araldite method both produce well-consolidated sandstone samples. The resulting samples are well suited for an empirical approach to investigate the acoustic behaviour of porous rocks. The silica-lock method would have been best, if not for the presence of the inhomogeneities in the samples.

III.7 Irregularities in the samples using Silica-lock

The silica-lock method would have been an ideal procedure to construct artificial sandstones but for the presence of crack-like features in the samples. The features occurred merely as irregularities in the larger samples while thin cylindrical samples often broke up into several pieces. Numerous experiments were performed in an attempt to pinpoint the causes for this phenomenon and to solve the problem, but so far without success. The fractures in the samples appear to be inherently associated with the consolidation mechanism itself.

During the consolidation process the sand is subjected to several volume changes, viz:

- heating of the sand caused by the dissolution of produced hydrochloric acid in the connate water
- expansion due to the polymerization of the silica gel at the grain contacts
- shrinkage of the cement due to dehydration

The volume changes introduce tensions in the samples as a whole which in their turn cause the irregularities to appear. Although some of the tests successfully reduced the number of cracks their appearance could not be eliminated completely.

III.7.1 Description of the irregularities

The fracture-like features manifest themselves in a way depending on the geometry of the sample. Small samples break completely, while in larger samples the features are apparent merely as disturbances in the packing of the grains. The features do not always show but if present, they exhibit a regular pattern.

- thin cylindrical samples

Rock samples were constructed in long narrow glass tubes with an inner diameter of 3 centimeters. Short samples (± 10 cm) did not show any irregularities at all, but larger ones (± 36 cm) were fractured.

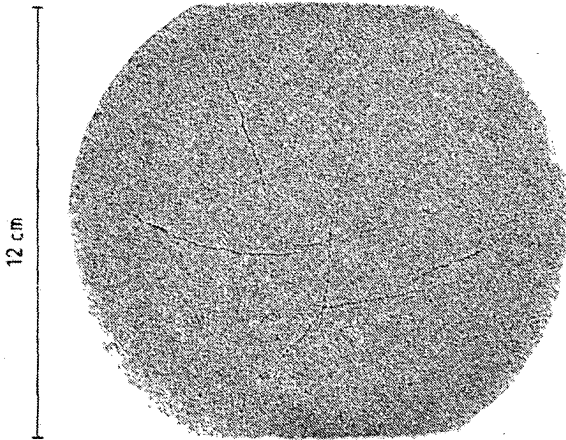


Fig 3.11 Crack-like irregularities in the samples produced with the silica-lock method.

After careful removal of the glass, the long samples appeared to be broken into 5 separate pieces, each about 7 cm long. All long samples manufactured in the glass tubes broke in this same regular pattern. In repeated experiments the location of the fractures could be predicted to within a distance of approx. 1 cm.

- medium-sized cylindrical samples

Larger samples (diam. 7 cm, length 30 cm) exhibited horizontal as well as vertical irregularities. The vertical features were radially distributed, usually with one dominant fracture-like feature right across the end surface of the sample. These specimens, however, were not completely broken. The fractures did not extend throughout the sample.

- large samples

Larger cylindrical samples (diam. 14 cm, length 15 cm) showed the same phenomena, although no dominant vertical fractures were present. The location of the irregularities was usually restricted to the outer edges of the sample; the inner core was free from cracks.

The very large cubic blocks with ribs of 40 cm were heavily fractured. The blocks showed a few dominant horizontal cracks but the general orientation of the features seemed to be induced by shrinkage tensions. It looked similar to the pattern that can be observed in dry crumpled clay surfaces on the earth. The location of the fractures was not restricted to the outside edges of the block either.

The fractures in the larger samples seem to be closed. Only very seldom is a clear gap visible at the location of the fracture. Rather, the fracture-like features make the impression of being a disruption in the orderly packing of the grains. The features are noticed by the missing of sand grains at the surface of the sample. After brushing the loose grains from the samples the cracks become visible. So it seems that the fractures are filled with sand grains but that the grains in the fracture plane are not cemented.

The continuity of the rock samples over the fracture planes was tested by drainage experiments on some consolidated specimens. The samples exhibited fracture-like features perpendicular to the flow-direction of the drainage. The samples were fully saturated and then drained to an irreducible watersaturation in the usual manner by pumping water from fine-sized beads beneath the sand samples. Most of the samples exhibited an evenly distributed saturation after drainage, indicating no significant uplifting of the sand body at the fractures.

III.7.2 Possible causes of fracturing

It is not clear at which stage in the consolidation process the irregularities develop. Usually the fractures become visible only after the sample is retrieved from its holder. It is unlikely that the features develop during the saturation or drainage of the unconsolidated sand. The regular pattern of the fractures excludes the possibility of irregular packing of the grains or an inhomogeneous water saturation in the sand after drainage. (A few times irregularities were observed in the sand after drainage, which developed into fractures during consolidation. But it occurred only twice so it seems to be purely coincidental.)

The irregularities, therefore, appear to develop during or shortly after the consolidation process. A test programme was started for better understanding the circumstances under which the consolidation takes place. In the experiments attention was focussed on the three possible origins of the fractures:

- thermal effects of the dissolution of HCl.
 - expansion of the sample.
 - shrinking of the cement bonds.
- Expansion and heat production during consolidation

Experiments were performed to monitor the lengthening and temperature variation of a sample during consolidation. The experimental set-up is shown in fig 3.12.

A perspex tube of 7 cm diameter and 30 cm length was filled with sand. The tube was greased on the inside and covered with a plastic foil to eliminate friction between the sand and the tube as much as possible. A perforated disc was embedded in the sand at a few centimeters from the top. The disc was connected to a micrometer which measured the elongation of the sample. A thermo couple was placed in the sand halfway from the top to measure the temperature inside the sample during the experiment.

At the top of the sample holder evaporized SiCl₄ was guided into the sand using nitrogen as a carrier gas. The produced HCl gas was removed at the bottom of the container.

It took ca. 6 hours for the sand to fully consolidate. The temperature and the displacement were recorded at intervals of 10 to 20 minutes.

The temperature in the sample is plotted versus time in fig 3.13. The graph depicts the local temperature at the tip of the thermo couple in the sand.

The rise in temperature is caused by the dissolution in the connate water of the HCl produced during the hydrolysis of silicontetrachloride. The dissolution of HCl causes a heat front to move through the sand in the direction of the gas flow. The heat front is observed as a yellowish zone moving ahead of the zone of consolidation. The front moves fast due to the large quantities of HCl produced and the relatively small amount of connate water present in the sand. It reaches the bottom of the sample in 49 minutes whereas the consolidation took approx. 6 hours to complete.

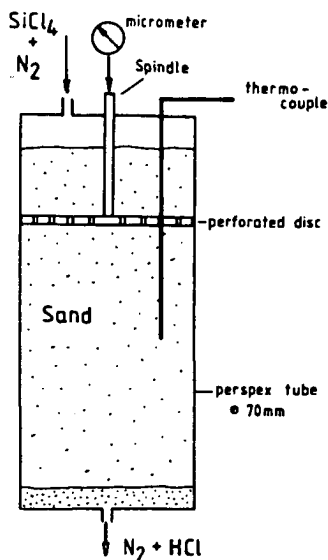


Fig 3.12
Set-up for the measurement of expansion and temperature changes during the consolidation process.

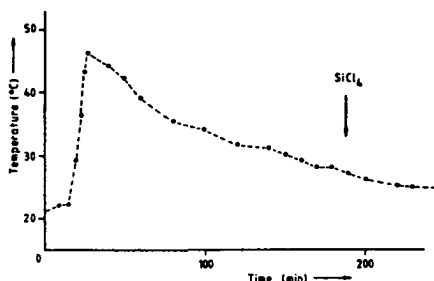


Fig 3.13
Local temperature in the sand during consolidation process. Arrow denotes time at which the consolidation front reaches the thermo couple.

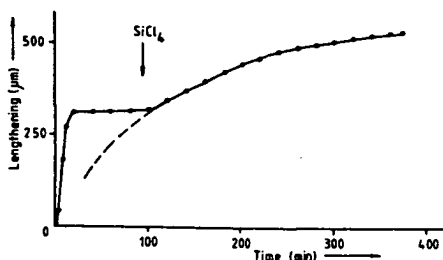


Fig 3.14
Axial elongation of the sample during consolidation. Arrow denotes time at which the consolidation front reaches the perforated disc.

After 27 minutes the HCl-front reaches the tip of the thermo couple. It is shown as a sharp increase in temperature in fig 3.13. At this moment the temperature rises to 46 °C as opposed to a room temperature of 21°C. After the HCl-front has passed the thermo couple, the sample cools down again. At the time the consolidation front reaches the tip of the thermo couple after approx. 180 minutes, the temperature in the sand at that particular location is decreased to ± 28 °C.

No change can be observed in the temperature curve as the consolidation front passes the thermo couple. It confirms that the consolidation reaction itself is not accompanied by significant heat production. A change in temperature in the sand is exclusively caused by the dissolution of the gaseous hydrochloric acid. At the time of consolidation most of the temperature effect has already disappeared.

The axial elongation of the sandstone sample during the experiment is plotted in fig 3.14. At the start of the consolidation the metal spindle connecting the perforated disc to the micrometer is heated by the passing HCl front. The extension of the spindle is recorded as a sharp linear increase in the elongation curve. After ca. 15 minutes the HCl heat-front has passed the disc. Thereafter no further change in elongation is recorded until the consolidation front passes the disc after about 100 minutes. This is accompanied by an increase in the elongation. As the consolidation proceeds the sample expands further until an elongation of 550 μm is reached as the sand is fully consolidated.

While still contained in the experimental set-up, the consolidated sample was saturated with water. A further extension of 80 μm could be noticed. This strange effect is probably explained by further relaxation of stresses built up in the sample during the expansion.

The expansion of the sand was confirmed by all other experiments using silicontetrachloride. An increase in volume was always evident. After consolidation the sand fitted in the sample holder very tightly and could be removed from it only by considerable effort. No reduction in length was observed at any time during the above or any other experiment.

The sample constructed in the test was very good. Apart from a few small irregularities at the bottom surface of the sample no fractures were present. (Of course the sample was broken at the location of the disc).

Expansion mechanism

As the consolidation front reached the perforated disc in the experiment the HCl heat wave had long since left the sample. But while the sand cooled down, it still continued to expand. To find an explanation for this effect a rock sample was prepared in a glass tube. Against the side of the tube a videorecorder with a magnifying objective was placed. The recorder monitored the consolidation process and stored it on tape.

Upon contact with SiCl_4 , the outer surface of the connate water was turned instantaneously into a solid silica layer (Fig 3.15). Following this initial rapid solidification of the outer surface, silicontetra-chloride slowly diffused through the silica layer. Then the inner water slowly solidified. This solidification of the inner water proceeds along two stages. First a silica gel is formed by the polymerization of the hydrous silica (ref. p. 56). Then the gel dehydrates into amorphous silica. It seems reasonable to assume that the polymerized silica gel occupies a larger volume than the initial volume of water at the grain contacts, which causes the sample to expand. This mechanism also may result in a separation of the individual grains.

The expansion of the water turning into silica gel itself was not visible on the video tape. But then the effect will hardly be noticeable on a grain sized scale.

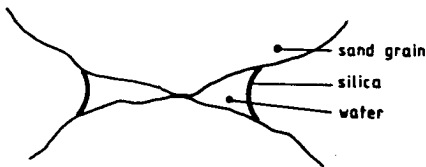


Fig 3.15
Consolidation of the connate water. Outer boundary is solidified instantaneously.

However, the tape seemed to indicate the appearance of cracks in the cement before the inner water was completely solidified.

This expansion mechanism also provides a plausible explanation for the cracked appearance of the cement

bonds while the total sample retains a high mechanical strength. The cracks are surface phenomena and the inner cement formed at the later stages of the reaction binds the grains.

- Shrinkage of cement

Another explanation for the cracked appearance of the cement bonds may be the shrinkage due to the dehydration of the silica gel. The gel

initially forms a honeycombe-structure containing small pores filled with water. The flow of dry nitrogen carrier gas through the sample causes this water to evaporate. The small pores induce strong capillary forces and upon evaporation of the water the structure collapses. The cement thus decreases in volume. This could explain the cracks in the cement bond, but not the crack-like features in the samples. It would imply that the irregularities are caused by shrinkage tensions in the overall sample, which in turn would imply that the total sample would shrink. This was never noticed during an experiment. The samples always expanded during the silica-lock process.

III.7.3 Attempts to reduce the effect of expansion of the samples during consolidation

Several experimental techniques have been devised to eliminate, or at least to neutralize the expansion effect. The tested methods are:

- using an irreducible HCl solution at the grain contacts in the sand,
 - using a sample holder containing a flexible wall during consolidation
 - consolidating under pressure.
- Consolidation with an irreducible hydrochloric acid saturation

An obvious method to remove the temperature effect from the consolidation process is to prevent the HCl gas from dissolving. Therefore the connate water has to be replaced by a saturated HCl solution. The consolidation proceeds exactly as before only this time hydrochloric acid instead of water is used to saturate and drain the unconsolidated sand. The technique works very well; no rise in temperature whatsoever was observed during the experiments. Employing the method also results in much improved rock samples. Real open fractures no longer occur, but irregularities in the samples are still not altogether absent.

- Consolidation using a flexible wall

An isotropic expansion will not introduce tensions in the rock samples. So by allowing the samples to expand freely in all directions, fracturing should be minimized. To this extent a flexible coating was placed

on the inside of the sample holder. The coating consisted of a 2 mm thick plastic foam. The pores in the foam could be compressed thus allowing the sample to expand. The inside of the sample holder was greased too to allow for axial expansion.

This technique also showed an improvement in the constructed samples, but still the samples were not perfect.

- Consolidation under pressure

An opposite technique is not to allow the sample to expand at all. The cement then expands into the porespace of the porous rock. The grains are not dislocated and no disruption of the orderly packing of the sand occurs. However, a high pressure apparatus to construct the samples in this manner was not available. The most that could be done, was to fill the sample holder completely with sand and firmly close the lid. Naturally this did not work properly; the forces introduced by the expansion were much too strong to be contained in a simple manner. The big blocks were manufactured in a cubic container. The sides of this container are 2 cm thick steel plates. During the consolidation of the sand they just bent outwards.

Uneven consolidation front

Some experiments were interrupted halfway through the consolidation stage to inspect the consolidation front. The tests were performed on medium sized cylindrical samples.

The front is not flat. It exhibits a protruding cone shape in the middle of the sand, while the outer sides stay behind. So the inner core of the samples is consolidated first. It expands while the sand at the outside is still unconsolidated. Due to the expansion the unconsolidated sand around the consolidated core is uplifted and fractures are generated at the outside of the samples.

This uplifting phenomenon was actually observed in some of the samples. It may also explain why the fractures in the cylindrical samples are restricted to the outside area and the samples are not completely broken.

III.7.4 Attempts to reduce the effect of shrinkage of the cement

The following attempts were made to eliminate the effect of the shrinkage of the cement upon the discontinuity features in the samples:

- influencing the capillary pressures in the sand pack and thus the amount of connate water.
- using a carrier fluid which prevents the cement from dehydrating, i.e. kerosene instead of nitrogen.
- repeating the consolidation process. Any cracks generated during the first consolidation are filled with cement during the second run.

- Reduction of capillary forces

In an attempt to influence the capillary forces in the sand, a small amount of propanol was added to the connate water. The propanol reduces the surface tension of the water which in its turn lowers the capillary forces. The use of propanol has several advantages:

- a small amount of propanol is needed to reduce the surface tension of water by aprox. 50 percent. (5 - 10 vol. percent)
- SiCl_4 reacts in a similar way with propanol as with water
- the capillary forces within the silica gel are reduced, resulting in less shrinkage of the cement
- the amount of connate water in the total sample is reduced

A reduction in the amount of connate liquid in the sand can therefore be expected as a result of the reduced surface tension. It means that more water should be drained from the unconsolidated sand in a drainage experiment. This, however, does not happen. The drainage process is only accelerated by the presence of propanol. The final amount of drained liquid is the same for water and a water/propanol mixture.

The reduction in surface tension of the connate water does not prevent the cement from fracturing either (fig 3.16).

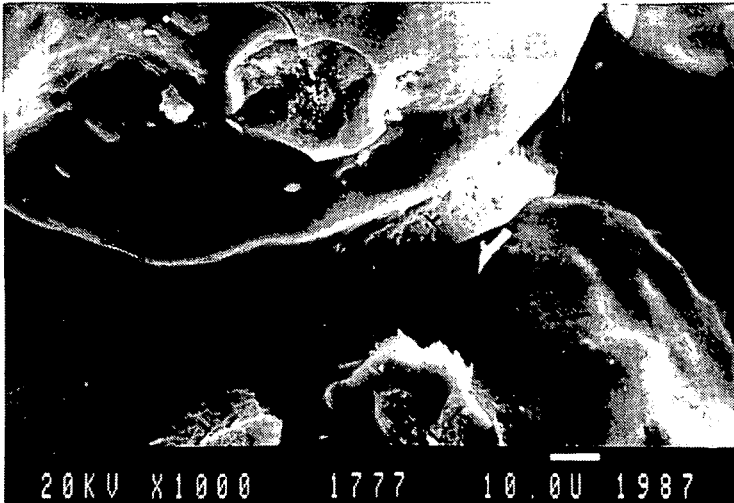


Fig 3.16 SEM photograph of sand consolidated with silicontetrachloride. Surface tension of the connate water has been lowered by the addition of 5 vol. per cent of propanol.

- Kerosene as a carrier fluid

Experiments were carried out using kerosene as a carrier fluid for the silicontetrachloride. SiCl_4 was dissolved in kerosene and the solution was pumped slowly through the sand pack. Using this technique, the quantity of SiCl_4 present in the sand can be accurately dosed by regulating the flow rate of the fluid and by controlling the dilution of the mixture. Furthermore a stable consolidation front can be obtained.

At any time during the process the sand is completely filled with fluid. The silica gel therefore does not dehydrate rapidly as is the case when dry nitrogen is used as a carrier of SiCl_4 . This may prove to have an advantageous effect upon the shrinkage of the bonds.

The large amounts of gaseous HCl formed by the consolidation were very troublesome in the tests. Cyclohexane was added to the kerosene to neutralize the HCl , but did not work properly. It did not neutralize all the produced HCl . Besides, it formed a reaction product which blocked the pores so the experiment had to be stopped prematurely.

The rock samples produced in the tests were too small to draw any definite conclusions but the technique may have the potential to

construct crack-free samples. But it is necessary to overcome the problem of the neutralization of the HCl. Possible neutralizers are of organic origin and are very toxic. The consolidation procedure therefore requires an extensive laboratory set-up and stringent measures have to be taken to control the process.

- Repeated consolidation

Some samples were consolidated twice. The idea behind these experiments was that no matter how the samples were fractured, the cracks would be filled with water and consolidate during a consecutive experiment. This however failed. Cracks in the cement were still present if not larger (fig 3.17).

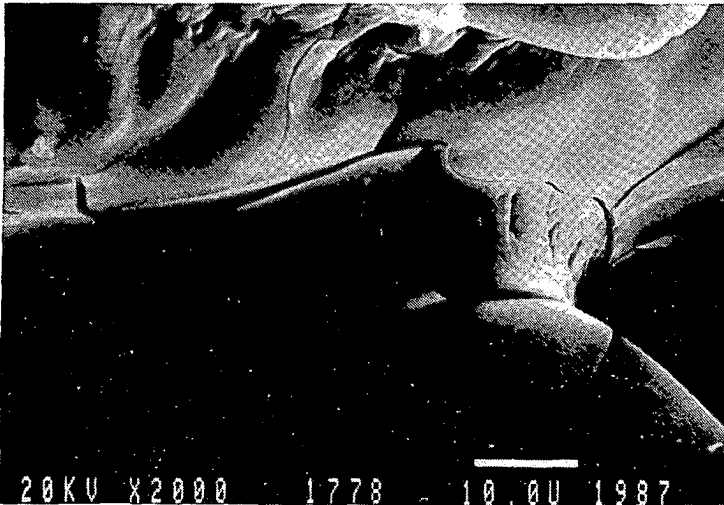


Fig 3.17 SEM photograph of sand consolidated twice with silicontetrachloride.

III.7.6 Conclusion

Recapitulating it can be stated that there are two possible sources for the crack-like features in the samples constructed using the silica-lock process:

1° expansion of the connate water as it turns into a silica gel while the outside is already solidified,

2° shrinkage due to dehydration.

The features most likely originate from the expansion of the sand pack. In all experiments the sand was observed to expand. A shortening of the rock samples was never observed.

Despite considerable efforts to change the physical conditions of the consolidation process, the problem could not be completely resolved. Still, the later samples showed a great improvement over the first ones. Open fractures were no longer present and the irregularities looked merely like discontinuities in the packing of the grains. Even samples without any irregularities were constructed but it was not possible to reproduce them properly.

Employing kerosene as a carrier liquid in the process showed promising results. However, the technique requires extensive laboratory utilities which were not available at the time. Therefore it was decided to discard the silica-lock method in favour of a consolidation process using araldite as a bonding agent. The latter technique did succeed in producing good rock samples.

III.8 Sample properties

In the following pages a description of the general characteristics of the synthetic reservoir rocks is given. Samples manufactured by the silica-lock method as well as araldite samples are treated.

- homogeneity

In order to determine the connate water distribution after drainage in an unconsolidated sandpack, the sample was cut into separate pieces of about 3 cm. The difference in density of each piece before and after drying yielded the water content.

The water was found to be very evenly distributed throughout the sample. The weight percentage varied from 3 % at the top to 3.5 % near the bottom. The saturation profile is given in fig 3.18.

The consolidation process transforms the fluid into cement. This is clearly evident from the density distribution in a consolidated sample shown in fig 3.19.

The sample was manufactured using the silica-lock method. The density of the rock was measured by a gamma-ray

transmission scanner at the Laboratorium van Grondmechanica in Delft.

A γ -source and detector were moved simultaneously along the sample. The attenuation of the γ -rays in the sample is proportional to the density of the rock. After the first measurement the sample was rotated over 90 degrees and the scan was repeated.

The density curves of fig 3.19 show an even density distribution with a slight increase towards the bottom of the sample. This agrees exactly with the connate water saturation shown in fig 3.18.

The measurements in the two perpendicular directions match very well, indicating no lateral density variations in the sample.

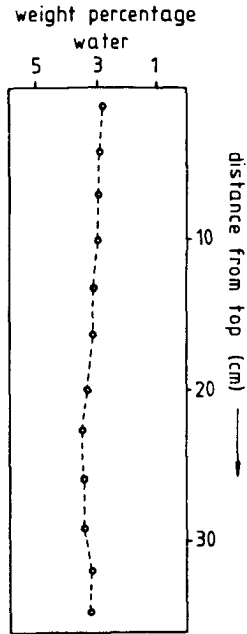


Fig 3.18
Water distribution in sand pack after drainage.

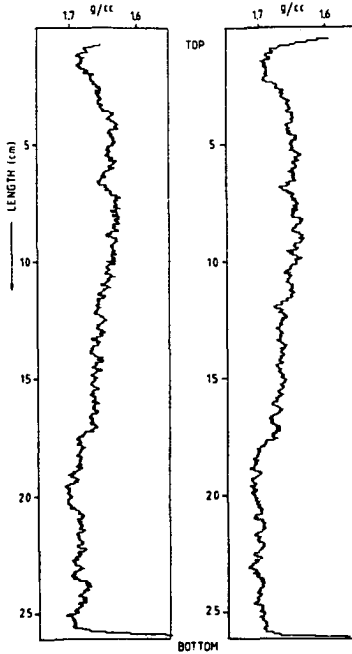


Fig 3.19
 Density profile of a sample consolidated with silicon tetrachloride measured by a γ -ray transmission scanner.
 The average density along the sample is shown for two directions at right angles.

- porosity

The porosity of granular rocks is mainly determined by the packing and sorting of the grains and by the amount of cement that fills the pores. In the case of the artificial samples, the packing and sorting of the grains are nearly optimum and little cement is present. The porosity of the unconsolidated sand therefore is about 40 % BV, which is reduced to approximately 37 % BV by the consolidation process. The porosity of the samples may vary slightly with the degree of packing of the grains. All produced samples have a porosity which lies between 35 and 40 % bv. Because of the extremely good sorting of the grains and the even distribution of the cement in the samples, the porosity is evenly distributed too. All pores are interconnected.

- permeability

Due to the large grains of the samples, the permeability is high. It correlates well with the empirical equation presented by van Baaren (1979), which relates the permeability to the porosity and the grain

size of a sandstone. The equation was tested on sandstone reservoirs in Nigeria, Venezuela, the North Sea area, Brunei and Serawak and shows good results with clean, non-shaly formations.

The permeability is calculated according to:

$$k = 10 * D_{dom}^2 * C^{-3.64} * \phi^{m+3.64} \tag{3.5}$$

where

k = one phase permeability, (mD)

D_{dom} = dominant grain size, (micron)

ϕ = porosity, (fraction of bulk volume)

m = cementation factor

C = empirical constant derived from the sorting

In fig 3.20 the permeability calculated by equation 3.5 is plotted versus the permeability of the samples measured with a liquid permeameter. To calculate the k -values from equation 3.5, a value of $m = 1.45$ was used. The original paper by van Baaren did not present an empirical constant C valid for sandstones as well sorted as these samples, but by extrapolation of his empirical range a value of $C = .6$ was derived.

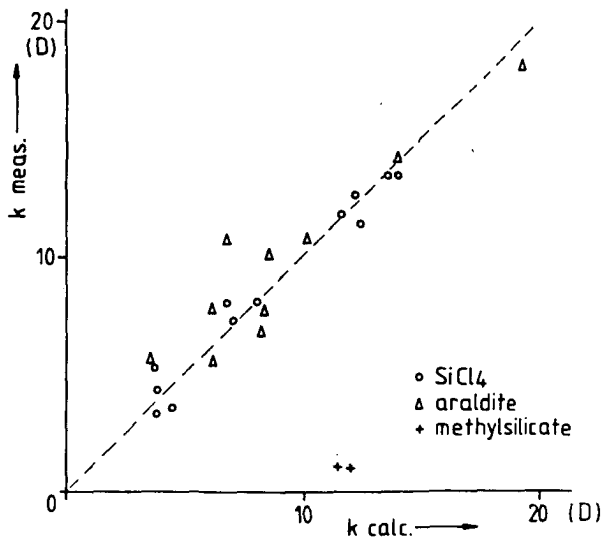


Fig 3.20
Calculated vs. measured permeability of artificial rock samples.

Permeabilities of samples produced by all three consolidation methods are plotted. The porosity of all samples is $37 \pm 2\%$ BV.

The measured permeabilities of the samples produced with methylsilicate are abnormally low. This is caused by swelling of the cement upon contact with water (refer p.64). The samples produced by the silica-lock and the araldite method show a very good correlation between the measured and calculated permeabilities.

- cement

The quantity of cement in the samples is low; i.e. $\pm 3\%$ bv for the silica-lock method as well as when using araldite cement.

Due to the very violent reaction of SiCl_4 with water, the silica-lock cement can not be manufactured separately. It is not possible to investigate the cement properties separated from the bulk sample.

Araldite cement on the other hand, is easily manufactured and accessible to physical measurements. The density of the cement is 1.12 g/cc. Its compressional velocity is 2115 m/s. The shear velocity of the cement is ± 1000 m/s.

- cap curve

A capillary pressure curve measured on a sample containing araldite cement is given in fig 3.21. The grain size of the sample is 130 μm .

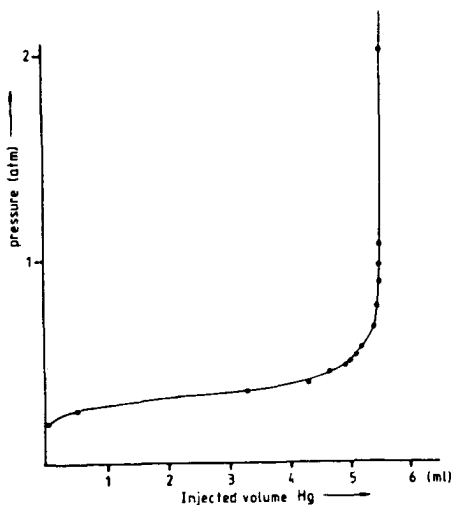


Fig 3.21
Capillary pressure curve of
a sample consolidated with
araldite.
Grain size = 130 μm .
Total pore volume = 6 ml.

As expected, little pressure is needed to start injecting mercury into the sample. The pore size is large, due to the relatively large grain size when compared to natural rock. After the initial influx of mercury into the sample, almost no pressure increase is required to saturate the sample fully. This implies that a very even pore throat distribution is present in the sample; all pore throats are sized about the same order of magnitude.

- cementation factor

The cementation factor of a rock is defined as:

$$R_o / R_w = \phi^{-m} \quad (3.6)$$

where

R_o = resistivity of the rock fully saturated with water

R_w = resistivity of the water

ϕ = porosity

m = cementation factor

The cementation factors were determined for the synthetic rock by resistivity measurements on fully water-saturated samples. The measured values range from 1.4 - 1.5 for both silica-lock and araldite cemented samples. These values compare well with the empirical values found for natural reservoir rocks ($m = 1.5$ for well sorted, friable rocks under in-situ circumstances).

- strength

The strength of the synthetic samples was tested on a uni-axial pressure bench. The vertical and horizontal strains were recorded versus the stress applied to a sample (fig 3.22)

The E-modulus and poisson ratio resulting from these measurements are:

Araldite cement: $E_{mod} \approx 4.2$ GPa , poisson ratio $\approx .25$

Silica-lock: $E_{mod} \approx 6.5$ GPa , poisson ratio $\approx .10$

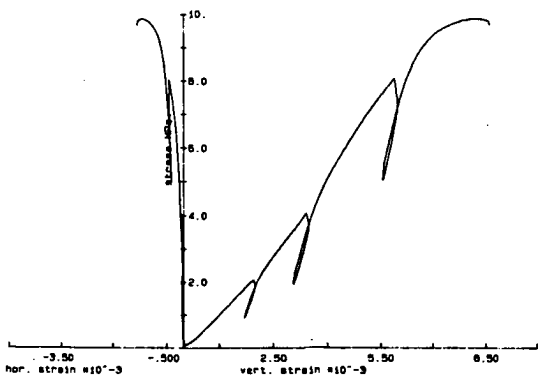


Fig 3.22
Uniaxial pressure test on
sample with araldite cement
Grain size = 230 μm .

- wettability of the samples

The wettability of the silica-lock samples with water is excellent. The wettability of the araldite cement samples with water is less, but improves after the samples are submerged for a while. Great care therefore has to be taken to saturate the araldite samples correctly.

- aging of the samples

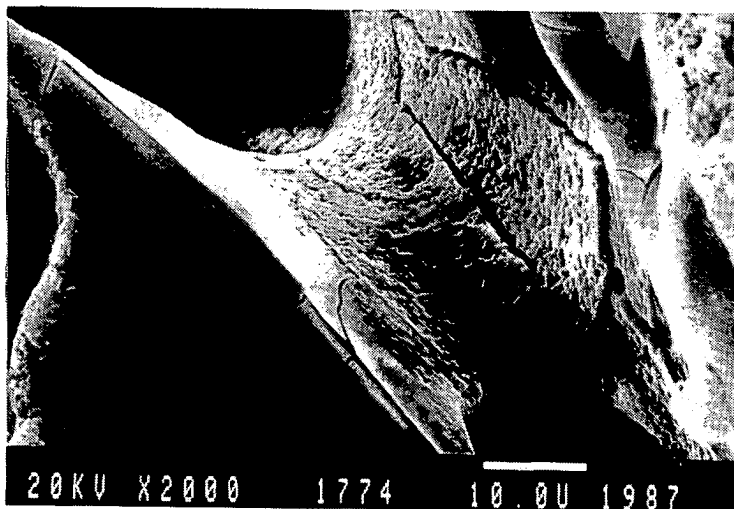
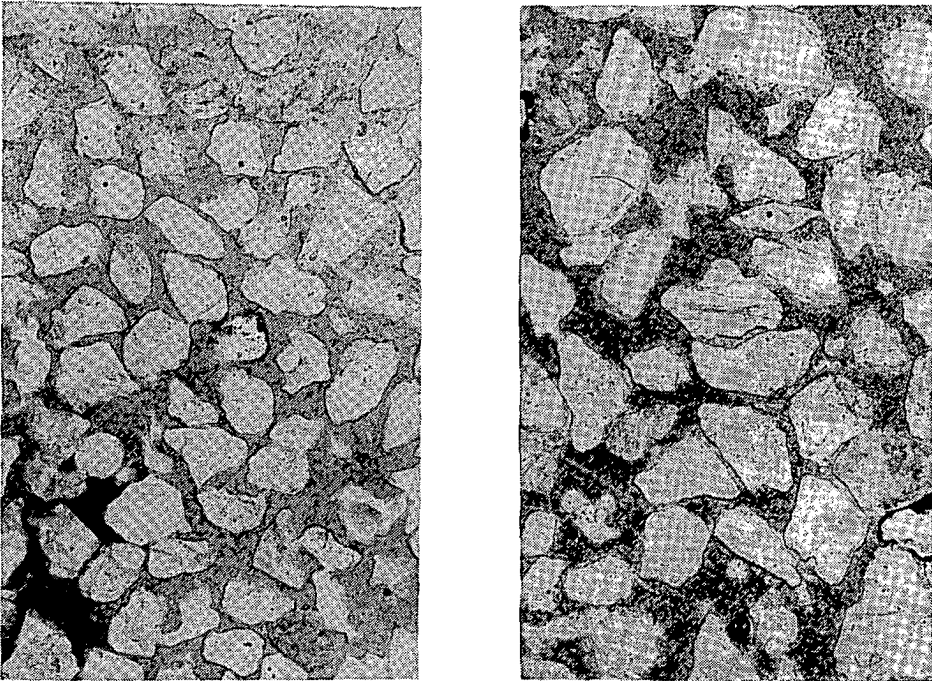


Fig 3.23 SEM photograph of silica-lock cement
showing similar cracks after a time lapse of 1 year
as shortly after consolidation.

The samples have not been observed to deteriorate with time. Measurements repeated after the samples were submerged for several months, always gave the same results. Fig 3.23 shows an SEM photograph of a cementbond produced by the silica-lock method, after the sample was left dry for approximately 1 year. No noticeable changes exist between this cementbond and a bond photographed shortly after consolidation (fig 3.10c).

III.9 Comparison of artificial samples with natural rock

The previous section showed that the properties of the produced samples correlate well with those of natural reservoir rock. Relationships between rock parameters of natural reservoirs also apply to the artificial rocks.



A

B

Fig 3.24 Thin sections of sandstone samples.
a. Nivelstein sandstone
b. Artificial sandstone

Figs 3.24 a and b show thin sections of a natural core and a sample containing araldite cement. The natural core was taken from the outcrop of the Nivelstein Sandstone in Limburg, Holland. The sandstone is very well sorted and contains no shale.

Both rocks have a porosity of around 37 % BV. Comparing the two rocks, it can be concluded that the artificial sample is at least as well packed as the natural rock. No bridging of the grains to form large pores is present. The pore structure of both rocks is alike.

A characteristic property of natural rock is that its acoustic velocity increases with pressure applied to the rock. It is generally assumed that this phenomenon is related to improved grain-to-grain contacts caused by the closing of microcracks under pressure. Initially, the velocity rapidly increases with pressure. Then it levels off until it reaches its end value asymptotically.

The phenomenon is clearly shown by fig 3.25a, where the axial velocity has been plotted versus the applied uniaxial pressure. The core was taken from the Eselführter Sandstein, which is a very homogeneous rock. The rock has a high shale content.

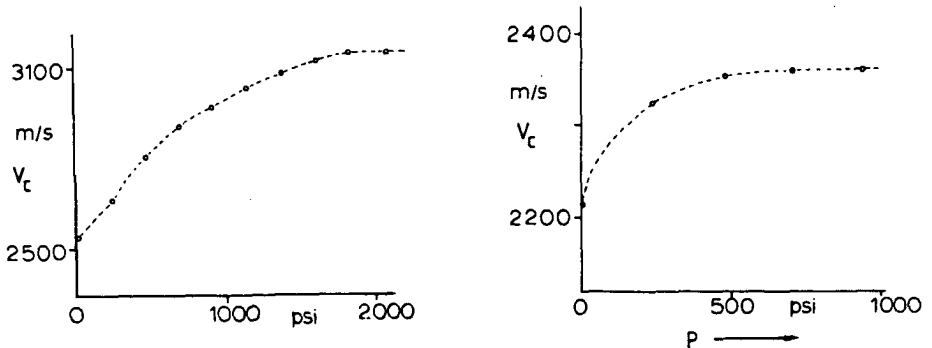


Fig 3.25 Compressional velocity versus uniaxial pressure.
a. Eselführter Sandstein
b. Artificial sandstone (Silica-lock)

Fig 3.25b shows the same experiment, but now performed on a sample constructed with the silica-lock method. The artificial sample shows the same phenomenon. Araldite cement samples also exhibit this same characteristic.

Summarizing it can be stated that the artificial rock samples, produced by the laboratory methods developed during the course of the research project, exhibit most of the required characteristics.

The silica-lock method and the araldite method both produce well consolidated sandstones. The properties of the samples can be controlled and are homogeneous throughout the sample. Slight inhomogeneities are introduced in the samples by the silica-lock method (the crack-like discontinuities), but these irregularities appear not to influence the acoustic response of the samples. The araldite samples have the disadvantage that they are not heat-resistant.

The artificial samples exhibit the same petrophysical characteristics as natural reservoir rock and they are therefore suitable for acoustic research. Results obtained from the synthetic rock samples are expected to be applicable to natural formations.

IV. MODELLING OF ACOUSTIC WAVETRAINS

IV.1 Introduction

The interpretation of acoustic signals recorded during acoustic experiments can be very complicated. Mathematical models which predict the received signals then are very useful to interpret the measurements. A comparison between the recorded and the calculated wavetrains may greatly simplify the evaluation of the received time traces. Modelling also may help to determine the optimum experimental configuration to enhance certain features to be investigated.

For these purposes two models were developed which simulate the acoustic measurements performed in the project. The models use the Biot theory to describe the wave propagation in the sandstone block. Two versions of this theory are used, which lead to the two different models. One model uses the high frequency limit of the Biot theory. In this high frequency limit the sandstone effectively reduces to a lossless porous medium. This model was developed by de Vries (1985). It calculates the acoustic response by the Cagniard-de Hoop technique. The obtained solution is exact and requires little computing time, but the model does not include interesting formation properties such as permeability. Therefore a second model was developed which uses the full frequency range of the Biot theory, including dispersion and attenuation. The pressure-time histories are calculated using a Fourier-Bessel approach.

The configuration of both models is similar to the experimental set-up; a pair of transducers is located in a layer of water above a flat block of sandstone. The models compute the wavetrain recorded at the receiver when the transmitter sends out an acoustic pulse.

In the following, a short literature review of wave propagation in porous media is given first. The Biot theory, being the one most appropriate for our experiments, is included and the influence of certain formation parameters upon the wave propagation is investigated theoretically. Then the mathematical models are discussed. The effect of formation characteristics on the calculated wavetrains is shown and numerical results are presented for various measurement configurations.

IV.2 Wave propagation in porous media

Porous rock consists of a dense packing of solid grains with intergranular pore space. The grains are cemented together forming a skeleton. The intergranular pore spaces are usually interconnected and allow fluid to flow through the rock.

In the theory of wave propagation several approaches towards the modelling of porous media are made. One approach is that the skeleton of a granular material resembles a packing of spherical particles in its response to stresses. Another proposed model for porous media consists of a continuous matrix containing a low concentration of inclusions.

The porous medium used in the granular skeleton model closely resembles real reservoir rock. It consists of a skeleton formed by a packing of spherical particles. The pores within the granular skeleton are interconnected and filled with a fluid. The elastic constants of the skeleton can be calculated from the properties of the elastic grains and the known packing geometry. Gassman (1951) derived an expression for the bulk modulus of compression (and thus the compressional wave velocity) in terms of porosity and the bulk moduli of the various components. In this theory the relative motion between fluid and skeleton during the passage of an acoustic wave is neglected. The elastic constants are computed for static stresses.

A general theory of wave propagation in linear elastic two-phase media was formulated by Biot (1956a,b). The two-phase medium consists of an elastic solid matrix fully saturated with a viscous fluid. The theory decouples the average motion of the solid and fluid part of the rock. Energy dissipation is related to the relative motion between the rock matrix and the viscous pore fluid during the passage of an acoustic wave. The theory treats the full frequency range and yields wave speeds as well as attenuations. A fundamental result of the Biot theory is the existence of three distinct bulk waves in a fluid-filled porous and permeable solid medium: a fast compressional wave, a shear wave and a slow compressional wave. In the low-frequency limit the Biot theory agrees exactly with the Gassman equations (Geertsma and Smit, 1961).

A different approach towards the modelling of porous media is that of a continuous matrix containing a low concentration of inclusions. The

model is applicable to rocks containing isolated pores as well as to suspensions of solid particles in fluids. In these models effective bulk moduli on a macroscopic scale are calculated for the porous medium. (Walsh 1966, O'Connell and Budiansky 1974, Kuster and Toksöz 1974).

As a model of reservoir rocks the solid matrix with isolated inclusions has serious limitations. Since interaction among inclusions is not incorporated the model does not allow fluid flow from one pore into another, which is one of the major characteristics of real reservoir rock. Such 'effective medium' theories cannot predict the two distinct compressional waves that are given by the Biot theory and that have been verified experimentally (Plona, 1980). Furthermore Johnson and Plona (1982) showed that the nature of the grain-to-grain contacts can have a large effect on the acoustic properties of a porous material. This would imply that 'effective medium' theories which do not explicitly take into account the grain-to-grain contacts can only be of limited usefulness.

Apart from the wave velocities, attention has been focussed in the literature on energy dissipation of waves propagating through porous rock. Several attenuation mechanisms have been proposed, such as matrix anelasticity, frictional dissipation at the grain boundaries, relative motion between fluid and solid, squirting phenomena, scattering and viscous relaxation. Each of these mechanisms may be more or less important depending upon the physical circumstances. Johnston et al. (1979) have given an extensive review of proposed attenuation mechanisms in relation to laboratory measurements.

In this thesis we will use the Biot theory as a basis to interpret the acoustic measurements on rock samples. The experiments have been carried out at high frequencies, i.e. $f = 500$ kHz and the rock samples under consideration have high porosities and permeabilities. Under these circumstances fluid flow as described by Biot gives an important contribution to the overall attenuation (Stoll and Bryan 1970, Johnston et al 1979). The present study is carried out in an empirical way by comparing the acoustic responses of different rock samples of which the properties are known in detail. Therefore the absolute determination of attenuation coefficients ascribable to the various physical mechanisms is not of primary interest here. It is only required that the attenuation due to mechanisms other than fluid flow be not excessively large

and not change appreciably over the range of rock samples measured (this condition can be checked by measurements on dry samples). It is then justified to interpret the results of the measurements in terms of the Biot theory.

IV.2.1 Biot theory

A general theory of wave propagation in linear elastic two-phase media was presented by Biot in 1956. This theory has been widely accepted and many authors have used it to interpret their measurements, among others: Wyllie et al 1962, Yew and Jogi 1976, Johnson et al 1982, Berryman 1980, Ogushwitz 1985. Several others have used it as the basis for their own work: Geertsma and Smit 1961, Stoll and Bryan 1970, Berryman 1981, Feng and Johnson 1983. In recent years the theory received a strong impetus when the slow P-wave predicted by Biot was verified experimentally. Plona (1980) observed the slow P-wave in an ultrasonic transmission measurement performed on sintered glass beads. His results have been identified by Berryman (1980,1981) with the Biot theory. Van der Grinten et al. (1985), van der Grinten (1987) observed the second compressional wave in shock tube experiments on artificial sandstone samples.

In the Biot theory, the porous solid consists of a skeleton or aggregate which is statistically isotropic. It contains a fluid that fills the interconnected pore space. The skeleton is made of an elastic solid. It is assumed to be macroscopically homogeneous; i.e. the aggregate is made out of elements which are small relative to the wavelength of the waves and in turn the size of the pores is assumed small compared to the size of an element. This presents an upper limit to the frequency for which the theory is valid.

Biot treats both the individual and coupled behaviour of the frame and pore fluid. Fluid flow in the pores is described by Darcy's Law. Energy dissipation is caused by the flow of the viscous pore fluid as it moves relative to the frame during the passage of an acoustic wave. The model predicts that wave velocity and attenuation in a porous rock depend on frequency, the moduli of the constituents of the rock, the viscosity of the pore fluid and on porosity, grain diameter and permeability.

The theory predicts three distinct waves:

- a fast compressional wave corresponding (approximately) to in-phase motion of the skeleton and pore fluid.
- a slow compressional wave corresponding (approximately) to out-of-phase motion of the skeleton and pore fluid.
- a shear wave propagating in the solid with an inertial contribution from the pore fluid.

A brief numerical formulation of the Biot equations is given in appendix A.

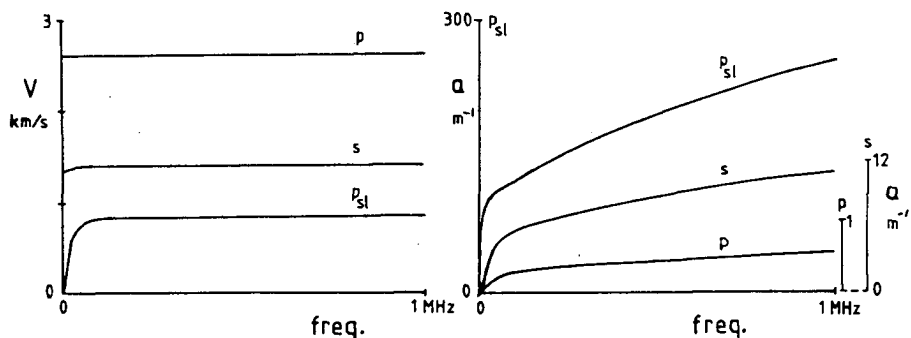


Fig 4.1 Velocity and attenuation of fast P-, slow P- and shear wave versus frequency, according to Biot theory. Formation parameters are listed in Table 4.1.

An illustration of the wave propagation through a porous formation calculated with the Biot theory is shown in fig 4.1. The equations given in appendix A were used. The velocity and attenuation have been plotted versus frequency for the fast P-, the slow P- and the shear wave. The skeleton and fluid properties used in the calculations represent a consolidated sandstone with water-filled pores. The formation properties are listed in Table 4.1.

The fast compressional wave is non-dispersive. Its velocity is virtually independent of the frequency. The attenuation is low. The shear wave is slightly dispersive in the low frequency range (up to ± 70 kHz. for this particular formation). The model predicts a higher attenuation for the shear than for the compressional wave. The slow P-wave is very dispersive at low frequencies. Its speed levels off too for higher frequencies. The attenuation coefficient is high.

IV.2.2 Formation parameters

The purpose of acoustic logging is to derive information about the logged reservoir from the recorded wavetrains. It is therefore necessary to relate the physical properties of the rock to the quantities governing wave propagation. The Biot model is very well suited for this approach. Its equations are directly expressed in physically meaningful formation parameters. Assuming a Biot-type wave propagation it is therefore possible to simulate numerically the influence of a specific rock parameter on the wave characteristics.

Table 4.1. Formation parameters

<u>pore fluid</u>		
K_f compression modulus		.225 E10 N/m ²
ρ_f density		1000 kg/m ³
η viscosity		1 E-3 kg/msec
<u>skeleton</u>		
K_s compression modulus of the grains		.379 E11 N/m ²
K_b compression modulus of the skeleton		.453 E10 N/m ²
N shear modulus		.37 E10 N/m ²
ρ_s density of the grains		2650 kg/m ³
ϕ porosity		36.5 % BV
ϵ tortuosity		2.48
k permeability		1 E-12 m ²
T surface permeability		0.
δ structural factor		$\sqrt{8}$

A total number of eleven variables enters Biot's formulae. These parameters however, cannot be varied independently. A change in porosity for instance, will have an influence on the bulk modulus of the aggregate too. The relations between the rock parameters will have to be accounted for if the formation model is to be realistic.

In the following sections, the effect of two important reservoir properties, the porosity and permeability, on the wave propagation are investigated numerically according to the Biot theory.

- Porosity

The amount of porosity influences the frame moduli of a formation which in turn determine to a large extent the velocities of the three bulk waves. A change in porosity thus has a large effect on the wave speeds in a porous rock.

This is evident from fig 4.2 where the velocity of the fast P-, slow P- and shear wave are plotted versus porosity. In constructing this plot the version of the self-consistent theory of Berryman (1981) has been used to provide the relationship between the porosity and the frame moduli.

The tortuosity needed in the calculations is given by $\epsilon = \phi^{1-m}$, where $m = 1.8 =$ cementation factor. (Perez-Rosales 1982)

For convenience the relation between the porosity and the permeability has been modelled by the Kozeny-Carman relation (Lambe and Whitman 1969) in this example:

$$k (1 - \phi)^2 / \phi^3 = k_0 (1 - \phi_0)^2 / \phi_0^3, \text{ with } k_0 = 1 \text{ Darcy at } \phi_0 = .20.$$

The other parameters are as listed in Table 4.1.

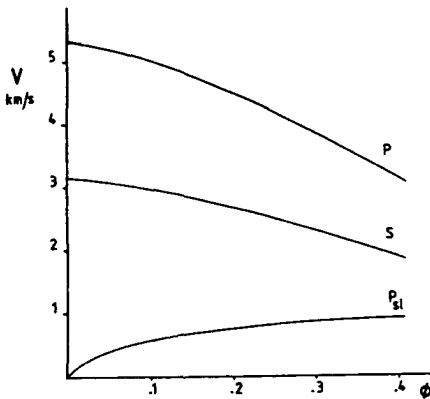


Fig 4.2
Velocity of fast P-, slow P- and shear wave vs. porosity

- Permeability

Another important parameter for oil- or gas-producing reservoirs is the permeability. To ensure that the large porosity effect does not obscure the influence of the permeability on the wave propagation, the porosity is kept constant in the following example. Instead the permeability is varied by changing the size of the individual quartz grains making up the skeleton. The permeability then changes according to (van Baaren, 1979):

$$k = 10 D_{dom}^2 C^{-3.64} \phi^{m+3.64} \quad (4.1)$$

where D_{dom} = dominant grain size, $C = .7$ = constant related to sorting, ϕ = porosity and m = cementation factor.

The influence of the dominant grain size and permeability is shown in fig 4.3. It is assumed that the bulk modulus of the skeleton K_b remains constant for varying grain sizes. The grain size parameter 'a' occurring in the frequency dependent dissipation factor $F(\kappa)$ (eq. A.19) is taken to be $1/3$ of the grain size (Stoll 1974). The plotted range in grain diameters (50 - 350 μm) corresponds to a permeability range from 0.38 to 18.6 Darcy.

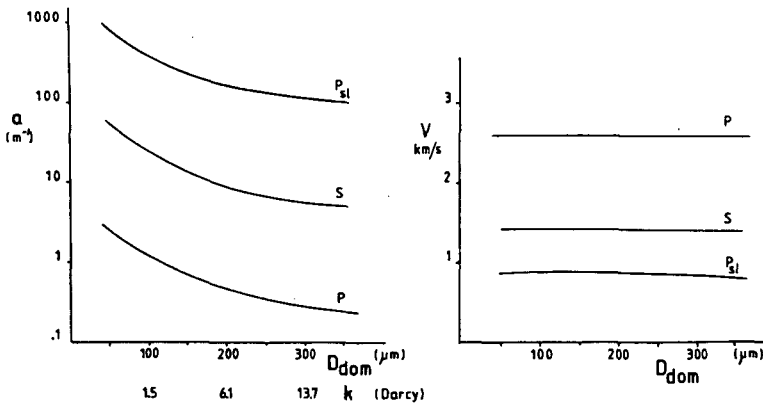


Fig 4.3 Dominant grain size (and permeability) vs. velocity and attenuation of the bulk waves according to Biot.

The velocities of the three bulk waves are hardly affected by the permeability. Only the slow P-wave, which is the one least accessible to measurement shows a slight decline in velocity with increasing grain size. The attenuation coefficients however change significantly over the range of plotted permeabilities.

IV.3 Modelling of acoustic waves in a liquid/porous solid configuration with a flat interface.

Two mathematical models have been developed which predict the received acoustic signals in our measurements. The configuration of the models is similar to the set-up used in the measurements under atmospheric conditions. It consists of a flat porous rock submerged in a liquid. The emitting and receiving transducers are located in the liquid above the block.

The propagation of waves in the porous rock is described by the Biot theory. Two distinct cases are treated:

- the full frequency range including dispersion and attenuation of the bulk waves due to fluid flow.
- the high frequency limit of the theory.

In this high frequency limit of the Biot theory energy dissipation due to fluid flow in the pores becomes negligible. The porous solid effectively reduces to a loss-less medium. This model is developed by de Vries (1985).

Both models calculate the pressure response in the fluid at the receiver due to the excitation of a monopole point source. A convolution of this system response with a known source wavelet then yields the desired acoustic trace. The models predict the arrival time and pulse shape of the various waves arriving at the receiver; i.e. the direct and reflected waves in the fluid, the shear and compressional waves in the solid and the surface waves if present.

In the high frequency limit the solution is obtained by the Cagniard-de Hoop technique. The solution is exact and requires little computer time. However, the model does not include attenuation due to fluid flow and thus permeability of the rock, as given by the full Biot theory.

The model incorporating the full frequency range on the other hand, includes the full Biot theory. It calculates the pressure response at the receiver by way of an Fourier-Bessel approach. It models the effect upon the recorded wavetrain of all the formation parameters occurring in the Biot theory. The exact solution of the Cagniard-de Hoop technique allows to check the Fourier-Bessel approach.

IV.3.1 Configuration

The configuration of the models is similar to the experimental set-up. A block of porous rock is submerged in a liquid. The liquid is taken to be a homogeneous, ideal fluid. The porous solid is a macroscopically homogeneous and isotropic elastic medium with fluid-filled pores. The fluid in the pores does not have to be similar to the fluid above the porous solid. To avoid confusion the half-space filled with liquid above the porous block will be denoted by the subscript L(iquid) while the fluid in the pores will be given the subscript f.

The interface between the liquid and the porous rock is a flat plane. Besides by the formation parameters, the characteristics of the interface are determined by the communication between the fluid in the pores of the solid and the liquid above the block. It can be characterized by open pores, sealed pores or some situation in between.

The liquid and the porous solid are both taken to be half-spaces (i.e. $0 < z < \infty$ and $0 > z > -\infty$ respectively). In the experiments this condition is approximated by placing a thick layer of water above a block of large dimensions. Any acoustic reflections from the surface of the water or the sides of the block then arrive outside the time interval of interest.

The transmitting and receiving transducers are both located in the liquid. The pressure response at the receiver is then equal to the sum of the direct wave between transmitter and receiver through the liquid, the reflected wave at the interface and the refractions from the porous medium.

Cartesian coordinates are defined with the origin 0 at the interface. The z-axis is taken perpendicular to the interface, pointing upwards into the liquid.

The transmitter is located at $z = h_t$, ($h_t > 0$) and the receiver is located at $z = h_r$, ($h_r > 0$)

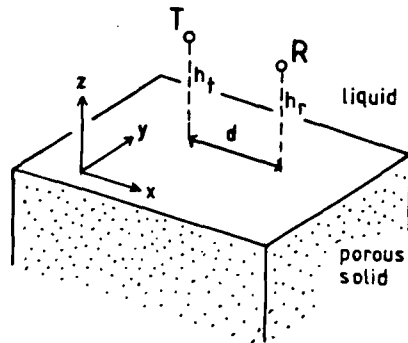


Fig 4.4 Geometric configuration

IV.3.2 The wave equations

In the liquid half-space the pressure is the fundamental unknown. This is the quantity that is measured by the receiver in the experiments. In the liquid the total acoustic wave field is equal to the superposition of the incident field and the reflected field. The incident field is the field that would be generated if the liquid were of infinite extent. The reflected field is the difference between the total wave field and the incident field. Hence, the acoustic pressure in the liquid, P_L , is given by :

$$P_L = P_L^i + P_L^r \quad (4.2)$$

The superscripts i and r refer to the incident and reflected waves respectively.

The transmitted wave field in the porous medium consists of a fast and slow compressional wave and a shear wave. In the porous solid the particle displacements of the fluid \underline{U} and the solid \underline{u} are the unknown quantities. The different wave fields are connected by the boundary conditions at the interface between the liquid and the porous sandstone block.

Waves in the liquid

The half-space $0 < z < \infty$ is filled with an ideal liquid. The pressure in the liquid P_L satisfies in the absence of volume forces the inhomogeneous wave equation :

$$\nabla^2 P_L - V_L^{-2} \partial_t^2 P_L + \rho_L \partial_t^2 \Phi_v = 0 \quad (4.3)$$

where Φ_v is the volume density of injected fluid volume.

Assuming that the point source is a monopole source, then

$$\Phi_v = \phi_v(t) \delta(x,y,z-h_T) \quad (4.4)$$

where $\phi_v(t)$ represents the volume injection function.

Splitting the total wave field in the liquid into the incident and reflected field, equation 4.3 can be decomposed into two differential equations:

$$\text{Incident: } \underline{V}^2 P_L^i - V_L^{-2} \partial_t^2 P_L^i = -\rho_L \partial_t^2 \Phi_v \quad (4.5)$$

$$\text{Reflected: } \underline{V}^2 P_L^r - V_L^{-2} \partial_t^2 P_L^r = 0 \quad (4.6)$$

To solve equation (4.5) use is made of the Fourier transforms with respect to time and space as defined in appendix B.

As a result we have :

$$\partial_z^2 \tilde{P}_L^i + \omega^2 \gamma_L^2 \tilde{P}_L^i = \rho_L \omega^2 \hat{\Phi}_v(\omega) \delta(z-h_T) \quad (4.7)$$

$$\text{with } \gamma_L = (V_L^{-2} - \alpha^2 - \beta^2)^{1/2} \quad ; \quad \text{Re,Im}(\gamma_L) \geq 0$$

The solution to this inhomogeneous differential equation is well known:

$$\tilde{P}_L^i = A^i e^{i\omega\gamma_L |z - h_t|} \quad (4.8)$$

$$\text{with } A^i = \frac{\omega \rho_L \hat{\Phi}_v(\omega)}{2i\gamma_L} \quad (4.9)$$

To solve the equation for the reflected wave, (4.6), again use is made of the Fourier transforms as defined in appendix B. This gives :

$$\partial_z^2 \tilde{P}_L^r + \omega^2 \gamma_L^2 \tilde{P}_L^r = 0 \quad z > 0 \quad (4.10)$$

A solution of this homogeneous differential equation is :

$$\tilde{P}_L^r = A^- e^{-i\omega\gamma_L z} + A^+ e^{i\omega\gamma_L z} \quad (4.11)$$

The first term represents a downgoing wave in the fluid, the second term an upgoing wave (pos. z-direction). Considering only the upgoing wave ($A^- = 0$), it can be expressed as the reflection coefficient at the interface (R_L) times the incident wave. This yields:

$$\tilde{P}_L^r = R_L A^i e^{i\omega\gamma_L (z + h_t)} \quad (4.12)$$

where R_L is the reflection-coefficient at the interface, and A^i is given by equation (4.9).

Waves in the porous rock

Biot's equations are used to describe the wave propagation in the porous sandstone block. In the rock, the particle displacement of the solid part, \underline{u} , and of the pore fluid, \underline{U} , are the fundamental unknown quantities.

The wave motion in the rock can be decomposed into a divergence-free part (shear wave) and a curl-free part (fast and slow compressional waves). The total displacements in the solid and fluid part of the rock are the sum of each of these contributions, so:

$$\text{solid part } \underline{u} = \underline{u}_+ + \underline{u}_- + \underline{u}_s \quad (4.13)$$

and

$$\text{fluid part } \underline{U} = \underline{U}_+ + \underline{U}_- + \underline{U}_s \quad (4.14)$$

The subscripts "+", "-" and "s" refer respectively to the fast and slow compressional waves and to the shear wave.

The expressions for the particle displacements in the rock are derived in appendix C.

IV.3.3 The pressure response in the fluid

In the laboratory experiments the acoustic pressure is measured by the receiver in the liquid above the rock sample. This pressure is equal to the superposition of the contributions of the incident and the reflected wave field :

$$P_L = P_L^i + P_L^r \quad (4.15)$$

In order to obtain a synthetic seismogram in the time domain, the received signal can be written as a convolution of the input signal with the system response:

$$P_L(t) = \partial_t [Q(t) * G_L(t)] \quad (4.16)$$

where $Q(t)$ is the source wavelet ($= \rho \partial_t \phi_v(t) \delta(x,y,z-h_t)$) and $G_L(t)$ is the system's Green's function. It is the response to a step in the rate of change of volume injection.

Equation 4.16 can also be written as:

$$P_L(t) = [Q(t) * G'_L(t)] \quad (4.17)$$

with $G'_L(t) = \partial_t G_L(t)$. $G'_L(t)$ now represents the response to an impulse in the rate of change of volume injection.

So to generate a synthetic wavetrain the expression for the system's response in eq. 4.16 or 4.17 has to be found. The calculation of this Green's function will be performed in the frequency domain and is transformed back to the space-time domain by a Fast Fourier program. A convolution with the emitted pulse then yields the desired acoustic trace.

In the following paragraphs expressions in the frequency domain are derived for the incident and the reflected field. The response function of the reflected field is calculated for two different models of the porous solid. The first model incorporates a reservoir rock that is described by the full frequency range of the Biot theory. It includes dispersion and attenuation of the waves due to viscous fluid flow in the pores of the solid. The second model uses the high frequency limit of the theory to describe the porous solid. The solid then becomes a loss-less medium. A solution of the Green's function in the time domain for this model is obtained by applying the Cagniard-de Hoop technique.

IV.3.4 Incident field

The transform-domain equivalent of equation (4.17) is for the incident field:

$$\tilde{P}_L^i = - \omega^2 \rho_L \hat{\phi}_v(\omega) \tilde{G}_L^i \quad (4.18)$$

The expression for the incident field in the transformed domain was given by eq. 4.8. Comparing this with (4.18) it follows that

$$\tilde{G}_L^i = - \frac{1}{2i\omega\gamma_L} e^{i\omega\gamma_L |z - h_t|} \quad (4.19)$$

Transforming this equation to the space-frequency domain, we have :

$$\hat{G}_L^i = \frac{\omega^2}{4\pi^2} \int_{-\infty}^{\infty} \int_{-\infty}^{\infty} -\frac{1}{2i\omega\gamma_L} e^{i\omega\gamma_L|z-h_t|} e^{i\omega(\alpha x + \beta y)} d\alpha d\beta \quad (4.20)$$

Introducing polar coordinates :

$$x = r \cos \theta, \quad y = r \sin \theta \quad r \geq 0, \quad 0 \leq \theta \leq 2\pi, \quad (4.21)$$

and new variables of integration κ and χ :

$$\alpha = \kappa \cos \chi, \quad \beta = \kappa \sin \chi \quad 0 \leq \chi \leq \pi, \quad 0 \leq \kappa \leq 2\pi, \quad (4.22)$$

we get :

$$\begin{aligned} d\alpha d\beta &= \kappa d\kappa d\chi \\ \alpha x + \beta y &= \kappa r \cos(\chi - \theta) \\ \alpha^2 + \beta^2 &= \kappa^2 \end{aligned} \quad (4.23)$$

Equation (4.20) changes into :

$$\hat{G}_L^i(r, \theta, z, \omega) = \frac{i\omega}{8\pi^2} \int_0^{\infty} \frac{1}{\gamma_L} e^{i\omega\gamma_L|z-h_t|} \kappa \int_0^{2\pi} e^{i\omega\kappa r \cos(\chi - \theta)} d\chi d\kappa \quad (4.24)$$

$$\text{where } \frac{1}{2\pi} \int_0^{2\pi} e^{i\omega\kappa r \cos(\chi - \theta)} d\chi = J_0(\kappa r), \quad (4.25)$$

a zero order Bessel function of the first kind.

Using the analytical solution of the Sommerfeld integral:

$$i\omega \int_0^{\infty} \frac{1}{\gamma_L} e^{i\omega\gamma_L|z-h_t|} J_0(\kappa r) \kappa d\kappa = \exp\left(\frac{i\omega R}{V_L}\right) / R \quad (4.26)$$

with $R = (r^2 + (z - h_t)^2)^{1/2}$,

we arrive for the incident field in the space-frequency domain as:

$$\hat{P}_L^i = \frac{-\omega^2}{4\pi R} \rho_L \hat{\phi}_V(\omega) \exp\left(\frac{i\omega R}{V_L}\right) \quad (4.27)$$

where $-\omega^2 \rho_L \hat{\phi}_V(\omega)$ is the source term.

Eq.4.27 is the monopole solution of the wave equations for an infinite homogeneous medium. It represents the direct wave between transmitter and receiver, which has an amplitude of $1/8\pi^2 R$ and is time shifted from the origin by an amount of R/V_L .

IV.3.5 Reflected field: full frequency range

The full frequency range of the Biot theory is given in appendix A. To obtain the system's response of the reflected field, we write analogue to the incident field:

$$\tilde{P}_L^R = -\omega^2 \rho_L \hat{\phi}_V(\omega) \tilde{G}_L^R \quad (4.28)$$

Comparing this with the expression for the reflected field in the transformed domain (eq. 4.12) we arrive, after changing the variables of integration (eq. 4.23), at the expression for the Green's function in the frequency domain:

$$\hat{G}_L^R(r, \theta, z, \omega) = \frac{i\omega}{4\pi} \int_0^\infty \frac{R_L}{\gamma_L} e^{i\omega\gamma_L(z+h_t)} J_0(\kappa r \omega) \kappa d\kappa \quad (4.29)$$

The reflection coefficient R_L is calculated in appendix C, using Biot's theory to describe the wave propagation in the rock, plus continuity of stress and displacement at the boundary. The vertical propagation coefficients of the bulk waves then are given by:

$$\begin{aligned} \gamma_+ &= (V_+^{-2} - \kappa^2)^{1/2}, & \gamma_- &= (V_-^{-2} - \kappa^2)^{1/2}, & \gamma_S &= (V_S^{-2} - \kappa^2)^{1/2}, \\ \gamma_L &= (V_L^{-2} - \kappa^2)^{1/2} \end{aligned} \quad (4.30)$$

The expression for the velocity in the rock of the compressional waves is given by eq. A.22 and of the shear wave by eq. A.25 of appendix A. The speed of the ideal liquid above the porous solid is equal to:

$$V_L = (K_L/\rho_L)^{1/2} \quad (4.31)$$

In equation 4.29 only one integration variable remains.

The velocities calculated with the Biot theory are complex-valued. Therefore in solving equation 4.29 a square root singularity occurs only at $\kappa^2 = V_L^{-2}$. This singularity can be removed by splitting up the integral into two parts. In both parts of the integral the singularity is then removed by a suitable substitution for κ .

So we get:

$$\hat{G}_L^r = I + II$$

where

$$I = \frac{i\omega}{4\pi} \int_0^{V_L^{-1}} \frac{R_L}{\gamma_L} e^{i\omega\gamma_L(z+h_t)} J_0(\kappa r\omega) \kappa d\kappa \quad (4.32)$$

$$\text{Substitution of } \kappa = \frac{\sin \psi}{V_L} \quad 0 \leq \psi \leq \pi/2$$

changes integral I into :

$$I = \frac{i\omega}{4\pi} \int_0^{\pi/2} \frac{R_L}{\gamma_L} e^{i\omega\gamma_L(z+h_t)} J_0\left(\frac{\sin \psi}{V_L} r\omega\right) \frac{\sin \psi}{V_L} \frac{\cos \psi}{V_L} d\psi \quad (4.33)$$

with the propagation coefficients :

$$\begin{aligned} \gamma_+ &= \left\{ V_+^{-2} - \frac{\sin^2 \psi}{V_L^2} \right\}^{1/2}, \quad \gamma_- = \left\{ V_-^{-2} - \frac{\sin^2 \psi}{V_L^2} \right\}^{1/2}, \quad \gamma_s = \left\{ V_s^{-2} - \frac{\sin^2 \psi}{V_L^2} \right\}^{1/2} \\ \gamma_L &= V_L^{-1} \cos \psi \end{aligned} \quad (4.34)$$

$$II = \frac{i\omega}{4\pi} \int_{V_L^{-1}}^{\infty} \frac{R_L}{\gamma_L} e^{i\omega\gamma_L(z+h_t)} J_0(\kappa r\omega) \kappa d\kappa \quad (4.35)$$

$$\text{Substitution : } \kappa = \frac{\cosh \xi}{V_L} \quad ; \quad \xi \geq 0$$

gives :

$$II = \frac{i\omega}{4\pi} \int_0^{\infty} \frac{R_L}{\gamma_L} e^{i\omega\gamma_L(z+h_t)} J_0\left(\frac{\cosh \xi}{V_L} r\omega\right) \frac{\cosh \xi}{V_L} \frac{\sinh \xi}{V_L} d\xi \quad (4.36)$$

with the propagation coefficients :

$$\begin{aligned} \gamma_+ &= \left(V_+^{-2} - \frac{\cosh^2 \xi}{V_L^2} \right)^{1/2}, \quad \gamma_- = \left(V_-^{-2} - \frac{\cosh^2 \xi}{V_L^2} \right)^{1/2} \\ \gamma_s &= \left(V_s^{-2} - \frac{\cosh^2 \xi}{V_L^2} \right)^{1/2}, \quad \gamma_L = \frac{i \sinh \xi}{V_L} \end{aligned} \quad (4.37)$$

The expression for the Green's function in the frequency domain now becomes :

$$\hat{G}_L^R(r,z,\omega) = I + II \quad (4.38)$$

where the integrals I and II are given by resp. eqs. 4.33 and 4.36, and the corresponding propagation coefficients by respectively eqs. 4.34 and 4.37.

IV.3.6 Numerical considerations

The Green's function calculated with eq. 4.38 is transformed back to the space-time domain with the help of a fast Fourier transform program, according to equation B4. A question of practical importance relates to the minimum number of points in the frequency domain where the integral has to be evaluated and the accuracy to which extent eq. 4.38 has to be solved.

Sampling in ω -domain

As far as the sampling in the ω -domain is concerned the problem is relatively simple. The waveform received at the transducer is real. This condition is assured by taking $\hat{G}'(-\omega) = \hat{G}'^*(\omega)$ where the asterisk designates the complex conjugate, so only positive values of omega have to be considered. The frequency bandwidth for which the function has to be evaluated is given by the characteristics of the transducers and by the frequency bandwidth of the emitted pulse.

To avoid aliasing the sampling rate must conform to the sampling theorem, i.e. $\Delta t \leq 1/2f_{Nyq}$, where the Nyquist frequency is the highest frequency present in the signal.

In every step of the frequency sampling the integrals (4.33) and (4.36) must be solved. Integral I is extended over the fixed interval $0 \leq \psi \leq \pi/2$, while integral II includes the evanescent part of the wavefield. The latter rapidly approaches zero due to the high frequencies at which is being modelled. (centre frequency $\approx 5\text{MHz}$).

Moreover the integration is complicated by the oscillatory behaviour of the Bessel function included in both integrals. Fig 4.5 shows the real and imaginary parts of integrals I and II. The frequency is 50 kHz, the formation parameters as listed in Table 4.1.

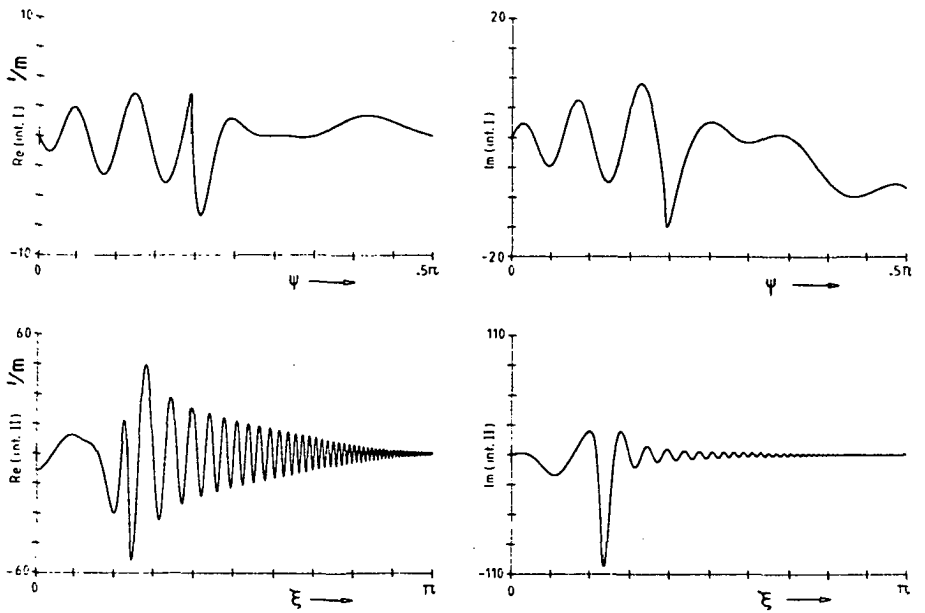


Fig 4.5 Real and imaginary part of $\hat{G}_L^R(r, \theta, z, \omega) = int.I + int.II$
 frequency = 50 kHz., $z_t = z_r = .001$ m., $tr_s = .13$ m.

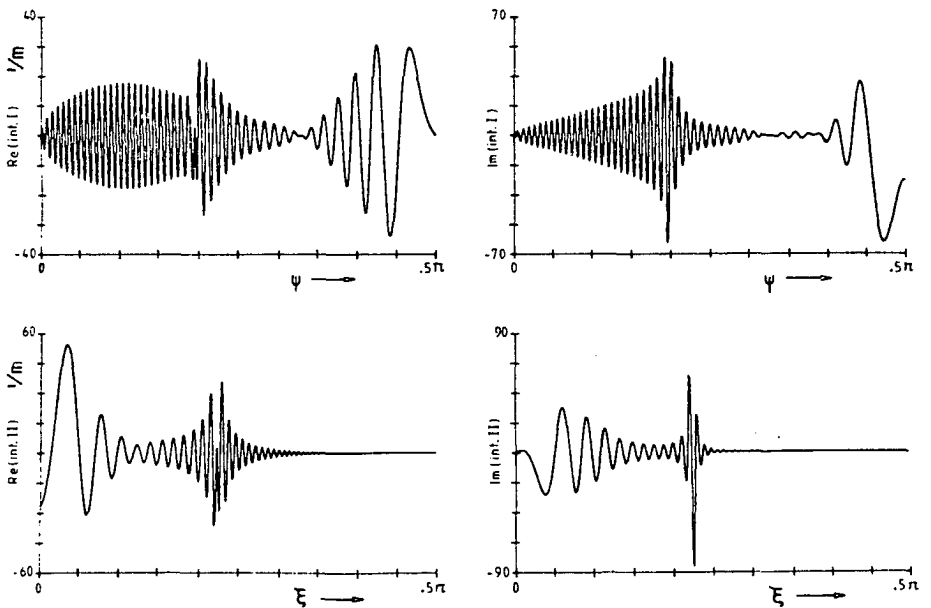


Fig 4.6 Real and imaginary part of $\hat{G}_L^F(r, \theta, z, \omega) = int.I + int.II$
 frequency = 500 kHz., $z_t = z_r = .001$ m., $tr_s = .13$ m.

The integrals are solved numerically by means of the trapezoidal rule. To acquire the desired accuracy a sufficient number of samples have to be taken in between the zero-crossings of the integrated functions. However this number of zero-crossings varies with frequency. Fig 4.6 shows the same response function as before, but now at a frequency $f = 500 \text{ kHz}$.

Sampling in the κ -domain

The arrivals of the different waves are distinguished in the ω - κ domain by sharp discontinuities. To reach the desired accuracy the sampling rate in the κ -domain has to be intensified at those arrivals. To this end the trapezoidal rule in combination with the Romberg interpolation method is used to evaluate numerically the integrals.

The interval to be integrated is divided into several subdivisions. Each subdivision is evaluated by the trapezoidal rule and by two successive Romberg interpolations. If the difference between the two interpolations is bigger than a specified value, then the subdivision is again divided into smaller segments in which the evaluation takes place. The procedure is repeated until the desired accuracy is reached. The numerical method automatically takes into account the variation of the oscillatory behaviour of the functions with frequency. It also accurately evaluates the discontinuities in the functions by reducing the numerical step distance and thus increasing the sampling rate in those regions.

Reflection coefficient

The reflection-coefficient appearing in the expressions is solved from appendix C by way of Cramer's rule; i.e. :

$$R_L = \Delta_5 / \Delta \quad (4.39)$$

where Δ = determinant of the matrix formed by the coefficients of equations C.17 - C.21.

and Δ_5 = determinant of the same matrix, where the fifth column of the matrix is replaced by the vector occurring at the right hand side of eq. C.17 - C.21

The variable of integration χ still present in the equations drops out of the solution for R_L .

Calculated example

An example of the calculated Green's function in the space-time domain is given in fig 4.7. The parameters of Table 4.1 were used as input. The direct wave through the fluid is not included, i.e. the incident field is neglected. The Green's function was calculated for a frequency range of 0 - 1 MHz. The number of samples was 409, with an increment in frequency of $\Delta f = 2441$ Hz.

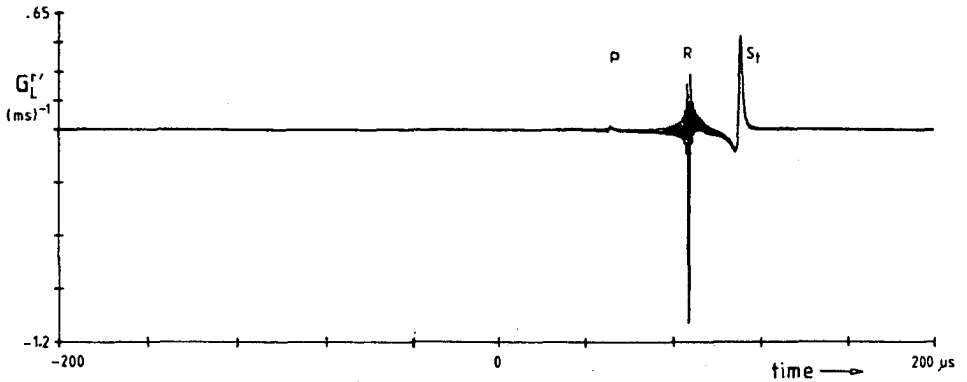


Fig 4.7 Impulse response in the time domain. $k = 10$ Darcy

The arrivals of successively the compressional, the body wave in the liquid reflected on the interface and the pseudo-Stoneley or Scholte wave can be distinguished clearly in fig 4.7. The latter is a surface wave propagating along a fluid/solid interface.

Due to the high frequencies and the oscillatory behaviour of the integrals to be solved, the calculation of a Green's function requires very much computation time. For the impulse response shown here it amounts to approximately 800 minutes on a Gould 32/77 computer.

IV.3.7 Reflected field: high frequency limit

The second model which was developed to simulate the experiments incorporates the high frequency limit of the Biot theory.

The energy dissipation of the bulk waves in Biot's theory is described by the factor $ibF(\kappa)/\omega\phi\rho_f$. In the high frequency limit of the theory ($\omega \rightarrow \infty$) this factor approaches zero. The solid becomes loss-less and the velocities of the bulk waves are real-valued and no longer dependent on

the frequency. It is therefore possible to solve the wave equations by the Cagniard-de Hoop technique in this high frequency limit of the Biot theory. The model was developed by de Vries (1985). The solution of the Cagniard-de Hoop technique is exact. It thus allows to check the results of the Fourier-Bessel approach. For the sake of completeness, a brief description of the method is given here. For more details the reader is referred to the original work of de Vries (1985).

In order to be able to use the Cagniard-de Hoop technique the transform to the frequency domain is given by a one-sided Laplace transform:

$$\hat{p}(x,y,z,s) = \int_0^{\infty} e^{-st} p(x,y,z,t) dt \quad (4.40)$$

with real and positive parameter s .

The Fourier transform with respect to space is given by eq. B2 and substituting $\alpha = i\alpha$ and $\beta = i\beta$.

The resulting expression for the system's Green's function now becomes (de Vries 1985):

$$\hat{G}_L^r = \frac{s^2}{4\pi^2} \int_{-\infty}^{\infty} d\beta \int_{-\infty}^{\infty} \frac{R_L}{2s \gamma_L} e^{-s(i\alpha x + i\beta y + \gamma_L(z+h_t))} d\alpha \quad (4.41)$$

The Green's function G_L^r is the response to a step in the rate of change of volume injection.

The Cagniard-de Hoop technique (de Hoop 1960) transforms the integration with respect to α and β into the real integration:

$$\hat{G}_L^r = \int_{T_{arr}}^{\infty} e^{-st} g(x,y,z,\tau) d\tau \quad (4.42)$$

by changing the path of integration in the complex p -plane such that the term in the exponent is purely real and positive. Lerch's uniqueness theorem then ensures that:

$$\begin{aligned} G_L^r(x,y,z,\tau) &= 0 & -\infty < \tau < T_{arr} \\ &= g(x,y,z,\tau) & T_{arr} < \tau < \infty \end{aligned} \quad (4.43)$$

Applying the Cagniard-de Hoop technique by substituting:

$$\alpha = \kappa \cos \theta - q \sin \theta, \quad \beta = \kappa \sin \theta + q \cos \theta$$

$$p = i\kappa$$

$$\operatorname{Re}\{pr + \gamma_L(z + h_t)\} = \tau$$

$$(4.44)$$

$$\operatorname{Im}\{pr + \gamma_L(z + h_t)\} = 0$$

The following expression for the space-time Green's function results:

$$\begin{aligned} &= 0 && -\infty < \tau < T_{HW} \\ &= \int_0^{Q_{BW}(\tau)} \frac{\operatorname{Im}\{R_L(p^{HW}, q)\}}{2\pi^2 \{T_{BW}^2(q) - \tau^2\}^{1/2}} dq && T_{HW} < \tau < T_{BW} \\ G_L^r &= \int_{Q_{HW}(\tau)}^{Q_{BW}(\tau)} \frac{\operatorname{Im}\{R_L(p^{HW}, q)\}}{2\pi^2 \{T_{BW}^2(q) - \tau^2\}^{1/2}} dq \\ &+ \int_0^{Q_{BW}(\tau)} \frac{\operatorname{Re}\{R_L(p^{BW}, q)\}}{2\pi^2 \{\tau^2 - T_{BW}^2(q)\}^{1/2}} dq && T_{BW} < \tau < T_{HWend} \quad (4.45) \\ &= \int_0^{Q_{BW}(\tau)} \frac{\operatorname{Re}\{R_L(p^{BW}, q)\}}{2\pi^2 \{\tau^2 - T_{BW}^2(q)\}^{1/2}} dq && T_{HWend} < \tau < \infty \end{aligned}$$

The limits of integration are:

$$Q_{BW}(\tau) = \left\{ \frac{\tau^2}{(d^2 + (h_r + h_t)^2)^{1/2}} - \frac{1}{V_+} \right\}^{1/2} \quad (4.46)$$

$$Q_{BW}(\tau) = \left\{ \left(\frac{\tau}{d} - \frac{h_t + h_r}{d} \frac{1}{V_L} - \frac{1}{V_+} \right)^2 - \frac{1}{V_+^2} \right\}^{1/2} \quad (4.47)$$

$$\text{and } T_{BW}(q) = \{d^2 + (h_t + h_r)^2\}^{1/2} \left\{ \frac{1}{V_L^2} + q^2 \right\}^{1/2} \quad (4.48)$$

T_{HW} and T_{BW} are the arrival times of the head wave and the body wave in the fluid. T_{HWend} is the time beyond which there are no head wave contributions any more. To obtain the expressions for the shear head wave, V_+ has to be replaced by V_s in the equations.

The square root singularities occurring at the end points of the q -integration are removed by the transformation:

$$q_n^2 = Q_{n-1}^2 \cos^2 \psi + Q_n^2 \sin^2 \psi \quad (4.49)$$

where Q_n is an endpoint of the integration.

An example of the system's step response is given in fig 4.8. The arrivals of the various waves at the receiver are distinguished by discontinuities in the curve.

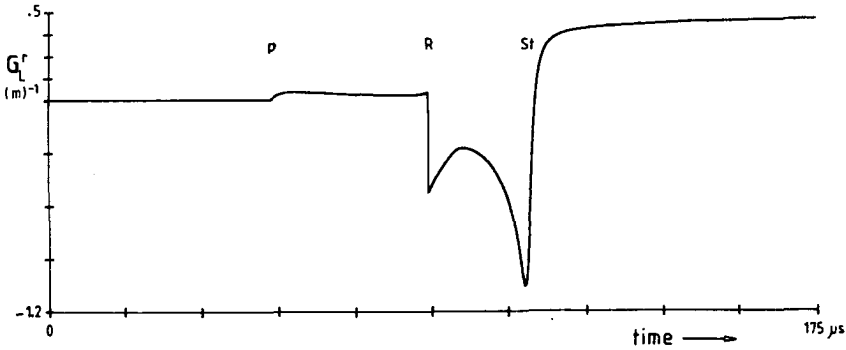


Fig 4.8 Step response in the time domain. High frequency limit.

In computing the step response with the Cagniard-de Hoop technique a single bounded integral has to be solved. In contrast to the previous high frequency range model the expressions do not show any oscillatory behaviour. The numerical evaluation therefore requires much less computer time. The time needed to calculate a single trace amounts to approximately 10 minutes on a Gould 32/77 computer.

IV.3.8 The convolutions

In the laboratory measurements the acoustic pressure in the fluid is recorded by the receiver. In order to model the experiments the system's Green's function has to be convolved with a certain source pressure pulse. The pulse emitted by the transmitter in the experiments is taken as the source signature. A convolution with the Green's function then models what really will be measured. The source signature is shown in fig 4.9. The source wavelet was determined by recording the direct wave from transmitter to receiver through the fluid. It was recorded in milli- Volts.

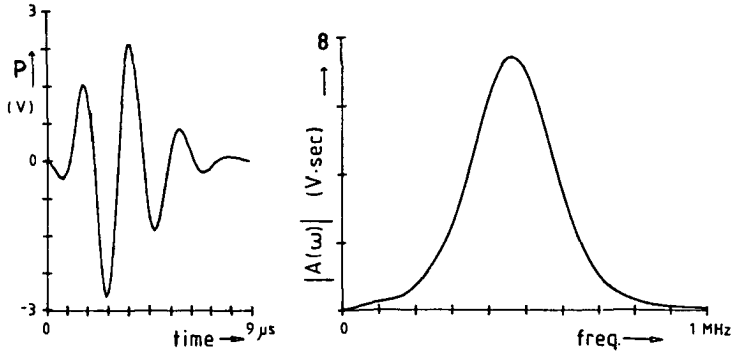


Fig 4.9 Input signal. a. time b. amplitude spectrum.

The direct wave is described in terms of ϕ_v by the expression for the incident field in the frequency domain:

$$\hat{P}_L^i = \frac{-\omega^2}{4\pi R} \rho_L \hat{\phi}_v(\omega) \exp\left(\frac{i\omega R}{V_L}\right) \quad (4.50)$$

For the reflected pressure in the liquid can be written (see 4.28):

$$\hat{P}_L^r = -\omega^2 \rho_L \hat{\phi}_v(\omega) \hat{G}_L^r \quad (4.51)$$

The expression in front of the Green's function in eq 4.51 can now be written as:

$$-\omega^2 \rho_L \hat{\phi}_v(\omega) = 4\pi R \hat{P}_L^i \exp\left(\frac{-i\omega R}{V_L}\right) \quad (4.52)$$

So a multiplication in the frequency domain of the measured input signal with the Green's function yields, apart from a factor $4\pi R$, the desired microseismogram.

The model using the high frequency limit of the Biot theory calculates the step response function of the system. The reflected pressure in the liquid then is equal to:

$$\hat{P}_L^r = s^3 \rho_L \hat{\phi}_v(\omega) \hat{G}_L^r \quad (4.53)$$

The term $s^3 \rho_L \hat{\phi}_v$ in eq 4.53 is now, in terms of the incident field:

$$s^3 \rho_L \hat{\phi}_V = 4\pi R s \hat{P}_L^i \exp\left(\frac{sR}{V_L}\right) \quad (4.54)$$

The input pulse of fig 4.9 has to be convolved with the time-derivative of the step response of the model using the Cagniard-de Hoop technique to compare the result with the result of the Fourier-Bessel approach. Figs 4.10 and 4.11 show the input signal convolved with the system response function of fig 4.7 and with the time-derivative of the system response function of fig 4.8, respectively. The agreement between the results of the two different models is very good. It implies that the Fourier-Bessel approach is working properly. The amplitude of the P-wave calculated by the full frequency model (fig 4.10) is slightly smaller than when calculated with the loss-less solid model (fig 4.11). This is to be expected as the attenuation of the P-wave is low ($Q \approx 1500$, refer fig 4.1). The difference between the models becomes apparent in the amplitude of the Stoneley wave.

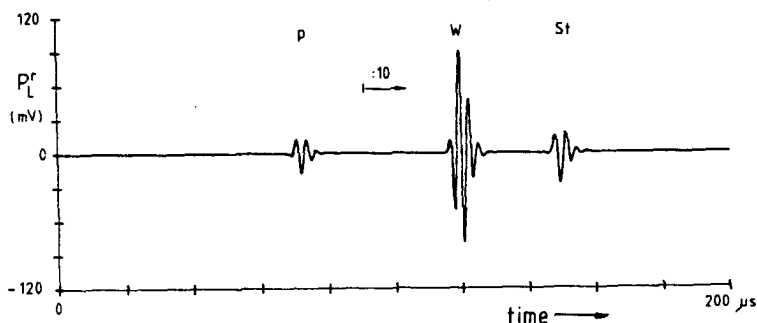


Fig 4.10 Convolution of the input signal with the system response as given in fig 4.7. $k = 10$ Darcy

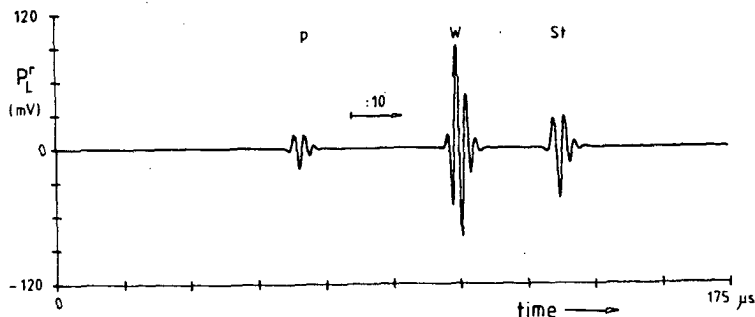


Fig 4.11 Convolution of the input signal with the time derivative of the system response as given in fig 4.8.

IV.3.9 Numerical results

In this paragraph pressure-time histories computed for various liquid/porous solid systems in the higher frequency ranges are presented. The low-frequency range (0-40 kHz) has been treated extensively by Rosenbaum (1974). The aim of the modelling is to investigate theoretically the effect of rock parameters upon the recorded wavetrain according to Biot's theory and to find the optimum configuration that allows the desired effects to be recorded with maximum detail.

A total of fifteen parameters enter the model for the liquid/porous solid configuration. Although these parameters all have physical significance, it is impossible to cover them all. The presented models are therefore limited to the various reservoir samples that are used in the experiments. Also some geometric configurations are shown that theoretically enhance the observed acoustic effects.

Depending upon the boundary conditions at the interface between the porous block and the liquid, several surface waves may show up in the computed traces, such as a pseudo Rayleigh wave propagating along a vacuum/solid interface, and pseudo Stoneley or Scholte waves, propagating along a liquid/solid boundary. If the pores of the rock are sealed at the interface, a surface wave occurs which is slower than the slowest wave in the rock, i.e. the slow compressional. Feng and Johnson (1983) gave a thorough treatment of these surface waves and their mode of occurrence.

The full frequency range model is compared to the model that uses the loss-less solid description of the Biot theory. The input data for the presented plots are given in Table 4.1. Any changes from this set of parameters is given with the figures. As the direct wave between transmitter and receiver through the fluid can be shielded off in the actual experiments, it has not been included in the models either.

Standard configuration

Figure 4.12 shows the pressure-time history computed for the loss-less solid. The input parameters of the model are given in Table 4.1. The velocities of the bulk waves in the solid and fluid are:

$$V_p = 2608.8, \quad V_s = 1386, \quad V_{ps1} = 706.8 \text{ and } V_L = 1500 \text{ m/s.}$$

The acoustic pressure is expressed in mVolts because the sensitivity of the recording system in Volts/Pa is unknown. The calculated pressure

associated with the fast compressional arrival is much smaller than the reflected wave in the water. To enhance the details in the trace the amplitudes have been reduced by a factor 10 just after the compressional arrival.

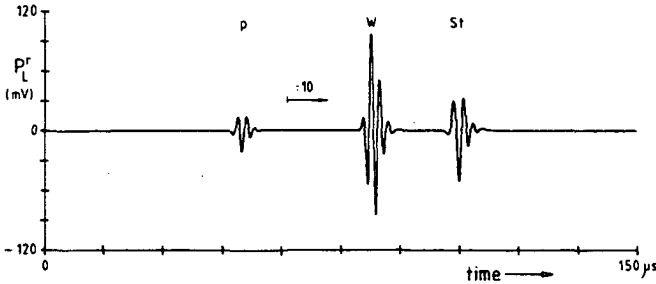


Fig 4.12 High frequency limit
 $z_t = z_r = 1 \text{ mm}$, $\epsilon = 3$, $\text{trs} = 12 \text{ cm}$.

In the computed waveform the arrivals of, successively, the compressional (P), the reflected body wave (W) and the pseudo-Stoneley wave (St) clearly show up. The shear wave is not present. Its velocity is less than that of the water above the block and therefore its critical angle is imaginary valued; it does not refract into the fluid.

Distance above interface

The amplitude of the surface waves decays away from the interface. This effect is shown in fig 4.13. It shows a trace calculated for a configuration where the receiver has been placed 5 mm above the porous block. The pseudo-Stoneley wave can scarcely be distinguished anymore, whereas the amplitudes of the P-wave and the reflection on the interface hardly change.

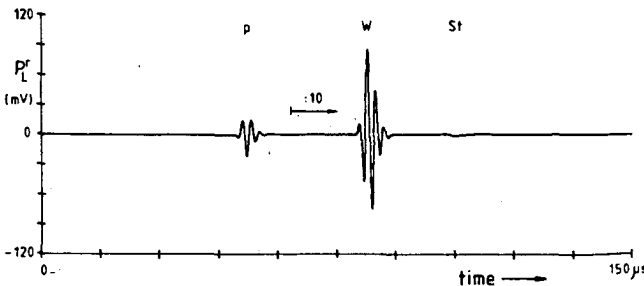


Fig 4.13 High frequency limit
 $z_t = 1 \text{ mm}$, $z_r = 5 \text{ mm}$, $\epsilon = 3$, $\text{trs} = 12 \text{ cm}$.

Interface conditions

The surface waves are sensitive to the way the interface has been prepared. In actual logging practice, the interface of a porous formation is always covered by a thin, almost impermeable mudcake. It is not clear how the mudcake behaves acoustically in reality, but as a first approximation we can investigate the limiting case of completely sealed off pores at the interface. (This condition can be achieved in the actual experiments by covering the rock sample with a thin impermeable foil). This particular case in the high frequency limit is shown in fig 4.14. The amplitude of the reflected wave in the fluid has been reduced by a factor 10 in this plot.

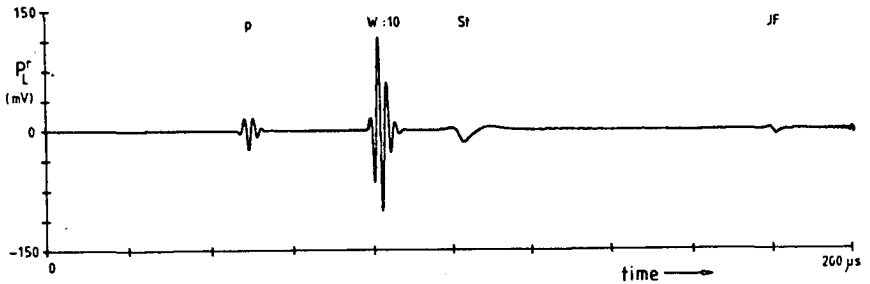


Fig 4.14 High frequency limit
 $z_t = z_r = 1 \text{ mm}$, $\epsilon = 3$, $\text{trs} = 12 \text{ cm}$, $T = \infty$

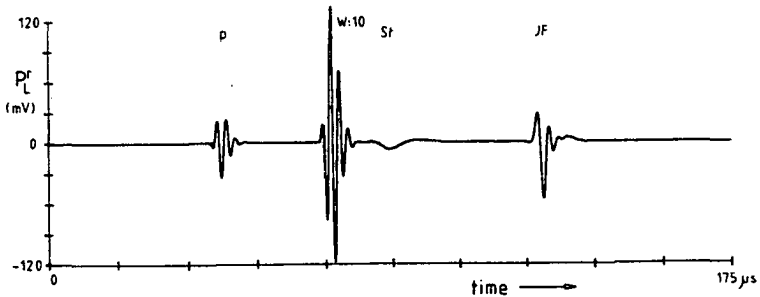


Fig 4.15 High frequency limit
 $\epsilon = 1.79$, $\text{trs} = 10 \text{ cm}$, $T = \infty$

Compared to fig 4.12 (completely open pores) the amplitude of the pseudo Stoneley wave (St) is reduced considerably. It also shows a low frequency content. Furthermore a surface wave (Jf) shows up whose velocity is less than the slowest wave speed in the porous block. ($V_{\text{surf}} = 557 \text{ m/s}$). We may call this a "Johnson-Feng" surface wave as they were the first to describe this wave theoretically. Changing the properties of the porous solid so that the slow P-wave becomes faster

($\epsilon = 1.79$, $V_{ps1} = 933$ m/s), fig 4.15, the "Johnson-Feng" surface wave becomes stronger and faster ($V_{JF} = 785$ m/s).

Sample under silicon oil

In the actual experiments, the shear wave in our sandstone samples will be slower than the wave speed in water. This implies that the shear wave can not be detected in a refraction measurement with the sample submerged in water. However, if the rock is submerged in a fluid whose wave velocity is less than the shear velocity in the rock, the shear wave shows up in the recorded trace. This is modelled in fig 4.16. The sample is submerged in silicon oil which has a bulk wave speed of 980 m/s. The shear velocity in the solid is 1386 m/s and the wave (S) shows up clearly in the computed time trace. The amplitude of the reflected wave in the oil (O) has been reduced by a factor 50. The pseudo Stoneley wave is indiscernible from the reflected body wave in the oil.

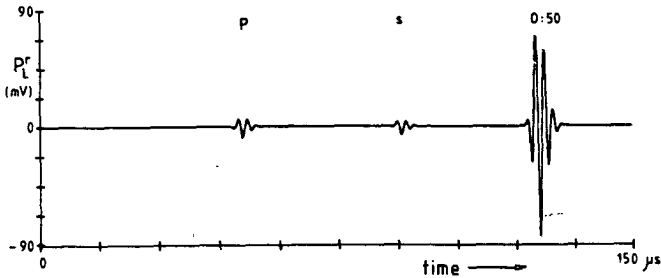


Fig 4.16 High frequency limit
 $z_t = z_r = 1$ mm, $\epsilon = 3$, $tr_s = 12$ cm, rock under silicon oil.

Full frequency range

So far the given pressure-time traces were computed in the high frequency limit of the Biot theory. The corresponding synthetic microseismograms covering the full frequency range of the Biot theory, including attenuation and dispersion of the bulk waves, are given in figs 4.17 to 4.19.

Fig 4.17 shows the calculated trace with completely sealed-off pores. Compared to the loss-less case (fig 4.14), the pseudo-Stoneley wave arrival has become even weaker. The Johnson-Feng surface wave does not show up in the trace.

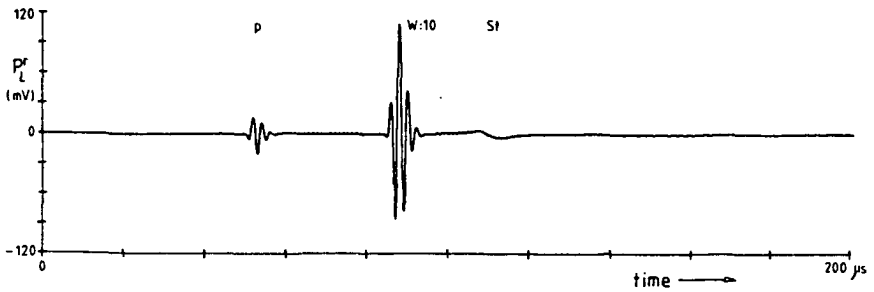


Fig 4.17 Full frequency range
 $T = \infty$

Fig 4.18 shows the calculated acoustic trace for a configuration with the porous rock placed under silicon oil. As in the loss-less case the compressional and shear wave arrivals can be distinguished clearly. The reflected body wave in the oil shows less interference with the pseudo-Stoneley wave.

Permeability

Fig 4.19 shows a calculated acoustic trace for a configuration with the rock submerged in water. The permeability of the porous rock is taken to be 1 Darcy. The effect of a change in permeability can be shown by

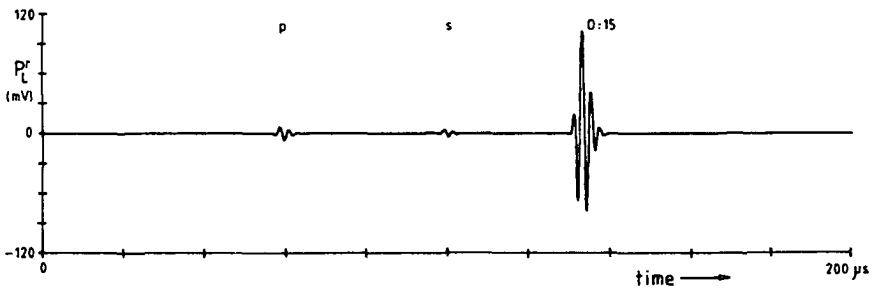


Fig 4.18 Full frequency range
 Rock sample under silicon oil.

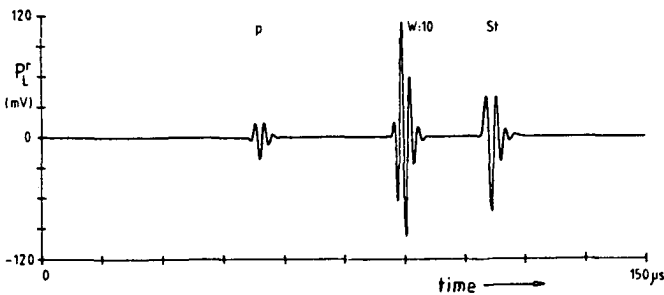


Fig 4.19 Full frequency range
 $k = 1$ Darcy.

comparing fig 4.19 with fig 4.10, the latter of which includes a porous solid with $k = 10$ Darcy.

The permeability appears to have a large effect upon the calculated amplitude with which the pseudo-Stoneley wave is generated. In the Biot equations, the permeability appears in that part which describes the attenuation of the bulk waves. The effect of permeability is therefore not present in the model using the loss-less solid limit of the Biot theory.

To quantify the effect of permeability, several microseismograms have been calculated where in each trace a different value of permeability has been assigned to the porous block.

The peak-to-peak amplitudes of the arrivals of the compressional and the pseudo-Stoneley waves have been plotted versus the permeability of the porous solid in fig 4.20.

The amplitudes have been normalized to the peak-to-peak amplitudes of the arrivals in the loss-less solid case (fig 4.11). It appears that

the amplitude of the compressional wave is hardly affected but that the amplitude with which the pseudo-Stoneley wave is generated, is highly sensitive to the permeability of the porous rock. To model the effect of permeability correctly, the theoretical model including the full frequency range of the Biot theory should be used.

Comparison of the models

Provided the wave propagation in the porous solid obeys Biot's theory the model incorporating the high frequency limit can be used very well to predict the recorded waveforms in laboratory refraction measurements. The model needs little computer time to calculate a synthetic seismogram and it predicts the correct arrival times of the various waves at the receiver as compared to the full theory. It can therefore be of valuable assistance when interpreting an experimentally acquired wavetrain.

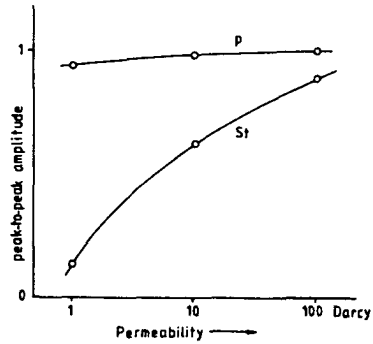


Fig 4.20
Peak-to-peak amplitudes of the arrivals versus permeability. The amplitudes are normalized to the loss-less case (fig 4.11).

However, the high frequency limit model does not include the effect of permeability of the rock upon the waveforms, which is an important parameter of oil and gas producing reservoirs. The model incorporating the full frequency range of the Biot theory including attenuation and dispersion of the bulk waves, has to be used to predict the effect of a change in this parameter. In doing so, the amplitude of the pseudo-Stoneley wave appears to be highly sensitive to the permeability of the porous rock along whose interface it propagates. This may provide a means to obtain the permeability from the recorded wavetrains.

The amplitudes of the surface waves decay away from the interface. The receiver therefore has to be placed close to the interface to obtain maximum detail in the recorded surface wave amplitudes.

In the acoustic traces calculated with the loss-less solid with completely sealed off pores, a "Johnson-Feng"-surface wave shows up which yields information about the slow compressional wave propagating inside the porous block. Using the full frequency range, this wave does not show up. It is unlikely that this surface wave, if existing, is detectable under the conditions prevailing at our experiments. But this surface permeability of the interface still needs more experimental investigation.

It is not possible to measure the shear wave in our measurement set-up with the reservoir sample submerged in water due to the properties of our samples. Modelling indicates that the shear wave will show up distinctly on the traces if a liquid above the sample is chosen that has a very low wave speed; for instance silicon oil with a velocity of 980 m/s.

V. ACOUSTIC MEASUREMENTS

V.1 Introduction

This chapter of the thesis discusses the experimental set-up for the acoustic measurements and gives some preliminary results. First, a description of the data-acquisition system is given. This system was developed in cooperation with the Technisch Physische Dienst. It is a general set-up for acoustic experiments and can be used to perform transmission as well as refraction measurements. Both measurement techniques were used during the course of the project. The transmission measurements provide a means of determining the properties of the bulk waves in the rock on small, relatively easy to produce, rock samples. It is possible to measure not only the compressional and shear waves, but also the slow compressional wave predicted by the Biot theory. The refraction experiments on the other hand, more closely resemble the measurements made by acoustic tools in actual well logging.

A range of artificial rock samples has been constructed on which acoustic measurements are currently performed. The manufactured rock samples differ in grain size and cement content. The objective is to link the acoustic responses of the samples to their rock properties, such as porosity, lithology, rock strength and permeability. The experiments are still being carried out and the interpretation of the results is still in its initial phase.

The synthetic rock samples appear to be suitable for acoustic research. The slow P-wave, as predicted by the Biot theory, can clearly be distinguished. The porosity versus velocity relationships valid for the artificial rock samples, show similar characteristics as the correlations encountered in natural reservoir rock. The shear-to-compressional transit time ratio appears to be specific for the synthetic rock samples. This agrees well with the observations made in the field examples in chapter II.

V.2 Data acquisition system

The data acquisition system was developed in cooperation with the Technisch Physische Dienst (TPD) in Delft. A schematic representation of the system is given in fig. 5.1. The heart of the system is a high frequency oscilloscope annex A/D-converter. Pre-programmed acoustic pulses are supplied by a programmable waveform generator. The signals are transmitted and received by a single pair of transducers of which the receiver is attached to an X-Y-Z positioning system. The total acquisition system is controlled by an IBM XT computer. The required software for this set-up was specifically developed. A short description of the various components of the system is given below. The transducer characteristics are described in appendix D.

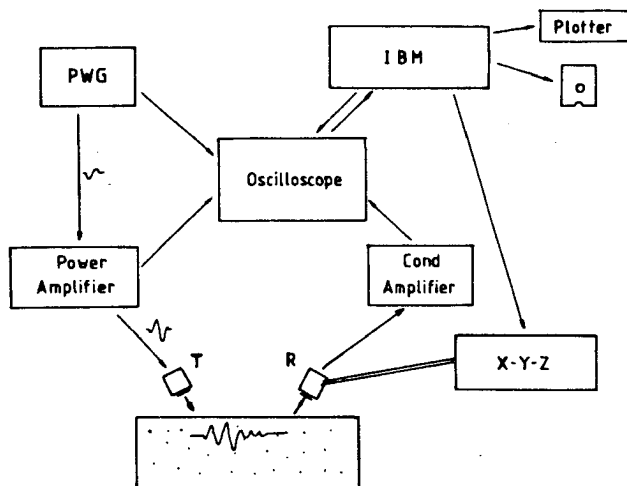


Fig 5.1 Data-acquisition system

A programmable waveform generator (PWG) is employed to generate the acoustic signals. The PWG was purchased from the TPD. It converts a pre-programmed 12-bit digital pulse shape into an analogue signal. The digital signals are stored on floppy disc. This ensures an exactly reproducible acoustic input pulse into the measurement system. The PWG can process any analytical pulse shape. The apparatus also incorporates an internal clock to synchronize the total acquisition system.

The analogue signal from the PWG is amplified 50 dB by an ENI 2100L power amplifier before it is passed to the transmitter. This is necessary to obtain enough power in the signal for the transmitting transducer to generate an acoustic pulse.

The data acquisition system contains a single set of transducers. Two sets are available for the measurements. One set has a centre frequency of around 0.5 MHz, the other of around 0.25 MHz. The transducers are described in more detail in appendix D.

After the receiving transducer, a Brüel & Kjaer wideband conditioning amplifier type 2638 is included in the acquisition circuit. The amplifier contains various high and low cut filters and applies an amplification to the signal that can be regulated from 0 - 60 dB in steps of 1 dB.

The heart of the acquisition system is a LeCroy 9400 digital oscilloscope. It is a two-channel, 8-bit A/D-converter with a maximum single shot sampling rate of 100 Megasamples per second. The scope contains two 32000 data point acquisition memories. It also contains a software package for elaborate signal processing on the digitally stored waveform. The processing options include a signal averaging technique which is used during the measurements to reduce the noise level in the recorded waveforms. This method of attenuating noise relative to the signal is based on the fact that a repetitive signal added to itself n times, increases in amplitude by a factor n , while incoherent noise only increases by a factor \sqrt{n} . Thus after n sweeps, the signal-to-noise ratio is improved by a factor \sqrt{n} . Of course, the averaging method requires the signals to be exactly repetitive, which condition is ensured by the use of the PWG. The digitally stored pulse shape and the internal clock of this apparatus make sure that each repeated signal is exactly the same in amplitude as well as phase. In our experiments, using a sweep-interval of .01 sec, it appeared that after approximately 1000 sweeps any white noise was effectively suppressed. Fig 5.2 illustrates the noise reduction by averaging the signal. It shows a trace recorded as a single shot (fig 5.2a) and the same signal after 1000 times averaging (fig 5.2b).

The pair of transducers is mounted on a stiff frame. The position of the transmitter is fixed. The receiver is connected to the z-axis of an

x-y-z positioning system which is attached to the frame. The positioning system consists of three perpendicular axes. Each axis contains a spindle which is connected to a stepping motor, thus allowing the displacement of the receiver in three perpendicular directions. At any time, the actual position of the receiver is registered by the acquisition software.

The accuracy of the positioning system is high (0.05 mm / 300 mm displacement) and the system has a smallest step distance in each direction of 0.025 mm.

These accuracy figures refer to the relative displacements between two locations of the receiver. The transmitter, on the other hand, is not attached to the positioning system. Its position is fixed during the measurements but can be changed (by hand) within the stiff frame. This implies that it is not possible to have a fixed origin of the coordinate system with respect to the locations of both transmitter and receiver (i.e. the location of the receiver is accurately known, but the location of the transmitter is not). To overcome this problem, the transmitter and receiver are positioned flat against each other prior to each measurement session. That particular location of the receiver then is taken as the origin and any following displacements are registered.

The data acquisition is controlled by an IBM XT computer. It reads the data-files from the scope and stores them on floppy discs. It also steers and registers the displacements of the positioning system. A plotter is connected to provide any graphical displays of the data.



Fig 5.2
Noise reduction by signal averaging
a) single shot
b) same trace after 1000 times
averaging

The accuracy of the data acquisition system is illustrated by fig 5.3. It shows the arrival time of an acoustic pulse in water at various transmitter-receiver distances. The receiver was stepped away from the transmitter with steps of 2 cm. At each increment the arrival time of the pulse was measured. The signal was averaged 500 times prior to the time measurement. The data show a straight line whose slope is proportional to the velocity in water. The line intersects the vertical axis at a value of $t_0 \approx 1.9 \mu\text{sec}$. This is caused by the delay time of the total system and by the fact that the transducers were not exactly touching at the start of the experiment.

The difference in arrival time between two successive steps is:

$$\Delta t = 13.55 \pm .02 \mu\text{sec} / 2 \text{ cm}.$$

It corresponds to a water velocity of $V_w = 1476 \pm 2 \text{ m/s}$.

The given inaccuracy of these values is very small and relates to the total acquisition system. It includes errors in measuring the arrival time, errors introduced by averaging the signal and inaccuracies in the positioning of the x-y-z system.

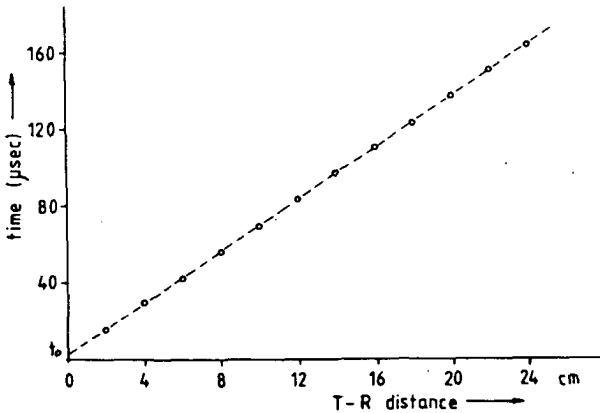


Fig 5.3 Arrival time of acoustic pulse in water versus transmitter-receiver distance

V.3 Transmission measurements

Acoustic transmission measurements through slices of rock provide a means to determine the properties of the bulk waves propagating through the rock sample. It is possible to detect not only the fast compressional wave and the shear wave, but also the slow compressional wave as predicted by Biot (1956a,b). The required rock samples are relatively small and therefore easy to manufacture. In the following sections, I describe the experiments, discuss the determination of the velocity and attenuation of the bulk waves in the rock, and then discuss the accuracy of the results.

V.3.1 Description of the experiments

The experimental technique is similar to the one used by Hartmann and Jarzynski (1974) and Plona (1980). The measurement configuration is depicted in fig 5.4. It consists of a pair of transducers with a rock sample placed in between. The sample is placed on a rotation table for varying the angle of incidence of the emitted wave. The total set-up is immersed in water to provide acoustic coupling.

An emitted pulse travels as a compressional wave to the rock. Upon reaching the rock surface, mode conversion occurs. Three bulk waves are generated in the porous rock: a fast compressional wave, a shear wave and a slow compressional wave. The raypaths of the bulk waves are refracted according to Snellius's Law. When the bulk waves reach the other side of the rock, they are converted again into compressional waves and are recorded by the receiver as compressional waves in the water.

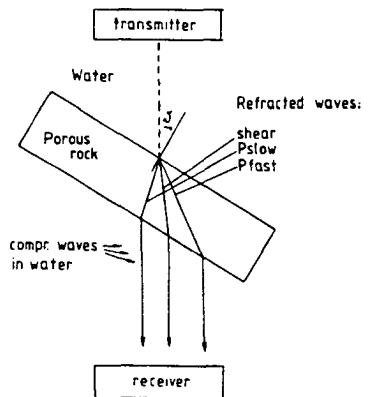


Fig 5.4 Configuration

When the bulk waves reach the other side of the rock, they are converted again into compressional waves and are recorded by the receiver as compressional waves in the water. The bulk waves propagate with different velocities in the rock and they therefore arrive at the receiver separated in time. Due to the directional characteristics of the transducers and to the dimensions of the rock sample, no wave is received that has diffracted around the block.

Although the wave velocities of the shear and slow compressional waves may be less than that of water, their responses are not obliterated by any direct wave in the water.

The mode conversions at the rock surface (and thus the recorded time trace) depend upon the angle of incidence, θ . Fig 5.5 shows four traces recorded on the same rock sample at different angles of incidence. The rock is an artificial sandstone sample cemented by araldite.

- $\theta = 0^\circ$ (fig 5.5A)

At normal incidence no shear waves are generated in the rock. The recorded trace shows a compressional wave (a) and multiple reflections equidistant in time (d,e). The slow P-wave (c) has a velocity which is approximately one-third the speed of the fast compressional wave. It therefore arrives close to the first multiple reflection.

- $0 < \theta < \theta_{\text{crit. P}}$

As the angle of incidence is increased to 35° (i.e. close to the critical angle of the fast P-wave), the trace given in fig 5.5B is recorded. The fast compressional arrival has weakened considerably while now the shear wave (b) is excited strongly. Multiple reflections of the fast P-wave have disappeared from the trace and the slow P-wave (c) stands out clearly. The fast P-wave shows a time-shift towards an earlier arrival time. The distance travelled through the rock becomes longer with increasing angle of incidence and because the fast P-wave velocity is higher than the speed in water, the pulse arrives sooner.

- $\theta > \theta_{\text{crit. P}}$

The angle of incidence is increased beyond the critical angle of the fast P-wave in fig 5.5C. Only two waves remain: the shear wave (b) and the slow P-wave (c). Both waves have a velocity that is slower than the velocity in water, so both waves exhibit a time-shift towards a later arrival time.

- $\theta = 70^\circ$

If the angle of incidence is increased still further (fig 5.5D, $\theta = 70^\circ$), both the shear wave and the slow P-wave remain present in

the recorded trace. The waves are slower than the wavespeed in water and they therefore do not refract critically.

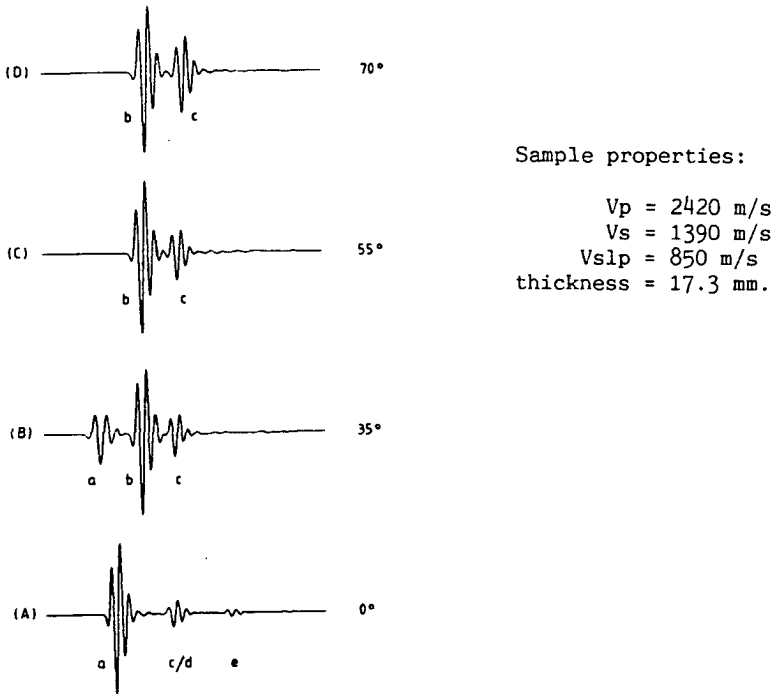


Fig 5.5 Recorded signals at different angles of incidence.
a) $\theta = 0^\circ$, b) $\theta = 35^\circ$, c) $\theta = 55^\circ$, d) $\theta = 70^\circ$
Amplitudes are normalized on highest peak in the trace.

It may be difficult to identify the arrivals of the three bulk waves in one single recorded trace. When the rock sample is thin, the separation in time between the various arrivals is minimal. In this case, it is convenient to perform measurements at several angles of incidence and plot the recorded traces in one single graph. An example is given in fig 5.6. The recorded acoustic traces are plotted versus the angle of incidence at increments of 5 degrees. The sample is an artificial sandstone cemented by araldite. Its thickness is 29 mm. The different waves are clearly identified. The first arrival is the fast P-wave. It disappears after the critical angle of incidence of around 40° is reached. Its velocity is faster than the wavespeed in water; the arrival bends to the left with increasing angle. The second arrival is the shear wave in the rock. It becomes visible at an angle of incidence of $15 - 20^\circ$ and is strongly generated at angles above 45° . Its velocity is less than the wavespeed in water; the curvature of the arrivals is

to the right. The third arrival is the slow P-wave. At small angles its arrival is drowned by the strong arrival of the first multiple reflection

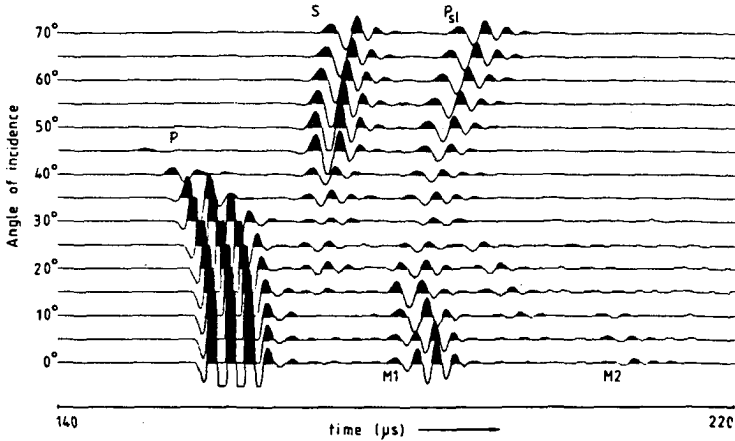


Fig 5.6 Recorded traces at increasing angles of incidence. Araldite cemented sandstone rock with thickness of 29 mm. Traces were averaged 1000 times.

tion of the fast P-wave. At increased angles (in this example at $\approx 25^\circ$) the multiple is not received anymore due to its side displacement. The distinction between the multiple reflection and the slow P-wave is easily made on account of the curvature of the arrivals in the plot. The fast P-wave is faster than the wavespeed in water, so the arrivals of the multiple reflection bend to the left, whereas the slow P-wave arrivals curve to the right.

V.3.2 Velocity determination

The velocity of the waves in the rock are determined by comparison of a recorded trace with a trace recorded in water only. If no rock sample is present, the arrival time of the pulse is simply given by the distance between the transducers (TRS) divided by the wave velocity in water:

$$T_{arr} = TRS / V_L \quad (5.1)$$

If a rock sample is placed between the transducers, the waves are refracted according to Snellius' Law:

$$V_L / V_r = \sin(\theta_i) / \sin(\theta_r) \quad (5.2)$$

in which

V_L, V_r = wave velocities in water and rock

θ_i, θ_r = angle of incidence and of refraction.

The raypath in the latter case is illustrated in fig 5.7. The difference in arrival time of a pulse between an experiment in water and an experiment with a rock sample, depends upon the velocity of the pulse in the rock (V_r) and the travelled distance in the rock (x).

The arrival time of a wave is now given by:

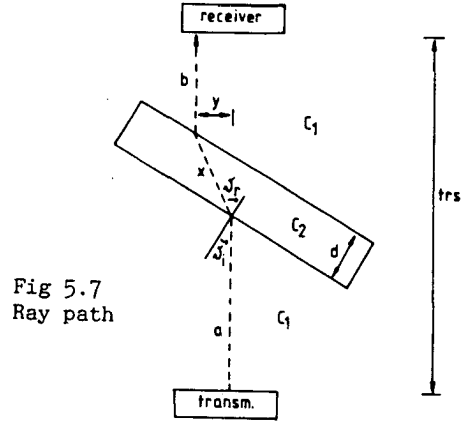


Fig 5.7
Ray path

$$T = [TRS - x \cos(\theta_r - \theta_i)] / V_L + x / V_r \quad (5.3)$$

Hence the difference between the arrival times with and without a sample, is:

$$\Delta t = T_{arr} - T = x \cos(\theta_r - \theta_i) / V_L - x / V_r \quad (5.4)$$

Furthermore,

$$x = d / \cos \theta_r \quad (5.5)$$

$$y = x \sin(\theta_r - \theta_i) \quad (5.6)$$

Substituting eqs. 5.5 and 5.2 into eq. 5.4, an expression for the velocity of the wave in the rock is obtained:

$$V_r = \frac{V_L}{\cos(\arcsin(\frac{V_r}{V_L} \sin \theta_i) - \theta_i) - \frac{\Delta t}{d} \frac{V_L}{\cos(\arcsin(\frac{V_r}{V_L} \sin \theta_i))}} \quad (5.7)$$

where V_L, V_r = velocities in water and rock
 θ_i = angle of incidence
 d = thickness of rock sample
 Δt = difference in arrival time of a pulse between an experiment in water and an experiment with a rock sample placed between the transducers.

After an initial estimate, V_r is calculated from eq. 5.7 by iteration. The iteration is stopped when the difference in V_r in two successive steps is less than 1 m/s.

Once the velocity in the rock is known, the travel distance of the wave inside the block, x , and the traverse displacement, y , can be calculated from eqs. 5.2, 5.5 and 5.6. The equations are applicable to all three bulk waves in the rock, i.e. the fast and slow P-waves and the shear wave.

In deriving the equations, several assumptions are implicitly made, i.e.:

- the emitted wave is a plane wave
- the emitted sound beam is straight and parallel
- the rock is homogeneous
- the flat faces of the rock are parallel.

The validity of these assumptions was confirmed experimentally and is discussed in section V.3.4, where the accuracy of the results from the transmission measurements is discussed.

A complicating factor in the determination of the arrival time of the wavelet required in eq. 5.7, is that in an attenuating medium the velocity is dispersive and the frequency content of a pulse changes as it travels along, due to the preferential damping of the higher frequencies. This causes the received wavelet to have a very gentle onset and the measured first arrival time appears to be dependent on the sensitivity setting of the oscilloscope. This is illustrated in fig 5.8. Fig 5.8a shows a pulse recorded with a maximum voltage range of 5 Volts set on the scope. As the scope contains an 8-bits A/D-converter, the maximum number of levels of detection is 256 and the minimum voltage level that can be detected, is 19.5 mV. Fig 5.8b shows the same trace, but now the sensitivity of the scope is increased by a factor 10. The first detectable negative offset now is 1.95 mVolt.

So, to measure the arrival time of the wavelet either a minimum detection level has to be set for the first arrival, or a cross-correlation technique has to be used.

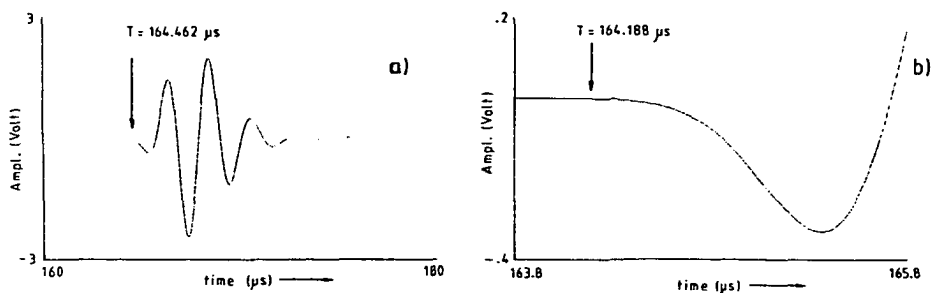


Fig 5.8 Arrival time of a wavelet recorded with different A/D converter sensitivity settings.
 a) minimum A/D level = 19.5 mV
 b) minimum A/D level = 1.95 mV

Fig 5.9 shows the velocities of the P-wave, the shear wave and the slow P-wave, calculated from the recorded traces shown in fig 5.6. The angle of incidence was varied from 0° to 70° in steps of 5° . For each angle, the first arrival time was determined for each wave using a minimum detection level of 1 % of the highest amplitude of the wavelet, and the velocity was calculated according to equation 5.7. The velocities are:

P-wave	:	2464 m/s
Shear wave	:	1344 m/s
slow P-wave	:	891 m/s

The calculated velocity values show a slight scatter of $\pm 0.5\%$, but do not depend upon the angle of incidence. The calculated velocity of the P-wave decreases slightly close to its critical angle. The shear wave is clearly present in the recorded traces from an angle of 45° onwards. Its velocity then remains constant. This also holds for the slow P-wave.

The travel distance through the block for the compressional wave is about twice as long at an angle of incidence of 30° as at an angle of 0° . The calculated velocity for both angles is the same. It appears that the dispersion and attenuation effects as discussed before, do not significantly affect the determined first arrival time. The samples are too thin for the effects to become noticeable. So the first arrival time of a wavelet provides a measure for the velocity of the rock sample. The slight scatter in the data can be suppressed by averaging

the velocities determined at different angles of incidence. This method was used to determine the velocities in the rest of this chapter.

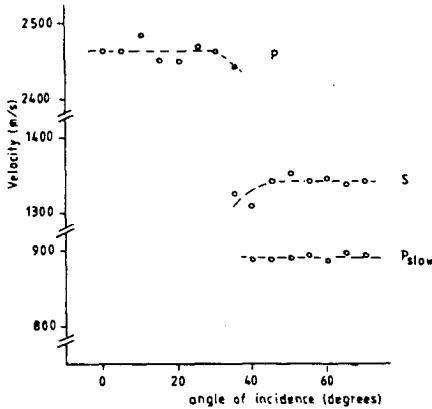


Fig 5.9 Velocity calculated from first arrival time of the recorded wavelets versus angle of incidence. Data from fig 5.6

V.3.3 Attenuation determination

The attenuation of the waves is determined from the recorded signals by comparing the amplitude spectra recorded on two slices of the same rock sample, but with different thicknesses. Because attenuation implies a preferential loss of the high frequencies, a change in the amplitude spectra occurs as a wave travels along. This change is linked to the attenuation coefficient.

The spectral amplitude of a wave can be written (Ward and Toksöz, 1971)

$$A(f,x) = G A_0(f) \exp [- \alpha(f) x] \quad (5.8)$$

where

G = geometrical factor including spreading, transmission and reflection,

$\alpha(f)$ = attenuation coefficient,

x = distance travelled,

f = frequency.

The ratio of the amplitudes for two slices of rock then becomes:

$$\ln \frac{A_1(f,x_1)}{A_2(f,x_2)} = \alpha(f) [x_2 - x_1] + \ln (G_1/G_2) \quad (5.9)$$

where x_1 and x_2 are the thicknesses of the slices.

Furthermore, the attenuation coefficient α is a linear function of the frequency for a given sample (Ward and Toksöz,1971, Bourbie et al,1987)

$$\alpha(f) = \pi f / Q(f) V \quad (5.10)$$

with $Q(f)$ = quality factor and V = velocity.

Strictly speaking, equation 5.10 does not satisfy causality (Aki and Richards, 1980, p. 171). But if the difference in thickness of the two slices is small, then significant dispersion effects have no time to occur and equation 5.10 may be used as a first approximation (Bourbie et al, 1987).

The term $\ln (G_1/G_2)$ is independent of the frequency for a given measurement set-up, so by comparing measurements on two slices of the same rock sample but with different thicknesses, the attenuation coefficient can be determined from the slope of the plot of $\ln (A_1/A_2)/[x_2 - x_1]$ versus frequency. The technique is illustrated in fig 5.10, which shows the determination of the attenuation coefficient of the P-wave from three slices of the same rock sample. The measurements were carried out at an angle of incidence of 0° . Fig 5.10a shows the amplitude spectra of the recorded traces. Figs 5.10b and c are the spectral ratios of the

Table 5.1

slice no.	thickness	P velocity	α (f_{centre})
1	5.13 cm	2454 m/s	
2	2.71	2464	$\alpha_{1-2} = 21.4$ 1/m.
3	2.04	2456	$\alpha_{1-3} = 21.1$ 1/m.

combinations of slice 1 with slices 2 and 3. The attenuation coefficients at the centre frequency compare very well for the two combinations, i.e. $\alpha_{1,2} = 21.4$ 1/m and $\alpha_{1,3} = 21.1$ 1/m. This shows that the original rock sample, from which the three samples were sawn, was homogeneous (This was also indicated by the P-wave velocities of the three slices, which are the same).

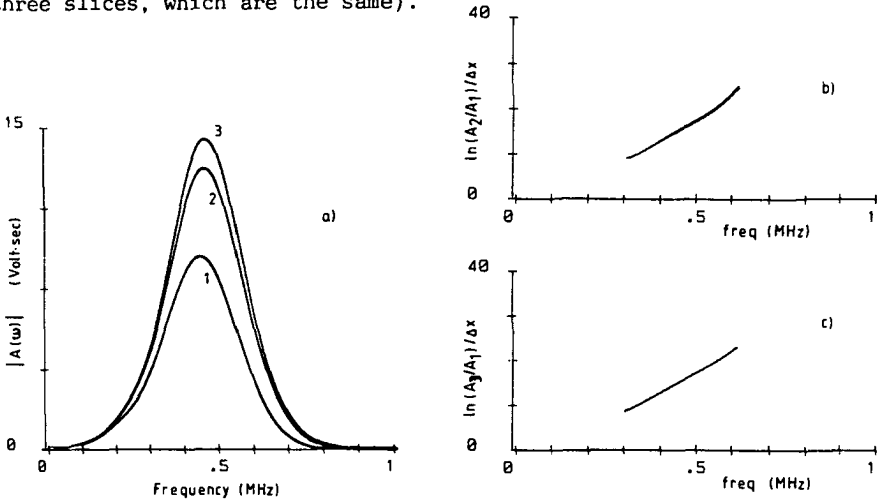


Fig 5.10 Determination of attenuation coefficient by spectral amplitudes on three slices of a rock sample
a) Amplitude spectra b,c) Amplitude ratios

The technique requires a signal which is not disturbed by other arrivals. The wavelets have to be completely separated in time; later arrivals should not be overlapping the tail end of the wavelet of interest. The traces therefore have to be measured at the angles of incidence where this does not happen to the wavelet of interest. A taper then can be applied to remove the unwanted arrivals from the trace.

Typical attenuations measured on the synthetic samples, are:

P- wave : $\alpha \approx 10 - 20$ 1/m., $Q \approx 60 - 30$

S-wave : $\alpha \approx 35$ 1/m., $Q \approx 31$

Psl-wave : $\alpha \approx 110$ 1/m., $Q \approx 17$

These values compare well with experiments reported in the literature for saturated sandstones, where Q-factors range from 10 to 50 (Bourbie 1987, Johnston et al 1979, Toksöz et al. 1979). The quality factors always appear to be lower for shear than for (fast) compressional

waves. Comparing the results from the synthetic samples with predictions calculated by the Biot theory ($\alpha_p \approx 0.4$, $\alpha_s \approx 10$ and $\alpha_{psl} \approx 180$ 1/m., refer fig 4.1), it appears that the predictions for the shear and compressional waves are much lower than the measured values. For the slow P-wave, on the other hand, it predicts a higher attenuation coefficient. The major trend, however, is the same for the measured values and the predictions.

V.3.4 Accuracy

The calculation of the velocity and attenuation from the transmission measurements is sensitive to several experimental errors, such as inhomogeneity of the rock, dispersion effects, divergence of the sound beam, small inaccuracies in the determination of the angle of incidence and in the thickness of the sample, non-parallelism of the faces of the rock, etcetera. Most of these effects can be determined experimentally. Dispersion appears not to have a significant effect on the calculated results, because the velocity is constant for varying angles of incidence. Since the length of the ray path through the rock varies with the angle of incidence (increasing the angle from 0° to 35° increases the travel path by a factor 2 for the P-wave, for instance), the travel distances appear to be too short for the dispersion effects to become noticeable. Inhomogeneities and non-parallelism of the faces of the rock also will become apparent as a velocity varying with angle of incidence.

The measurements are performed in the far field of the transducers (appendix D). This ensures that the emitted wave is a plane wave and that the spreading of the sound beam is negligible.

More random effects, such as the time span associated with one A/D-level and small inaccuracies in the setting of the angle of incidence, are levelled out by averaging the velocity values obtained at the various angles of incidence.

All in all, the calculated velocity values are accurate to within $\pm 1\%$ if the experiments are executed carefully.

For the determination of the attenuation coefficients, the accuracy is much less. To begin with, the measurements are performed under water. The electric contacts therefore are liable to slight corrosion, which

manifests itself directly in a reduced strength of the received signal. To circumvent these effects, a reference signal has to be recorded to which all other measurements are normalized. The signal recorded in water is chosen as the standard for the experiments. During each measurement session at least one water signal is recorded to which all recorded traces are normalized. The normalized traces of the sample then can be compared.

The experimental errors are equal to the ones discussed above and can be checked likewise. For a correct measurement of the received amplitudes, the receiving transducer has to be displaced sideways. The ray path of a wave leaving the sample is displaced from the incoming wave over a distance proportional to the angle of incidence (fig 5.7). As the region of highest sensitivity of the transducer is restricted to the middle area of its surface, the receiver has to be displaced sideways until the strongest signal is received. This provides another check on the geometrical errors. At a certain angle of incidence the measured displacement should be equal to the displacement calculated by equation 5.6.

The measurements are performed on thin slices of rock. The difference in travel paths between two slices is small, so a small error in the travel distance has a relatively high contribution to the inaccuracy of the calculated attenuation coefficient. But the biggest difficulty is the small bandwidth of the transducers. The attenuation coefficient is determined from the slope of the spectral amplitudes versus frequency. As the frequency bandwidth is small, the slope has to be determined from a very small region in the plot. This contributes significantly to the inaccuracy. In general, the accuracy of the attenuation coefficient from the spectral amplitudes is believed to be within 10 - 20 % (Bourbie 1987)

V.4 Refraction measurements

A second type of acoustic measurements which is performed, is the so-called refraction measurement. In a refraction experiment the transmitter and receiver are both located on the same side of the rock to be measured. The transmitter emits a pulse which is refracted critically at the rock surface. The wave travels through the rock just below its

surface and is recorded by the receiver. Such experiments exhibit a much closer resemblance to the measurements made in actual borehole logging than do the transmission measurements. Using the transmission technique, it is possible to measure the bulk waves in the rock, whereas the refraction experiments, as in actual logging, only record the waves that radiate away from the rock surface.

V.4.1 Configuration

The configuration of the measurements is depicted in fig 5.11. It consists of a rock sample with a flat surface submerged in water. The transmitter and receiver are located in the water above the rock. As a wave reaches the rock, it generates P, slow P and shear waves in the rock as well as surface waves which propagate along the interface. Waves in the rock, whose velocities are higher than the wavespeed in water, radiate back into the water and are picked up by the receiver.

This means that the slow P-wave with a velocity of 900 m/s as opposed to the water velocity of 1500 m/s, is not recorded in these experiments.

The rock sample is a cube with ribs of 40 cm. The dimensions are chosen this large to ensure that multiple reflections from the sides and bottom of the sample, do not interfere with the arrivals of interest. Any reflections from the water surface can simply be eliminated

by increasing the thickness of the water layer on top of the sample.

A seismic record is constructed by moving the receiver away from the transmitter in a horizontal plane and recording the acoustic signals at equidistant intervals. Such a scan is plotted in fig 5.12. The sample is an artificial sandstone cemented by araldite.

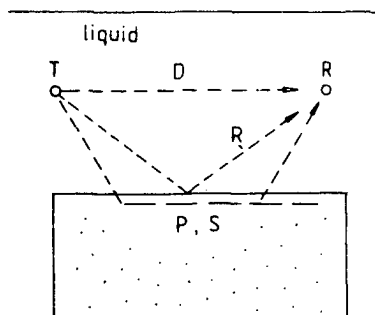


Fig 5.11 Configuration

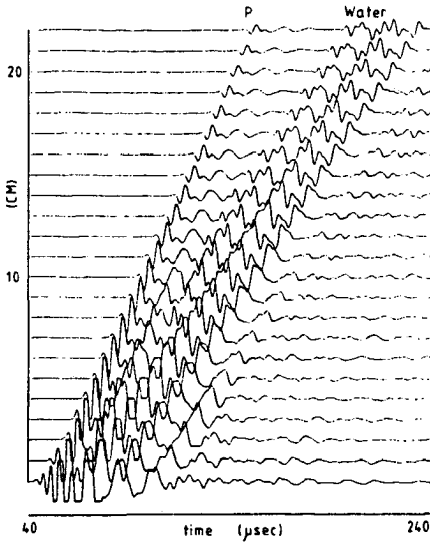


Fig 5.12
Acoustic scan on
artificial rock sample.
step interval = 1 cm.
250 kHz transducers.

In the plot the arrivals of the compressional wave and the wave in the water that has reflected once on the rock surface, can clearly be distinguished. The velocity of the waves is given by the slope of the line connecting the arrival times. For the compressional wave this results in: $V_p = 2320$ m/s.

V.4.2 Optimisation of the measurements

The refraction measurements are still in an early experimental stage. Several scans were recorded, predominantly to optimise the measurement configuration.

From the orientating experiments several conclusions can be drawn:

- 1) The sample dimensions (40×40×40 cm) are large enough to prevent any multiple reflections from interfering with the arrivals of interest. The path length of the multiple reflections is so large that the arrivals fall outside the recorded time window.
- 2) The direct wave through the water and the reflection on the rock surface can to a large extent be shielded from the recorded trace by placing an aluminum reflector or a sponge between the transducers.
- 3) The directional characteristics of the transducers require that a wave is emitted close to its critical angle for it to be detected by the receiver. It implies that separate scans with different angles

of incidence are necessary to detect the compressional and the shear waves.

- 4) As predicted by the theoretical modelling, the shear wave can be detected if the sample is submerged in silicon oil instead of water. The velocity of the shear wave is such ($V = 1300$ m/s) that the wave radiates into the immersion liquid when the liquid is oil ($V = 980$ m/s), but not when the liquid is water ($V = 1500$ m/s). An example of these measurements is shown in section V.6.
- 5) No surface waves were observed in any of the scans. This was probably due to the location of the transducers. The dimensions of the transducers and their directional characteristics hamper their positioning close to the rock surface. Furthermore, the theoretical modelling shows that due to the small wavelengths, the amplitude of the surface waves has already died away at distances of a few millimeters away from the rock surface. So to measure the surface waves, a different set of transducers should be purchased. They preferably should be strip transducers, which do not exhibit a strong directional sensitivity and therefore can be located very close to the rock surface.

V.5 Measurement results

A range of artificial rock samples varying in grain size and cement content, has been constructed. The resulting samples differ mainly in permeability and rock strength. Currently, these samples are being investigated using the acoustic transmission technique and the measurements are being interpreted. The present section of the thesis reports on the results obtained so far.

V.5.1 Samples

The samples that were used in the transmission measurements are listed in Table 5.2. All samples consist of sand grains cemented by araldite. The cement content was varied by changing the araldite/acetone ratio in the fabrication process.

Table 5.2 Sample properties.

Sample nr.	grain size (μm)	porosity % BV	permeability (Darcy)	araldite/acetone ratio
1	130	34.9	2.3	1:2
2	130	38.7	4.2	1:2
3	130	41.8	3.3	1:2
4	320	36.4	20	1:2
5	320	37.2	21.7	1:2
6	320	37.9	20	1:2
7	320	36.6	12.9	1:1
8	320	36.8	14.1	1:1
9	320	36.5	15.5	1:1
10	170	37.1	3	1:3
11	170	39.8	6.4	1:3
12	170	39	6.9	1:3
13	130	39.1	6	1:3
14	130	42.7	6.8	1:3
15	130	46.2	8.6	1:3
16	170	37.9	-	1:2
17	170	34.2	-	1:2
18	170	37.5	-	1:2
19	170	38.9	-	1:2
20	170	36.8	10.8	1:2
21	170			1:2
22	170			1:2
23	230	36.6	18	1:2
24	230			1:2
25	230			1:2
26	130	39.1	6.8	1:2
27	130			1:2
28	130			1:2
29	320	39.8	33.5	1:2
30	320			1:2
31	320			1:2

The permeability and porosity of all samples were measured. The permeability was determined by forcing water through the samples of known dimensions at a constant pressure differential. From the measured flow rate, the permeability was calculated by way of Darcy's Law. The porosity was determined on small plugs (2 cm diameter) taken from the samples, using a porosimeter as well as the wet-and-dry-weight method. However, an accurate determination of the bulk volume of the plug, required for both methods, proved to be a problem. The usual procedure of measuring the bulk volume in the porosimeter by submerging the plug in mercury, did not work properly. The mercury invaded the plugs slightly, due to the large pore throats of the samples. This resulted in a porosity determined by the porosimeter, which was too small. On the other hand, the determination of the bulk volume of the plugs by measuring the dimensions with a vernier caliper, did not account for the surface rugosity of the plugs. It yielded a value which was slightly too large and consequently, the wet-and-dry-weight method gave too high porosity values. The porosity of the plug then was approximated by averaging the results of the two methods. This gave a porosity for each sample with an accuracy of approximately ± 1 porosity percent.

V.5.2 Results

Type of cement

Fig 5.13 shows the P-wave and shear wave velocity versus the angle of incidence for three different types of synthetic porous materials. Sample A is a glass filter plate, consisting of glass sintered together. Sample B is an artificial sandstone cemented by silicon tetrachloride and sample C is a sandstone cemented by araldite. The porosity of all three samples is 39 % BV. The glass plate has a high rock strength. Its velocities are high, but it is very inhomogeneous. The velocity of the P-wave varies with the angle of incidence from 3135 to 2578 m/s. The two artificially made reservoir rock types both are homogeneous. The sample made using silicon tetrachloride has slightly higher P- and S-wave velocities than the araldite sample. This is no surprise: the sample is cemented by amorphous quartz which probably has a P-wave velocity of around 4000 m/s, depending on the amount of micro

porosity present. The araldite cement on the other hand, has a velocity of only 2000 m/s.

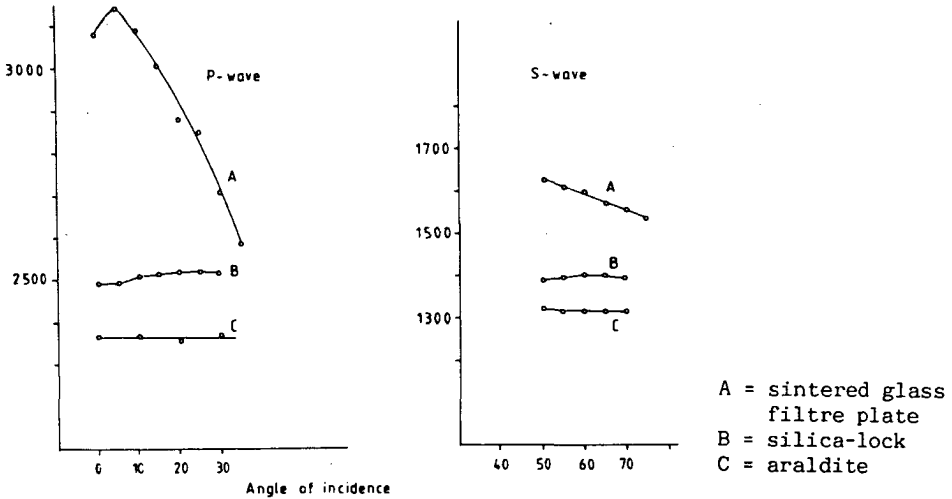


Fig 5.13 Velocity of compressional and shear wave versus angle of incidence for three types of porous media.

Fracture-like irregularities

The irregularities which were observed on the samples cemented by silicon tetrachloride, appear not to influence the acoustic response of the sample. A comparison of two samples of which only one showed such a fracture-like irregularity, indicated no difference in received acoustic signal, both for transmission and refraction measurements. This is consistent with the observation made in chapter 3 that, although a sample may exhibit such an irregularity, it is not accompanied by a reduction in elasticity modulus.

Velocity versus porosity

The porosity is plotted versus the P- and S-wave velocities in figs 5.14a and b for the samples listed in Table 5.2. The velocities of both waves decrease with increasing porosity. By linear regression a best-fit line is drawn in both plots. This yields for the compressional wave:

$$V_p = 3933 - 39.2 \phi \tag{5.11}$$

and for the shear wave:

$$V_s = 3455.6 - 55.6 \phi \quad (5.12)$$

In both equations the porosity is expressed as percentage of the total bulk volume. The accuracy of these equations is small due to the inaccuracies in the porosity values and the very limited range over which the correlation is established.

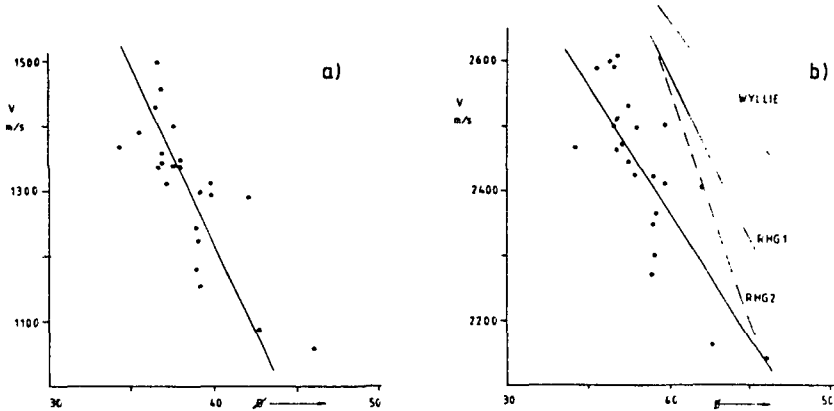


Fig 5.14 Velocity versus porosity
a) shear wave b) compressional wave

The Wyllie time average equation is drawn in fig 5.14b. The equation is expressed as:

$$\phi = \frac{\Delta t - \Delta t_{ma}}{\Delta t_{fl} - \Delta t_{ma}} * 1 / Bcp \quad (5.13)$$

where ϕ is porosity and Δt , Δt_{ma} and Δt_{fl} are the interval transit times of the rock, the matrix and the pore fluid, respectively.

The Wyllie equation yields good porosity estimates in formations with low to medium porosity, but in unconsolidated sands it calculates a porosity from the velocity data, which is too high. In these circumstances, an empirical correction factor is applied to the equation, Bcp. The factor actually corrects for the lack of good acoustic coupling between grains at the high porosities occurring in these circumstances. It ranges from 1 to 1.6, depending on the formation encountered (in fig 5.14b the relation is drawn using Bcp = 1).

As is to be expected, a similar phenomenon is observed for the synthetic rock samples. The samples are consolidated by compacting loose sand grains and afterwards adding cement to glue the grains together. Thus the nature and the distribution of the grain contacts is more or less similar to those of unconsolidated sands. In the artificial samples, any near-contacts between the grains are filled with cement, but the cement itself is an acoustically slow medium. Hence, a similar dependence of velocity on the porosity is found for the synthetic samples as for "unconsolidated" sands. The relation between the velocity and porosity of the synthetic rock samples runs parallel to the Wyllie equation, but is shifted to the left (fig 5.14b). Using a correction factor of $B_{cp} = 1.4$ would bring the Wyllie equation in perfect agreement with the velocities measured on the artificial rock samples.

The same results are obtained when a porosity vs. velocity relation proposed by Raymer et al. (1980) is used. Their proposed transform is based entirely on comparisons of independent porosity measurements and velocity data. Unfortunately they gave no details of their data. The proposed relation is split up into three separate porosity ranges: from 0 - 37 % (shown as RHG1 in fig 5.14b), from 37 - 47 % (RHG2), and for porosities higher than 47 % . The first part represents the range in porosities normally encountered in reservoir rock, the second part unconsolidated sands and the third part represents newly deposited sediments and suspensions of particles in liquids. Here again, the part representing the unconsolidated sands gives a better fit to the measured velocities.

So it appears that the artificial rock samples behave as natural high-porosity reservoir rock. The Wyllie equation indicates porosity values which are too high compared with the independent porosity measurements, but a very good fit is obtained when a compaction factor of $B_{cp} = 1.4$ is used. This seems to confirm the validity of the porosity versus velocity relation obtained for the synthetic rock samples (eq. 5.11). No empirical field equations are available to check the relation between porosity and shear wave velocity (eq. 5.12). But the constant shear to compressional velocity ratio (which is discussed in the next section) implies that the shear wave velocity versus porosity relation exhibits the same behaviour for the synthetic samples as for natural rock. Equations 5.11 and 5.12, however, do not present a means to

remove the problems encountered in the porosity determination of the synthetic rock samples by the standard methods. The scatter in the data is too large for that. To improve this situation, a set of rock samples should be manufactured which cover a wide range of porosity values (by changing the sorting of the sand grains). Velocity measurements then can give a more accurate relationship valid for a wider porosity range. This also becomes important when, in the follow-up project, measurements are to be performed on natural reservoir rocks. In general, these rocks will have a lower porosity than the synthetic samples and the relations valid for high porosities cannot simply be extrapolated towards lower porosity ranges.

Compressional versus shear velocity

The compressional velocity is plotted versus the shear velocity in fig 5.15. The plot shows a very good correlation with a constant velocity ratio of:

$$V_p / V_s = 1.89 \quad (5.14)$$

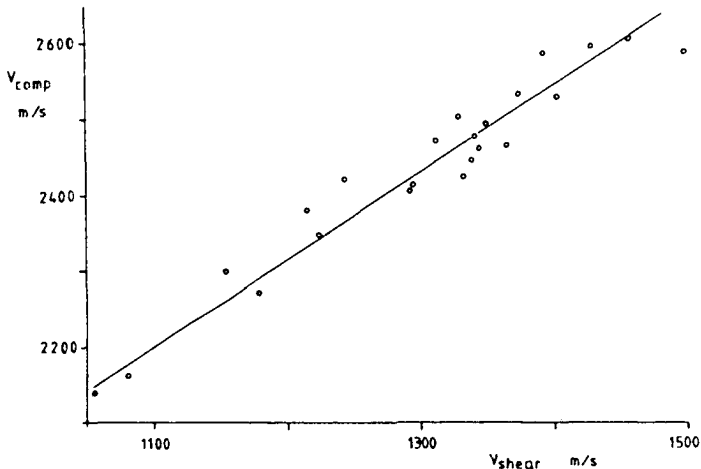


Fig 5.15 Compressional versus shear velocity

This value is characteristic for the sandstone samples cemented with araldite. A constant velocity ratio for a given rock type is consistent with the results from the field studies in chapter 2 and with observations reported in the literature (Pickett 1963, Nations 1974). The field examples, however, show significantly lower velocity ratios (i.e

≈1.6). This is probably due to the fact that the empirical values are established under in-situ circumstances (high confining stress).

Quantity of cement

In principle, the amount of cement in a sample can be calculated from the equations:

$$\rho_b = V_q \rho_q + V_c \rho_c, \text{ with } V_q + V_c + \phi = 1 \quad (5.15)$$

where ρ_b = bulk density of the sample

ρ_q, ρ_c = density of quartz respectively cement

V_q, V_c = volume fraction of quartz respectively cement

ϕ = porosity

For the synthetic samples the application of equation 5.15 does not give significant results. The quantity of cement in these samples ($\pm 2\%$ of the total volume) is too small in comparison with the inaccuracies in the porosity values. The quantity of cement that is calculated is 1 - 2% of the total sample volume, regardless of the araldite/acetone ratio during the fabrication process. But a qualitative impression of the influence of the amount of cement can be obtained by comparing the acoustic response of samples manufactured with a different araldite/acetone ratio. For this purpose we can compare samples 4, 5 and 6 with samples 7, 8, and 9 from Table 5.2. All six samples have the same grain size. Samples 7, 8 and 9 were constructed using a twice as high araldite/acetone ratio. These samples are therefore expected to contain approximately twice as much araldite as samples 4, 5 and 6. The results of the velocity measurements on these samples are:

sample	ϕ	permeability	V_p	V_s	V_{slp}	araldite/ acetone
4	36.4	20	2461	1344	892	1:2
5	37.2	21.7	2444	1338	872	1:2
6	37.9	20	2494	1348	865	1:2
7	36.7	12.9	2590	1498	911	1:1
8	36.8	14.1	2607	1457	901	1:1
9	36.5	15.5	2598	1423	900	1:1

Samples 4, 5 and 6 have a permeability which is significantly higher than samples 7, 8 and 9, whereas the porosity is more or less the same for all samples (keeping in mind the accuracy of the porosity of $\pm 1\%$ BV). Furthermore a large difference in compressional and shear wave velocity is noticed for the two sets of samples. The small difference in porosity between the two sets cannot explain the difference in velocity (refer eqs. 5.11 and 5.12). It has to be accounted for by a larger quantity of cement. So it seems that for the synthetic rock samples, the compressional and shear wave velocities are sensitive to the quantity of cement in a sample. When comparing the acoustic responses of two different rock samples, this has to be taken into account. In the future project therefore, an effort should be made to develop a method which accurately determines the quantity of cement in the samples.

V.5.3 Modelling

The slow P-wave can clearly be distinguished in the transmission measurements. The coupling of the solid grains with the fluid in the pores of the rock, as described by the Biot theory, therefore plays an important role. The Biot theory is at least qualitatively applicable to the synthetic rock samples. The velocities predicted by the theory agree well with the velocities measured on the samples. The attenuation predicted by the theory for the compressional and shear waves of a reservoir rock similar to the synthetic rock samples, is significantly less than the attenuation actually measured (refer V.3.3). The difference can partly be explained by losses due to solid-solid friction at the grain contacts. The Biot theory does not incorporate this. It only accounts for the solid-fluid friction due to microscopic fluid flow in the pores. Another reason may be the existence of inaccuracies in the values for the input parameters of the model. The Biot theory requires the specification of eleven formation parameters. Most of these are readily measured but others, notably the moduli of compression, are not. For the latter, Biot and Willis (1962) indicated so-called jacketed and unjacketed compressibility tests to determine the elastic parameters of the rock. But these tests are hard to realize. However, even after fitting the input parameters, the discrepancy between the calculated and measured attenuation remained. So it appears

that attenuation mechanisms other than solid-fluid friction play an important role for the synthetic rock samples. It is thus highly recommended to incorporate internal losses due to solid-solid friction at the grain boundaries in the Biot model.

Up till now, the theoretical models developed in chapter IV have merely been used to investigate the influence of formation parameters upon the received acoustic traces according to Biot, and to optimize the experimental configuration of the refraction measurements. The influence of formation parameters is discussed in chapter IV itself. The optimisation of the experimental configuration resulted in the detection of the shear wave, which hitherto had not been observed. This is illustrated by figures 5.16 and 5.17 which show a scan recorded with a rock sample placed under water and under silicon oil respectively. Both figures show a scan actually measured and a synthetic scan calculated for the same configuration.

The artificial rock sample was constructed using the silica-lock technique. The transducers were located at ± 7 mm above the rock surface. The direct wave and the reflection on the surface were shielded with an aluminum plate. The synthetic scans were calculated by the high frequency limit of the Biot theory. The input parameters were chosen such that $V_p = 2618$ m/s, $V_s = 1428$ m/s, $V_{psl} = 935$ m/s and $V_w = 1500$ m/s.

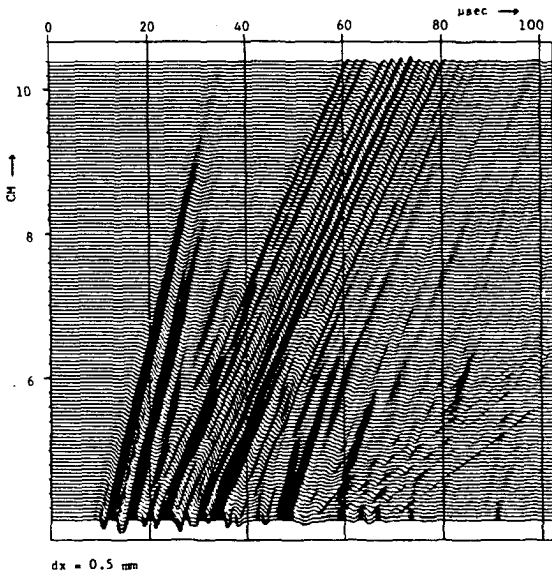


Fig 5.16
Sample under water
a) recorded scan
b) modelled scan

Fig 5.16a

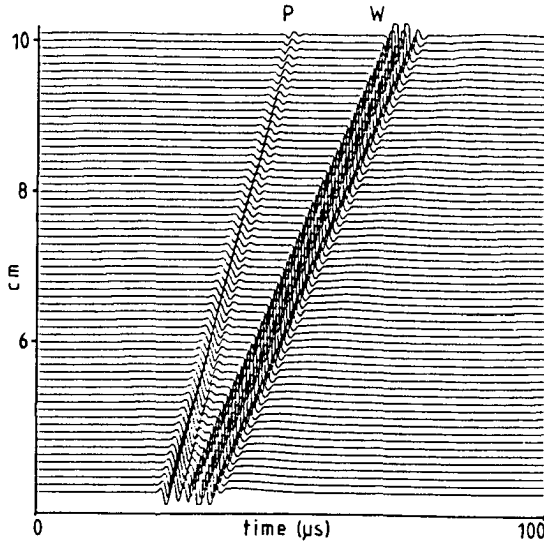


Fig 5.16b

Fig 5.16 shows the recorded and synthetic scans with the rock sample placed under water. In the modelled traces a compressional wave (P) and a reflection on the rock surface (W) are present. The shear wave does not radiate into the water because its velocity is lower than the wave speed in the water. Because the transducers are located relatively high above the rock surface (7 mm), no surface waves show up. The same arrivals are observed in the recorded scan (fig 5.16a).

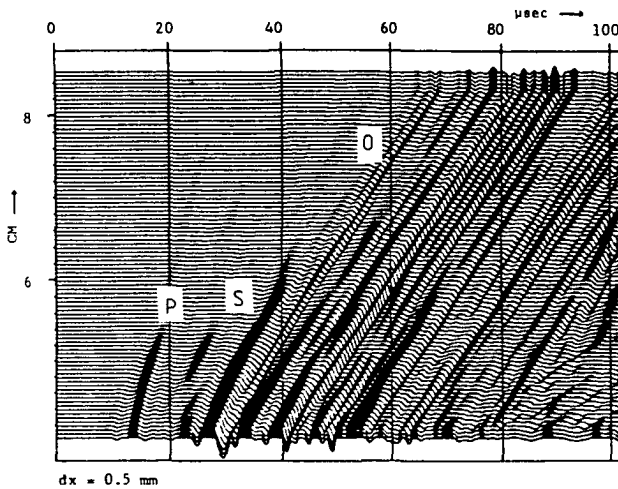


Fig 5.17
sample under
silicon oil
a) recorded scan
b) modelled scan

Fig 5.17a

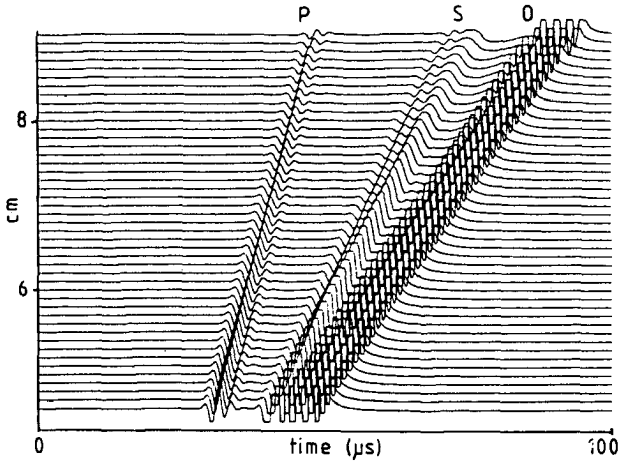


Fig 5.17b

Fig 5.17 shows the recorded and synthetic scans with the rock sample placed under a layer of silicon oil. In the modelled traces a shear wave (S) shows up, besides the compressional (P) and reflected (O) waves. In contrast to the previous scan, the shear wave now radiates into the liquid above the sample because its velocity is higher than the wave velocity in silicon oil (980 m/s). Again the same waves are noticed in the recorded scan.

These examples indicate that the theoretical modelling on the basis of the Biot theory, can very well be used to predict what will really be measured in a certain measurement configuration. The next step is to perform inverse modelling to calculate the formation parameters from the recorded acoustic traces.

V.6 Summary of results.

A general set-up has been built for performing acoustic measurements. Currently transmission as well as refraction measurements on a range of artificial rock samples are being performed and interpreted. The transmission measurements provide a relatively easy way to determine the properties of the bulk waves in the porous rock samples. The various arrivals are received separately in time and hardly any data processing

is necessary. The refraction measurements are still in an initial stage.

The measurement results obtained so far, show that the artificial rock samples are suited for acoustic research. The samples show an acoustic behaviour similar to the one encountered in natural high-porosity reservoir rocks. The porosity versus velocity relation agrees with the well-known Wyllie time average equation using a "compaction" factor of 1.4. This implies that the nature and distribution of the grain contacts in the synthetic samples cemented with araldite, are similar to the ones found in unconsolidated sandstones. The shear to compressional transit time ratio measured under atmospheric conditions, is constant and has a value characteristic for the synthetic samples. The compressional and shear wave velocities are sensitive to the quantity of cement in an artificial sample. They therefore can give an indication of the cement content of the samples.

The Biot theory appears to be qualitatively valid for the artificial rock samples. The slow P-wave is clearly observed in the transmission measurements. The attenuation of the bulk waves predicted by Biot, differs significantly from the measured values. It appears that losses due to solid-solid friction play an important role besides the solid-fluid losses as described by the Biot theory. It therefore seems necessary to incorporate these effects in the theory before inverse modelling can successfully be applied.

VI. CONCLUSIONS

1. An empirical approach to study the acoustic behaviour of rocks by comparing field data, encounters large difficulties in the correlation of a difference in acoustic response with one single rock property. At best, a broad, general trend can be found.
2. Artificial reservoir rock samples that are suited for acoustic research, can be manufactured in the laboratory using the silica-lock process or an araldite cement. One rock property of the samples can be changed, while the other properties are kept constant, thus enabling to study the influence of that particular rock property upon the acoustic response.
3. The artificial rock samples exhibit characteristics similar to natural reservoir rocks. Petrophysical correlations established in the field, apply to the synthetic rocks, too. The acoustic behaviour of the samples also agrees well with observations made in the field on high porosity rock and reported in the literature.
4. The existence of the slow compressional wave in the synthetic samples is verified unambiguously. The Biot theory therefore applies at least qualitatively to the samples.
5. The model incorporating the high frequency limit of the Biot theory predicts the arrivals of the waves in a refraction measurement correctly. It, however, does not include the influence of certain interesting formation properties such as permeability.
6. The model incorporating the full frequency range of the Biot theory, shows that the permeability has a large effect upon the amplitude with which the surface waves are generated at the liquid/porous rock interface.

7. Transmission measurements through a slice of rock sample provide a means to determine the properties of all bulk waves in the rock.
8. Under atmospheric conditions, the compressional-to-shear-wave-velocity ratio has a characteristic value for the synthetic rock samples. This value is independent of porosity.
9. The field studies indicate that full wavetrain logging can give a valuable contribution to formation evaluation.
10. The field study of the shaly sandstone formation showed that:
 - the shale fraction present in a reservoir can consist of a varying mixture of different clay minerals. In the sandstone formation studied, each mixture is characterized by its own 100 % wet shale point, resulting in a range of five shale points, each one valid for a different subinterval of the reservoir.
 - the five shale points can be obtained from the conventional logs.
 - as a result of the new evaluation method, the formation properties are determined more accurately. Ultimately, this results in a more accurate estimate of the hydrocarbon content of the reservoir.

RECOMMENDATIONS

With regard to the follow-up project, the following recommendations can be made from the present study:

1. A range of artificial rock samples should be manufactured which have a wider range of porosities, by changing the sorting of the grain size of the sand. This should enable the determination of the wave velocity vs. porosity relation more accurately for the synthetic samples. It may also facilitate the extrapolation of the laboratory results to field data in the future.
2. The effect of the quantity of cement in the artificial rock samples should be investigated more closely. A method should be developed to determine the quantity of cement in a sample, thus allowing these experiments to be performed under more controlled circumstances.
3. The consolidation of synthetic rock samples using the silica-lock process with kerosene as a carrier liquid, should be investigated experimentally. Proper silica-cemented samples are required for measurements under in-situ circumstances that are to be performed.
4. For the sake of inverse modelling, the quantitative applicability of the Biot theory has to be investigated.
5. The effects of solid-solid friction losses at the grain contacts should be incorporated in the theoretical models.
6. During the refraction measurements, attention should be focussed on the effect of permeability upon the surface waves as predicted by the theoretical modelling. The experimental set-up should be optimised to allow recording of these surface waves.
7. In natural reservoir formations, mudcake is present on the borehole wall. For a better understanding of its effect upon the acoustic response of a formation, measurements should be performed on rock samples with a simulated mudcake.

8. Acoustic measurements should be performed on natural reservoir rock as well as on artificial rock samples to facilitate the extrapolation of the results to field data.
9. Acoustic measurements have to be performed under in-situ circumstances in the 'borehole simulator' to determine the effect of confining stress upon the acoustic behaviour of the samples.
10. More field studies should be carried out over a wider range of different formations to determine the validity of the results of the two field studies contained in this thesis, in general. For this to provide optimal results, care should be taken to choose less complex formations.

References

- Aki, K. and P.G. Richards, 1980, Quantitative seismology, Theory and methods Vols. I & II, San Francisco, Freeman & Co.
- Archie, G.G., 1942, Electrical resistivity as an aid in core analysis interpretation, Trans. AIME, Vol. 146, pp 54-63.
- Aron, J., Murray, J. and B. Seeman, 1978, Formation compressional and shear interval transit time logging by means of long spacings and digital techniques, SPE paper 7446.
- Berryman, J.G., 1980, Confirmation of Biot's theory, Appl. Phys. Lett., Vol. 37 (4), pp 382-384.
- Berryman, J.G., 1981, Elastic wave propagation in fluid-saturated porous media, J. Acoust. Soc. Am., Vol. 69 (2), pp 416-424.
- Biot, M.A., 1956 (a), Theory of propagation of elastic waves in a fluid-saturated porous solid. I. Low-frequency range, J. Acoust. Soc. Am., Vol. 28 (2), pp 168-178.
- Biot, M.A., 1956 (b), Theory of propagation of elastic waves in a fluid-saturated porous solid. II. Higher frequency range, J. Acoust. Soc. Am., Vol. 28 (2), pp 179-191.
- Biot, M.A., 1962, Mechanics of deformation and acoustic propagation in porous media, J. Appl. Phys., Vol. 33 (4), pp 1482-1498.
- Biot, M.A. and D.G. Willis, 1957, The elastic coefficients of the theory of consolidation, J. Appl. Mech., pp 594-601.
- Bourbie, T., Coussy, O. and B. Zinszner, 1987, Acoustics of porous media, Paris, Technip
- Brie, A., Hsu, K. and C. Eckersley, 1988, Using the Stoneley normalized differential energies for fractured reservoir evaluation, SPWLA 29th Ann. Log. Symp., paper XX.
- Brown, R.J.S., 1980, Connection between formation factor for electrical resistivity and fluid-solid coupling factor in Biot's equations for acoustic waves in fluid-filled porous media, Geophysics, Vol. 45 (8), pp 1269-1275.
- Chin, R.C.Y., Berryman, J.G. and H.W. Hedstrom, 1985, Generalized ray expansion for pulse propagation and attenuation in fluid-saturated porous media, Wave Motion, Vol. 7 (1), pp 43-65.
- Davies, D.R. and F.H. Meijs, 1980, Silica-lock a novel sand-control process for gas wells, SPE paper 9423.
- de Hoop, A.T., 1960, A modification of Cagniard's method for solving seismic pulse problems, Appl. Sci. Res. Sec.B8, pp 349-356.
- de Hoop, A.T. and J.H.M.T. van der Hijden, 1984, Generation of acoustic waves by an impulsive point source in a fluid/solid configuration with a plane boundary, J. Acoust. Soc. Am., Vol 75, pp 1709-1715.
- de Vries, S.M., 1985, Generation of acoustic waves by an impulsive point source in a fluid/porous-medium configuration with a plane boundary, report nr 1985-05, TU Delft, depart. Electr. Eng.
- Deresiewicz, H. and R. Skalak, 1963, On the uniqueness in dynamic poro-elasticity, Bull. Seismol. Soc. Am., Vol 53, pp 783-788.
- Donker, J., 1986, Artificial sandstone made by Silica-locking: theoretical investigation of the hydrolysis of SiCl_4 and the nature of its reaction product SiO_2 , Internal report T.U. Delft, April 1986.
- Feng, S. and D.L. Johnson, 1983, High-frequency acoustic properties of a fluid/solid interface. I. New surface mode, J. Acoust. Soc. Am., Vol. 74 (3), pp 906-914.
- Feng, S. and D.L. Johnson, 1983, High-frequency acoustic properties of a fluid/solid interface. II. The 2D reflection Green's function, J. Acoust. Soc. Am., Vol. 74 (3), pp 915-924.

- Gassman, F., 1951, Über die Elastizität poröser Medien, Vierteljahresschrift der Naturforschenden Gesellschaft in Zürich, Vol. 96, pp 1-23.
- Geertsma, J. and D.C. Smit, 1961, Some aspects of elastic wave propagation in fluid-saturated porous solids, Geophysics, Vol. 26 (2), pp 169-181.
- Hartmann B. and J. Jarzynski, 1974, J. Acoust. Soc. Am., Vol 56, pp 1469-1478.
- Havenaar, I. and F.H. Meijs, 1963, Sand consolidation with epoxy-resin solutions, J. Inst. Petr. Vol.49, no. 480, pp 392-397
- Johnson, D.L. and T.J. Plona, 1982, Acoustic slow waves and the consolidation transition, J. Acoust. Soc. Am., Vol. 72 (2), pp 556-565
- Johnson, D.L., Plona, T.J., Scala, C., Pasierb, F. and H. Kojima, 1982, Tortuosity and acoustic slow waves, Phys. Rev. Lett., Vol. 49 (25), pp 1840-1844.
- Johnston, D.H., Toksöz, M.N. and A. Timur, 1979, Attenuation of seismic waves in dry and saturated rocks: II. Mechanisms, Geophysics, Vol.44 (4), pp 691-711.
- Juhasz, I., 1979, The central role of Q_v and formation-water salinity in the evaluation of shaly formations, The Log Analyst, July-August 1979, pp 3-13.
- Krautkrämer, J. and H., 1983, Ultrasonic testing of materials, 3rd ed., Springer Verlag, Berlin.
- Kuster, G.T., and M.N. Toksöz, 1974, Velocity and attenuation of seismic waves in two-phase media: I. Theoretical formulations, Geophysics, Vol. 39 (5), pp 587-606
- Lambe, T. W. and R. V. Whitman, 1969, Soil Mechanics, New York, Wiley
- Lebreton, F., Sarda, J.P., Trocqueme, F. and P. Morlier, 1978, Logging tests in porous media to evaluate the influence of their permeability on acoustic waveforms, SPWLA 19th Ann. Log. Symp., June 13-16, 1978, paper Q.
- Liu, O.Y., 1986, A new method of fracture detection using borehole sonic velocity measurements, SPWLA 10th Eur. Form. Eval. Symp., Trans., paper R.
- Mandel, P., Berg, J.W. and K.L. Cook, 1957, Resistivity studies of metalliferous synthetic cores, Geophysics, Vol. 22 (2), pp 398-411.
- Murphy III, W.F., 1982, Effects of microstructure and pore fluids on the acoustic properties of granular sedimentary materials, dissertation Stanford University.
- Nations, J.F., 1974, Lithology and porosity from acoustic shear and compressional wave transit time relationships, SPWLA 15th Ann. Log. Symp., Trans., paper Q.
- O'Connell, R.J., and B. Budiansky, 1977, Viscoelastic properties of fluid-saturated cracked solids, J. Geoph. Res., Vol. 82 (36), pp 5719-5735
- Ogushwitz, P.R., 1985, Applicability of the Biot theory. I. Low-porosity materials, J. Acoust. Soc. Am., Vol. 77 (2), pp 429-440.
- Perez-Rosales, C., 1982, On the relationship between formation resistivity factor and porosity, SPE J., august, pp 531-536.
- Pickett, G.R., 1963, Acoustic character logs and their applications in formation evaluation, J. Petr. Techn., June 1963, pp 659-667.
- Plona, T.J., 1980, Observation of a second bulk compressional wave in a porous medium at ultrasonic frequencies, Appl. Phys. Lett., Vol. 36, pp 259-261.

- Poupon, A., Clavier, C., Dumanoir, J., Gaymard, R. and A. Misk, 1970, Log analysis of sand-shale sequences: a systematic approach, *J. Pet. Tech.*, July 70
- Raymer, L.L., Hunt, E.R. and J.S. Gardner, 1980, An improved sonic transit time-to-porosity transform, *SPWLA, 21st Ann. Logg. Symp.*, July 1980
- Rosenbaum, J.H., 1974, Synthetic microseismograms: Logging in porous formations, *Geophysics*, Vol. 39 (1), pp 14-32.
- Stoll, R.D., 1974, Acoustic waves in saturated sediments, in: *Physics of sound in marine sediments*, ed. by L. Hampton, Plenum, New York, pp 19-39.
- Stoll, R.D. and G.M. Bryan, 1970, Wave attenuation in saturated sediments, *J. Acoust. Soc. Am.*, Vol. 47, pp 1440-1447.
- van Baaren, J.P., 1979, Quick-look permeability estimates using sidewall samples and porosity logs, *SPWLA 6th Eur. Symp. Trans.*, London.
- van der Grinten, J.G.M., van Dongen, M.E.H. and H. van der Kogel, 1985, A shock tube technique for studying pore-pressure propagation in a dry and water-saturated porous medium, *J. Appl. Phys.*, Vol. 58 (8), pp 2937-2942.
- van der Grinten, J.G.M., 1987, An experimental study of shock-induced wave propagation in dry, water-saturated and partially saturated porous media, dissertation T.U. Eindhoven.
- Viksne, A., Berg, J.W. and K.L. Cook, 1961, Effect of porosity, grain contacts, and cement on compressional wave velocity through synthetic sandstones, *Geophysics*, Vol. 26 (1), pp 77-84.
- Visser, R., Bours, K.A.T. and J.P. van Baaren, 1988, Effective porosity estimation in the presence of dispersed clay, *SPWLA 29th Ann. Log. Symp.*, Trans. paper BB.
- Visser, R. and J.P. van Baaren, 1985, Optimisation of the shale correction using well logs, *SPWLA 26th Ann. Log. Symp.*, Trans., paper C.
- Walsh, J.B., 1966, Seismic wave attenuation in rock due to friction, *J. Geoph. Res.*, Vol. 71 (10), pp 2591-2599.
- Ward, R.W. and M.N. Toksöz, 1971, Causes of regional variation of magnitude, *Bull. Seism. Soc. Am.* 61, pp 649-670
- Wyllie, M.R., Gregory, A.R. and L.W. Gardner, 1956, Elastic wave velocities in heterogeneous and porous media, *Geophysics*, Vol. 21 (1), pp 41-70.
- Wyllie, M.R.J., Gardner, G.H.F. and A.R. Gregory, 1962, Studies of elastic wave attenuation in porous media, *Geophysics*, Vol. 27 (5), pp 569-589
- Yew, C.H. and P.N. Jogi, 1976, Study of wave motions in fluid saturated rocks, *J. Acoust. Soc. Am.*, Vol. 60 (1), pp 2-8.

Appendix A. Biot theory; numerical description

For the sake of completeness a brief mathematical description of the theory is given below. The notation generally follows that of Johnson and Plona (1982).

Stress-strain relations

The relations between the average stresses in the solid and fluid part of the medium, σ_{ij} and $S\delta_{ij}$, and the average particle displacements are:

$$\sigma_{ij} = (P - 2N)\delta_{ij} \partial_k u_k + N(\partial_i u_j + \partial_j u_i) + Q\delta_{ij} \partial_k U_k \quad (A.1)$$

$$S\delta_{ij} = -\phi P_f \delta_{ij} = Q \delta_{ij} \partial_k u_k + R \delta_{ij} \partial_k U_k \quad (A.2)$$

where summation over x, y, z applies.

ϕ is porosity, P is the pore fluid pressure and u, U are the average particle displacements in the solid and fluid part. P, Q, R, N are the elastic parameters of the medium.

δ_{ij} is the kronecker delta.

Elastic parameters

By assuming that the porosity remains constant under the small strains typical of acoustic waves, the relations between the elastic parameters $\{P, Q, R, N\}$ and the bulk parameters of the material $\{\phi, \rho_f, K_f, \rho_s, K_s, K_b, N\}$ are given by: (Biot and Willis 1957, Geertsma and Smit 1961)

$$P = \frac{(1 - \phi) (1 - \phi - K_b/K_s) K_s + \phi K_s K_b / K_f}{1 - \phi - K_b/K_s + \phi K_s / K_f} + 4/3 N \quad (A.3)$$

$$Q = \frac{(1 - \phi - K_b/K_s) \phi K_s}{1 - \phi - K_b/K_s + \phi K_s / K_f} \quad (A.4)$$

$$R = \frac{\phi^2 K_s}{1 - \phi - K_b/K_s + \phi K_s / K_f} \quad (A.5)$$

Stoll (1974) introduced dissipation due to matrix anelasticity by allowing the bulk modulus of the skeleton, K_b , and the shear modulus, N , to be complex.

Wave equations

The particle displacement wave equations which result from eq. A.1 and A.2 are:

$$\rho_{11} \frac{\partial^2 \underline{u}}{\partial t^2} + \rho_{12} \frac{\partial^2 \underline{U}}{\partial t^2} = P \nabla(\nabla \cdot \underline{u}) + Q \nabla(\nabla \cdot \underline{U}) - N \nabla \times (\nabla \times \underline{u}) + b F(\kappa) \left(\frac{\partial \underline{U}}{\partial t} - \frac{\partial \underline{u}}{\partial t} \right) \quad (\text{A.6})$$

$$\rho_{12} \frac{\partial^2 \underline{u}}{\partial t^2} + \rho_{22} \frac{\partial^2 \underline{U}}{\partial t^2} = Q \nabla(\nabla \cdot \underline{u}) + R \nabla(\nabla \cdot \underline{U}) - b F(\kappa) \left(\frac{\partial \underline{U}}{\partial t} - \frac{\partial \underline{u}}{\partial t} \right) \quad (\text{A.7})$$

Mass coefficients

The mass coefficients ρ_{11} , ρ_{12} and ρ_{22} are related to the density of the solid and fluid part of the medium by:

$$\rho_{11} + \rho_{12} = (1 - \phi) \rho_{\text{solid}} \quad (\text{A.8})$$

$$\rho_{12} + \rho_{22} = \phi \rho_f \quad (\text{A.9})$$

$$\rho_{12} = -(\epsilon - 1) \phi \rho_f \quad (\text{A.10})$$

The term ρ_{12} describes the inertial drag that the fluid exerts on the solid as the latter is accelerated relative to the former.

Tortuosity

Following Johnson and Plona (1982) a complex, frequency dependent tortuosity is introduced:

$$\epsilon(\omega) = \epsilon + ibF(\kappa)/\omega\phi\rho_f \quad (\text{A.11})$$

The variable ϵ has been identified with the tortuosity (Wyllie 1962, Brown 1980) and is given by:

$\epsilon = \phi F$, where F is the formation resistivity factor from Archie's formula (1942). Berryman (1980) derived $\epsilon = 1/2 (\phi^{-1} + 1)$ for spherical solid particles.

Equations (A.6) and (A.7) now change to:

$$\rho_{11} \frac{\partial^2 \underline{u}}{\partial t^2} + \rho_{12} \frac{\partial^2 \underline{U}}{\partial t^2} = P \nabla(\nabla \cdot \underline{u}) + Q \nabla(\nabla \cdot \underline{U}) - N \nabla \times (\nabla \times \underline{u}) \quad (\text{A.12})$$

$$\rho_{12} \frac{\partial^2 \underline{u}}{\partial t^2} + \rho_{22} \frac{\partial^2 \underline{U}}{\partial t^2} = Q \nabla(\nabla \cdot \underline{u}) + R \nabla(\nabla \cdot \underline{U}) \quad (\text{A.13})$$

where now the mass coefficients are complex valued and

$$\rho_{12} = -(\epsilon(\omega) - 1) \phi \rho_f \quad (\text{A.14})$$

Dissipation factor

The parameters $b F(\kappa)$ appearing in eqs. A.6, A.7 and A.11 govern the attenuation due to fluid flow.

$$b = \eta \phi^2 / k, \quad \eta = \text{fluid viscosity, } k = \text{permeability} \quad (\text{A.15})$$

The function $F(\kappa)$ represents the deviation from Poiseuille friction between the fluid and the solid as the frequency increases. It has been defined as (Biot 1956a,b):

$$F(\kappa) = \kappa T(\kappa) / 4 [1 - 2 T(\kappa) / i\kappa] \quad (\text{A.16})$$

where $T(\kappa)$ is given by the complex Kelvin function:

$$T(\kappa) = (\text{ber}'(\kappa) + i\text{bei}'(\kappa)) / (\text{ber}(\kappa) + i\text{bei}(\kappa)) \quad (\text{A.17})$$

$$\text{and } \kappa = \delta (\omega \rho_f / \eta \phi)^{1/2} \quad (\text{A.18})$$

δ is a structural factor and has a value according to Biot of $\delta \approx \sqrt{8}$.

The parameter κ may also be defined as (Stoll 1974):

$$\kappa = a (\omega \rho_f / \eta)^{1/2} \quad (\text{A.19})$$

where a is a pore size parameter and has a value of approx. $1/6$ to $1/2$, of the dominant grain diameter.

Velocity

The velocities of the different waves are found by applying the divergence and curl operators to eq. A.12 and A.13.

This yields for the compressional waves:

$$(\rho_{11} \frac{\partial^2}{\partial t^2} - P \nabla^2) \nabla \cdot \underline{u} = (Q \nabla^2 - \rho_{12} \frac{\partial^2}{\partial t^2}) \nabla \cdot \underline{u} \quad (\text{A.20})$$

$$(\rho_{12} \frac{\partial^2}{\partial t^2} - Q \nabla^2) \nabla \cdot \underline{u} = (R \nabla^2 - \rho_{22} \frac{\partial^2}{\partial t^2}) \nabla \cdot \underline{u} \quad (\text{A.21})$$

There are two compressional waves whose wavespeeds are given by:

$$V_{\pm}^2 = \frac{B \pm (B^2 - 4AC)^{1/2}}{2A} \quad (\text{A.22})$$

$$\begin{aligned} \text{where } A &= \rho_{11} \rho_{22} - \rho_{12}^2 \\ B &= P \rho_{22} + R \rho_{11} - 2Q \rho_{12} \\ C &= PR - Q^2 \end{aligned}$$

The plus sign refers to the fast, the minus sign to the slow P-wave.

The curl operator applied to eqs. A.12 and A.13 gives:

$$\frac{\partial^2}{\partial t_2^2} (\rho_{11} \nabla \times \underline{u} + \rho_{12} \nabla \times \underline{U}) = N \nabla^2 (\nabla \times \underline{u}) \quad (\text{A.23})$$

$$\frac{\partial^2}{\partial t_2^2} (\rho_{12} \nabla \times \underline{u} + \rho_{22} \nabla \times \underline{U}) = 0 \quad (\text{A.24})$$

There is one shear wave with a velocity of:

$$V_s^2 = \frac{N}{\rho_{11} - \rho_{12}^2 / \rho_{22}} \quad (\text{A.25})$$

Particle displacement

If the relation:

$$\left(\frac{1}{V_{\pm}^2} \frac{\partial^2}{\partial t^2} - \nabla^2 \right) (\nabla \cdot \underline{u}_{\pm}) = 0 \quad (\text{A.26})$$

is substituted in eqs. A.20 and A.21, the relation between the particle displacement of the fluid part and the solid part of the rock, is found for the compressional waves:

$$\underline{u}_{\pm} = - G_{\pm} \underline{u}_{\pm}$$

$$\text{with } G_{\pm} = (V_{\pm}^{-2} \rho_{11} - P) / (V_{\pm}^{-2} \rho_{12} - Q) \quad (\text{A.27})$$

For the shear wave it follows directly from eq. A.24 as:

$$\underline{u}_s = - (\rho_{12} / \rho_{22}) \underline{u}_s = (\epsilon(\omega) - 1) / \epsilon(\omega) \underline{u}_s \quad (\text{A.28})$$

Attenuation

The attenuation coefficient α of the bulk waves is obtained by taking the imaginary part of the complex wave vector $q(\omega) = \omega / V(\omega)$.

Appendix B: Transforms

The wave constituents are first calculated in the transformed domain, i.e. after having carried out a Fourier transform with respect to time and to the coordinates x and y parallel to the interface.

The transforms are defined as follows for the quantity $p = p(x, y, z, t)$:

$$\hat{p}(x, y, z, \omega) = \int_{-\infty}^{\infty} e^{i\omega t} p(x, y, z, t) dt \quad (B1)$$

$$\tilde{p}(\alpha, \beta, z, \omega) = \int_{-\infty}^{\infty} \int_{-\infty}^{\infty} \int_{-\infty}^{\infty} e^{-i\omega(\alpha x + \beta y - t)} p(x, y, z, t) dx dy dt \quad (B2)$$

$$\hat{p}(x, y, z, \omega) = \frac{\omega^2}{4\pi} \int_{-\infty}^{\infty} \int_{-\infty}^{\infty} e^{i\omega(\alpha x + \beta y)} \tilde{p}(\alpha, \beta, z, \omega) d\alpha d\beta \quad (B3)$$

The back transform is:

$$p(x, y, z, t) = \frac{1}{2\pi} \int_{-\infty}^{\infty} e^{-i\omega t} \hat{p}(x, y, z, \omega) d\omega \quad (B4)$$

with the following transform pairs :

$$\begin{aligned} \partial_t p & \leftrightarrow -i\omega \tilde{p} \\ \partial_t^2 p & \leftrightarrow -\omega^2 \tilde{p} \\ \partial_x p & \leftrightarrow i\omega\alpha \tilde{p} \\ \partial_x^2 p & \leftrightarrow -\omega^2 \alpha^2 \tilde{p} \\ \nabla^2 p & \leftrightarrow \partial_z^2 \tilde{p} + i\omega(\alpha + \beta) \tilde{p} \\ \nabla^2 p & \leftrightarrow \partial_z^2 \tilde{p} - \omega^2 (\alpha^2 + \beta^2) \tilde{p} \end{aligned}$$

Appendix C. Calculation of the reflection coefficient

An expression is derived for the reflection coefficient needed to calculate the system's response. The Biot theory is used to describe the wave motion in the rock. In doing so, the particle displacement is considered to be the fundamental unknown. The total displacement in the rock is equal to the sum of the contributions of the transmitted bulk waves, viz; the fast and slow compressional waves and the shear wave. The particle displacement in the rock is connected to the wave motion of the incident wave in the fluid by way of the boundary conditions at the interface.

Transmitted compressional waves

Biot's equations as given in appendix A, are used to describe the wave motion in the porous solid. For the displacement of the solid part in the rock follows from eq. A.26:

$$\nabla^2 \underline{u}_{\pm} - V_{\pm}^{-2} \partial_t^2 \underline{u}_{\pm} = 0 \quad (C.1)$$

The subscripts "+" and "-" refer to the fast and slow compressional waves respectively. Only the displacement due to the fast compressional wave is treated extensively. The derivation of the expression for the displacement due to the slow P-wave proceeds along the same lines.

The Fourier transform of equation (C.1) is :

$$\partial_z^2 \tilde{\underline{u}}_{\pm} + \omega^2 \gamma_{\pm}^2 \tilde{\underline{u}}_{\pm} = 0 \quad (C.2)$$

$$\text{with } \gamma_{\pm} = (V_{\pm}^{-2} - \alpha^2 - \beta^2)^{1/2}$$

The solution to this differential equation is :

$$\tilde{\underline{u}}_{\pm} = C e^{-i\omega\gamma_{\pm}z} \quad (C.3)$$

The solution must remain bounded as $z \rightarrow -\infty$, so $\text{Re } \gamma_{\pm} \geq 0$ and $\text{Im } \gamma_{\pm} \geq 0$.

At the interface the transmitted compressional wave may be expressed as the product of the transmission-coefficient and the downgoing wave in the liquid (the incident wave) :

$$\underline{\tilde{u}} = T \underline{\tilde{U}}_L^i \quad (z = 0) \quad (C.4)$$

The displacements of the downgoing wave in the liquid in the x-, y- and z-direction follow from the transformed equation of motion in the liquid (no volume forces) :

$$\frac{\partial}{\partial z} P_L^i - \rho_L \omega^2 \underline{\tilde{U}}_L^i = 0 \quad (C.5)$$

as:

$$\begin{aligned} \tilde{U}_{Lx}^i &= \frac{i\alpha}{\omega\rho_L} A^i e^{i\omega\gamma_L(h_t - z)} \\ \tilde{U}_{Ly}^i &= \frac{i\beta}{\omega\rho_L} A^i e^{i\omega\gamma_L(h_t - z)} \\ \tilde{U}_{Lz}^i &= -\frac{i\gamma_L}{\omega\rho_L} A^i e^{i\omega\gamma_L(h_t - z)} \end{aligned} \quad (C.6)$$

Combining equations C.3, C.4 and C.6 we arrive for the displacements in the porous medium at :

$$\begin{aligned} \underline{\tilde{u}}_x &= i\alpha T_x \frac{A^i}{\rho_L \omega} e^{i\omega(\gamma_L h_t - \gamma_+ z)} \\ \underline{\tilde{u}}_y &= i\beta T_y \frac{A^i}{\rho_L \omega} e^{i\omega(\gamma_L h_t - \gamma_+ z)} \\ \underline{\tilde{u}}_z &= -i\gamma_L T_z \frac{A^i}{\rho_L \omega} e^{i\omega(\gamma_L h_t - \gamma_+ z)} \end{aligned} \quad (C.7)$$

where T_x , T_y , T_z are the transmission-coefficients in the x-, y- and z-direction.

Since the compressional waves are curl-free, the following equation holds :

$$\nabla \times \tilde{\mathbf{u}}_+ = \mathbf{0} \quad (\text{C.8})$$

which yields $T_y = T_x$ ($= T_+$) and $\gamma_L T_z = \gamma_+ T_+$

The displacements of the solid part of the porous medium due to the fast compressional wave now become :

$$\begin{aligned} \tilde{u}_x^+ &= i\alpha T_+ \frac{A^i}{\omega \rho_L} e^{i\omega(\gamma_L h t - \gamma_+ z)} \\ \tilde{u}_y^+ &= i\beta T_+ \frac{A^i}{\omega \rho_L} e^{i\omega(\gamma_L h t - \gamma_+ z)} \\ \tilde{u}_z^+ &= -i\gamma_L T_+ \frac{A^i}{\omega \rho_L} e^{i\omega(\gamma_L h t - \gamma_+ z)} \end{aligned} \quad (\text{C.9})$$

Equally for the slow compressional wave :

$$(\tilde{u}_x^-, \tilde{u}_y^-, \tilde{u}_z^-) = (i\alpha T_-, i\beta T_-, -i\gamma_L T_-) \frac{A^i}{\omega \rho_L} e^{i\omega(\gamma_L h t - \gamma_- z)} \quad (\text{C.10})$$

The displacements of the fluid part of the porous medium can be calculated using :

$$\tilde{\mathbf{U}}_{\pm} = -G_{\pm} \tilde{\mathbf{u}}_{\pm} \quad (\text{C.11})$$

where G_{\pm} is given by eq. A.27.

Transmitted shear wave

For the particle displacement of the solid part of the rock due to the transmitted shear wave follows from eqs. A.23 and A.24:

$$\partial_z^2 \tilde{\mathbf{u}}_s + \omega^2 \gamma_s^2 \tilde{\mathbf{u}}_s = \mathbf{0} \quad (\text{C.12})$$

with $\gamma_s = (V_s^{-2} - \alpha^2 - \beta^2)^{1/2}$ $\text{Re } \gamma_s \geq 0$; $\text{Im } \gamma_s \geq 0$

At the interface between liquid and porous solid transmission occurs as well as conversion from compressional to shear motion.

Taking this into account and the fact that shear waves are divergence-free ($\nabla \cdot \tilde{\underline{u}}_s = 0$), we get for the solid particle displacements due to the shear waves :

$$\begin{aligned} \tilde{u}_x^s &= -i\gamma_s T_x^s \frac{A^i}{\omega\rho_L} e^{i\omega(\gamma_L h_t - \gamma_s z)} \\ \tilde{u}_y^s &= -i\gamma_s T_y^s \frac{A^i}{\omega\rho_L} e^{i\omega(\gamma_L h_t - \gamma_s z)} \\ \tilde{u}_z^s &= (-i\alpha T_x^s - i\beta T_y^s) \frac{A^i}{\omega\rho_L} e^{i\omega(\gamma_L h_t - \gamma_s z)} \end{aligned} \quad (C.13)$$

where the coefficients T_x^s, T_y^s account for the transmission and conversion at the interface.

The transformed shear-wave displacement of the fluid part of the porous medium follows by using :

$$\tilde{\underline{U}}_s = \frac{\epsilon(\omega) - 1}{\epsilon(\omega)} \tilde{\underline{u}}_s \quad (A.28)$$

Displacement in the solid

The total displacement in the porous solid is obtained by superposition of the contributions of the various waves in the solid.

$$\underline{u} = \underline{u}_+ + \underline{u}_- + \underline{u}_s \quad (C.14)$$

$$\underline{U} = \underline{U}_+ + \underline{U}_- + \underline{U}_s \quad (C.15)$$

Thus, from equations C.9, C.10, C.11 and C.13 the total displacements of the solid and fluid part of the rock are :

$$\begin{aligned}
\tilde{u}_x &= i\alpha T_+ \frac{A^i}{\omega\rho_L} e^{i\omega(\gamma_L h_t - \gamma_+ z)} + i\alpha T_- \frac{A^i}{\omega\rho_L} e^{i\omega(\gamma_L h_t - \gamma_- z)} + \\
&\quad - i\gamma_s T_x^S \frac{A^i}{\omega\rho_L} e^{i\omega(\gamma_L h_t - \gamma_s z)} \\
\tilde{u}_y &= i\beta T_+ \frac{A^i}{\omega\rho_L} e^{i\omega(\gamma_L h_t - \gamma_+ z)} + i\beta T_- \frac{A^i}{\omega\rho_L} e^{i\omega(\gamma_L h_t - \gamma_- z)} + \\
&\quad - i\gamma_s T_y^S \frac{A^i}{\omega\rho_L} e^{i\omega(\gamma_L h_t - \gamma_s z)} \tag{C.16}
\end{aligned}$$

$$\begin{aligned}
\tilde{u}_z &= -i\gamma_+ T_+ \frac{A^i}{\omega\rho_L} e^{i\omega(\gamma_L h_t - \gamma_+ z)} - i\gamma_- T_- \frac{A^i}{\omega\rho_L} e^{i\omega(\gamma_L h_t - \gamma_- z)} \\
&\quad + (-i\alpha T_x^S - i\beta T_y^S) \frac{A^i}{\omega\rho_L} e^{i\omega(\gamma_L h_t - \gamma_s z)}
\end{aligned}$$

$$\tilde{U}_\pm = -G_\pm \tilde{u}_\pm \tag{A.27}$$

$$\tilde{U}_s = \frac{\epsilon(\omega) - 1}{\epsilon(\omega)} \tilde{u}_s \tag{A.28}$$

$$\text{with } \epsilon(\omega) = \epsilon + i[bF(\kappa)/\omega\phi\rho_f] \tag{A.11}$$

$$G_\pm = (V_\pm^2 \rho_{11} - P)/(V_\pm^2 \rho_{12} - Q) \tag{A.27}$$

In order to be able to solve the five transmission- and reflection-coefficients occurring in eq. C.16, five boundary conditions at the liquid/porous solid interface are required. These conditions are :

- The liquid and the porous solid are in contact.

Therefore the normal component of the particle displacement is continuous across the interface.

This gives :

$$\lim_{z \rightarrow 0} [\phi U_z + (1 - \phi)u_z] = \lim_{z \rightarrow 0} [U_{Lz}^i + U_{Lz}^r] \tag{C.17}$$

where ϕ is the porosity.

- The interface cannot produce any forces. It can only transmit them. Thus the normal component of the sum of the stresses in the fluid and solid part of the porous medium must be equal and opposite to the acoustic pressure in the liquid.

This condition leads to :

$$\lim_{z \rightarrow z_0^+} [\sigma_{zz} + S] = \lim_{z \rightarrow z_0^-} (-P_L^i - P_L^r) \quad (C.18)$$

σ_{ij} and S are the stresses in respectively the solid and fluid part.

- The liquid cannot support shear stresses. So the tangential components of the stress in the porous solid must become zero at the interface.

This gives :

$$\lim_{z \rightarrow z_0^+} [\sigma_{xz}] = 0 \quad (C.19)$$

$$\lim_{z \rightarrow z_0^+} [\sigma_{yz}] = 0 \quad (C.20)$$

- The last boundary condition describes the permeability of the interface. Analogous to Deresiewicz and Skalak (1963) who investigated a porous medium/porous medium interface, a partially impermeable interface can be defined.

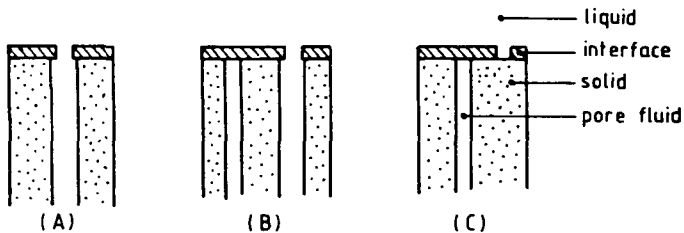


Fig C1. Interface between liquid and solid.

A non-alignment of a portion of the pores, (B), produces an interfacial flow area which is smaller than the one in the porous medium. The effect is equivalent to a partially permeable membrane. Flow through such an interface would result in a pressure drop across the

interface. For the pressure drop in the fluid across the interface may be written :

$$\lim_{z \rightarrow 0^+} P_f - \lim_{z \rightarrow 0^-} P_L = \lim_{z \rightarrow 0} [T\phi(\partial_t U_z - \partial_t u_z)] \quad (C.21)$$

where T is the "surface permeability" i.e. a coefficient of resistance to flow through the surface

Figure (A) above, corresponds to $T = 0$; a situation of open pores.

The other extreme, fig (C), equals equation C.21 with $T = \infty$, or

$$\partial_t U_z - \partial_t u_z = 0 \quad (C.22)$$

In other words it describes a porous solid with completely sealed off pores at the surface.

Equations C.17, C.18, C.19, C.20 and C.21 completely determine the reflection- and transmission coefficients R_L , T_+ , T_- , T_x^S and T_y^S .

For the stresses in the fluid and solid part of the porous medium Biot gives the equations :

$$\sigma_{ij} = (P - 2N) \partial_{ij} \partial_k u_k + N (\partial_i u_j + \partial_j u_i) + Q \partial_{ij} \partial_k U_k \quad (A.1)$$

and

$$\partial_{ij} S = -\phi P_f \partial_{ij} = Q \partial_{ij} \partial_k u_k + R \partial_{ij} \partial_k U_k \quad (A.2)$$

Substitution of equations (A.1) and (A.2) in equations C.17 through C.21 gives, after applying the Fourier transforms, the following equations describing the transmission- and reflection-coefficients in the transformed domain :

$$\begin{aligned}
& T_+ \{ \gamma_+ \phi(G_+ + 1) - \gamma_+ \} + T_- \{ \gamma_+ \phi(G_- + 1) - \gamma_- \} + T_x^S \{ \alpha \left(\frac{\phi}{\alpha(\omega)} - 1 \right) \} + \\
& + T_y^S \{ \beta \left(\frac{\phi}{\alpha(\omega)} - 1 \right) \} + R_L \{ -\gamma_L \} = -\gamma_L
\end{aligned} \tag{C.23}$$

$$\begin{aligned}
& T_+ \left\{ -\frac{(P+Q)}{V_+^2} + 2N(\alpha^2 + \beta^2) + \frac{G_+(Q+R)}{V_+^2} \right\} + T_- \left\{ -\frac{(P+Q)}{V_-^2} + 2N(\alpha^2 + \beta^2) + \right. \\
& \left. + \frac{G_-(Q+R)}{V_-^2} \right\} + T_x^S \{ -2N\alpha\gamma_s \} + T_y^S \{ -2N\beta\gamma_s \} + R_L \{ \rho_L \} = -\rho_L
\end{aligned} \tag{C.24}$$

$$T_+ \{ 2\alpha\gamma_+ \} + T_- \{ 2\alpha\gamma_- \} + T_x^S \{ -\gamma_s^2 + \alpha^2 + \beta^2 \} = 0 \tag{C.25}$$

$$T_+ \{ 2\beta\gamma_+ \} + T_- \{ 2\beta\gamma_- \} + T_y^S \{ -\gamma_s^2 + \alpha^2 + \beta^2 \} = 0 \tag{C.26}$$

$$\begin{aligned}
& T_+ \left\{ \frac{-Q}{V_+^2} + \frac{RG_+}{V_+^2} + T\phi^2 \gamma_+(G_+ + 1) \right\} + T_- \left\{ \frac{-Q}{V_-^2} + \frac{RG_-}{V_-^2} + T\phi^2 \gamma_-(G_- + 1) \right\} + \\
& + T_x^S \left\{ T\phi^2 \frac{\alpha}{\alpha(\omega)} \right\} + T_y^S \left\{ T\phi^2 \frac{\beta}{\alpha(\omega)} \right\} + R_L \{ \phi\rho_L \} = -\phi\rho_L
\end{aligned} \tag{C.27}$$

Appendix D : Transducer characteristics

The acoustic transducers are important components of the data-acquisition system. They determine to a large extent the emitted and received acoustic signals in an experiment. For a correct interpretation of the measurement results it is therefore necessary to know the characteristics of the used transducers. Of importance are: the frequency bandwidth, the transition between the near and far field, and the spread angle of the sound field. The characteristics of the transducers used for the measurements, were determined experimentally and are given in this appendix.

Two pairs of transducers were available for the measurements: one set has a centerfrequency of around .5 MHz, the other of .25 MHz. The transducers of each pair are identical and can be used for emitting as well as receiving acoustic signals. Both sets are non-focussed immersion transducers made by Panametrics. The specifications are:

- 1° - type V391 0.5 MHz element diameter 1.125".
- 2° - type V3469 0.25 MHz element diameter 1".

The radiation pattern produced by the transducers is composed of two zones, the near and far field. The near field is situated close to the transducer, it is characterized by interferences arising from elementary waves originating from different locations at the transducer surface. Further away from the transducer, the sound field becomes smoother until a uniform sound beam is present in the far field. Such a flat, parallel beam is necessary in the transmission measurements to prevent any interference in the refracted sound beam arising from rim effects. Care should be taken to place the rock in the far field of the emitting transducer.

The distance in front of the transducer of the transition between the near and far field, is given by (Krautkrämer, 1983):

$$X = 0.25 D^2 / \lambda \quad (D1)$$

where D = transducer element diameter

λ = wavelength at the given frequency

X = distance in front of the transducer of the transition
between near and far field

The values of X for the two sets of transducers are:

X = 6.7 cm (.5 MHz transducers)

X = 2.7 cm (.25 MHz transducers)

Figures D1 show the acoustic traces recorded in water for the far field (D1a) and the near field (D1b), together with the amplitude spectra. The transmitter was excited by one sinus period with a peak-to-peak voltage of 320 Volt. The trace recorded in the far field is smooth. The trace recorded in the near field (D1b) shows some interference (noticeable on the second positive peak and on the worse damping of the pulse) which is also present in the amplitude spectrum. The center-frequency which follows from the amplitude spectrum in the far field is 464 kHz, with a -6 dB bandwidth of 345 - 602 kHz.

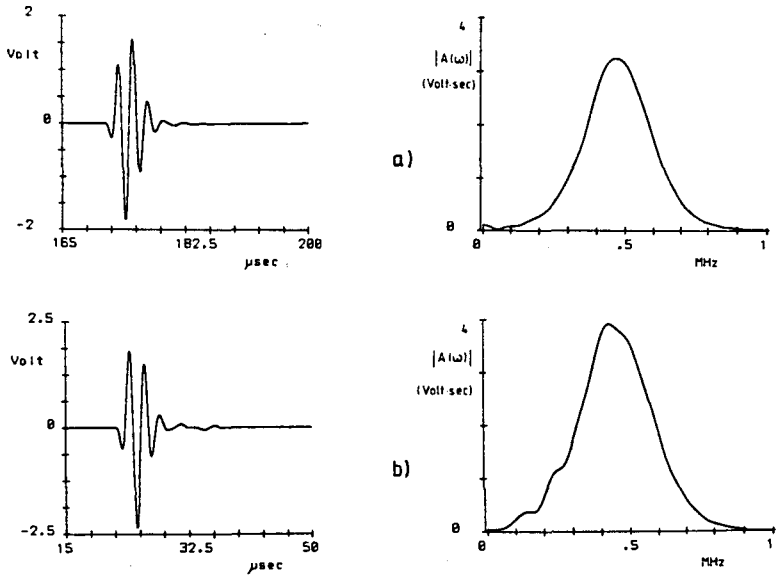


Fig D1. Time trace and amplitude spectrum of acoustic signal in water. 0.5 MHz transducers. Bandpass filter: 50 kHz - 2 MHz.
a) Far field. Transmitter-receiver distance = 25 cm.
b) Near field. Transmitter-receiver distance = 3 cm.

Fig. D2 shows the acoustic trace recorded in water with the .25 MHz transducers, together with its amplitude spectrum. In the time trace a low-frequency (± 80 kHz) oscillation is present which stands out clearly in the spectrum. This prolongs the duration of the pulse to

approximately 30 μsec . Such a long pulse is very unfavourable for the transmission measurements, because it means that the different waves in the rock arrive at the receiver not separated in time. The waves interfere and it is very difficult to determine the properties of the separate waves. Therefore the .5 MHz transducers were used exclusively in the transmission measurements.

Another important transducer characteristic is the sound pressure profile in the far field. Since the results of the transmission measurements largely depend on the refraction of the sound beam at the rock surface, a uniform beam is required in the far field with a small spread angle. The sound beam then has a uniform angle of incidence and refracts uniformly according to Snellius' Law and no distortions of the pulse occur due to interference at the rims of the beam. To check this condition experimentally, the amplitude of the received signal was measured at various locations in front of the transmitter. The measurements were performed with the transmitter at a fixed position. The receiver was stepped away from the transmitter in axial and traverse directions with steps of 5 mm. At each receiver location, the amplitude of the highest negative peak of the pulse was recorded in millivolts. The results are shown in fig D3. The lines connect the positions in front of the transmitter, where equal acoustic pressures were recorded. The plot shows a very uniform sound beam with a small spread angle. Theoretically, the angle is given by (Krautkrämer, 1983):

$$-6 \text{ dB spread angle} = \arcsin (.5 \lambda/D) \tag{D2}$$

This equation gives a value of 4.2° for the spread angle of the .5 MHz transducers. This small value is confirmed by fig.D3 which shows an almost parallel sound beam.

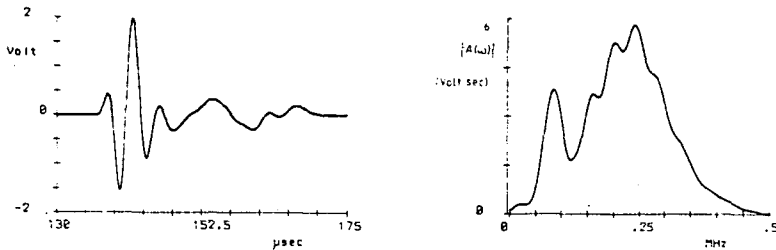


Fig D2. Time trace and amplitude spectrum of acoustic signal in water. 0.25 MHz transducers. Transmitter-receiver distance = 20 cm.

Figure D3 also includes the decrease in amplitude of the pulse due to the attenuation in the water and due to the increased distance from source to receiver. This effect is shown in fig. D4. It shows the measured amplitudes at various transmitter-receiver separations along the transmitter-receiver axis drawn in fig D3. The plot shows a rapid decrease in amplitude at small transmitter-receiver distances. Around the transition zone between near and far field (6.7 cm), the amplitude varies very little and at distances beyond approximately 12 cm the amplitude starts to decrease. The decrease is small. At the ranges at which the transmission measurements are performed (T-R \approx 24 cm), the decrease is equal to - 10 dB/m, which is negligible in comparison with the attenuation of the waves in the porous rock.

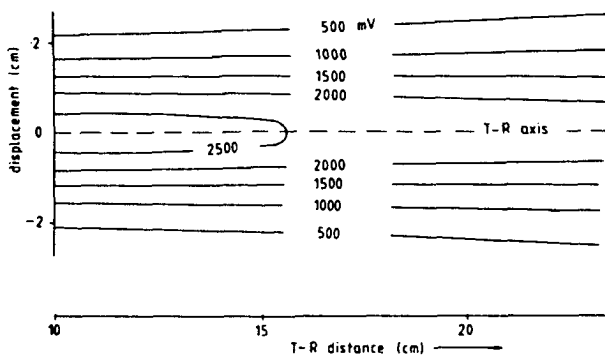


Fig D3. Acoustic pressure in mVolts at various locations in front of the transmitter. (0.5 MHz transducers).

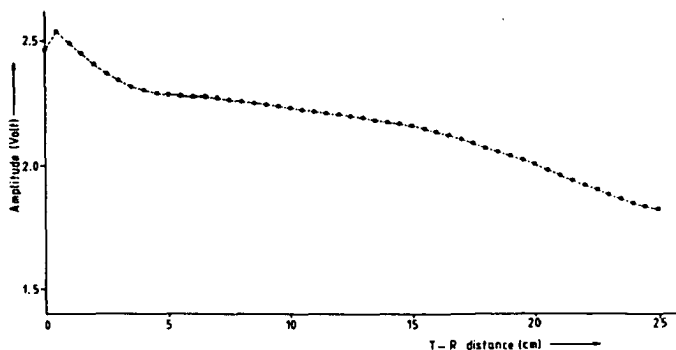


Fig D4. Decrease in amplitude along the T-R axis. (0.5 MHz transducers).

SUMMARY

The present study gives an account of the work carried out on the E.C.-financed project "Acoustic measurements on reservoir rock", which aims at improving the interpretation of acoustic logging in boreholes. Four separate topics are treated: field examples of acoustic logging, the construction of artificial sandstone rock samples, theoretical modelling of the laboratory experiments and the design and construction of the measurement system.

Two field examples are presented concerning wells in which a full waveform log was run. One well is drilled in a shaly sandstone reservoir, the other in a dolomite formation. An extensive petrophysical evaluation is carried out to describe both reservoirs in detail. The standard petrophysical methods fail to account correctly for the shale fraction in the sandstone formation, so a special evaluation procedure had to be developed to give a proper description of this formation. Besides being very tight, the dolomite formation was heavily fractured. Both field examples clearly show the limitations of using field data for acoustic research. Too many rock properties vary between specimens of natural rocks to be able to obtain any more than a broad, general relation between the physical properties and the acoustic response of a rock.

To overcome these problems, a laboratory procedure is developed to construct artificial sandstone samples for research purposes. Loose sand grains are cemented together at the grain contacts, thus forming a porous sandstone closely resembling natural reservoir formations. The consolidation method produces very homogeneous rock samples. The rock properties are well-defined and can be varied within certain limits. The method does not restrict the dimensions of the samples.

Three types of cement are investigated:

- 1° silica cement formed by the reaction of silicontetrachloride with an irreducible water saturation in the loose sand pack.
- 2° silica cement obtained from methylsilicate
- 3° araldite cement, an epoxy resin.

Both silicontetrachloride and araldite produce well-consolidated rocks. The synthetic samples exhibit petrophysical properties similar to natural reservoir rocks. The use of methyl-silicate results in very brittle samples and is not favourable.

A mathematical model is developed which predicts the received acoustic signals in the measurements. The configuration of the model is similar to the set-up used in the actual experiments. It consists of a flat porous sandstone submerged in a liquid. The emitting and receiving transducers are located in the liquid above the rock. The propagation of the waves in the porous rock is described by the Biot theory. Two distinct cases are treated:

- 1° the full frequency range including dispersion and attenuation of the bulk waves due to fluid flow in the pores.
- 2° the high frequency limit of the Biot theory.

In the latter case, energy dissipation becomes negligible and the porous rock effectively reduces to a loss-less medium.

Calculated microseismograms are presented for different measurement configurations and for different types of rock. The amplitude with which the surface wave is generated appears to be sensitive to the permeability of the rock.

A data acquisition system was built for performing high frequency acoustic experiments. It is a multi-purpose set-up, suitable for transmission as well as refraction measurements.

Both transmission and refraction measurements are performed on a range of artificial sandstone rock samples under atmospheric conditions. The transmission measurements provide a relatively easy way to determine the properties of the bulk waves in the porous rocks, whereas the refraction measurements more closely resemble actual logging.

SAMENVATTING

De inhoud van deze studie wordt gevormd door de neerslag van het onderzoek uitgevoerd in het kader van het door de E.G. gefinancierde project "Akoestische metingen aan reservoirgesteente", met als doel het verbeteren van de interpretatie van akoestische metingen in boorgaten.

Er komen vier verschillende onderwerpen aan de orde:

praktijkvoorbeelden van akoestische metingen in boorgaten, de constructie van kunstmatige zandsteenmonsters, het ontwikkelen van een theoretisch model voor de akoestische experimenten en ontwerp en constructie van de meetopstelling.

Er worden twee praktijkvoorbeelden van putten waarin een volledige akoestische meting werd verricht, behandeld. De ene put werd geboord in een kleihoudend reservoirgesteente, de andere in een dolomietformatie. Beide formaties worden gedetailleerd beschreven aan de hand van een diepgaande petrofysische evaluatie. De normale evaluatieprocedure blijkt voor de kleihoudende formatie geen correct kleigehalte op te leveren. Er moest dus een speciale evaluatiemethode ontwikkeld worden om deze formatie juist te kunnen beschrijven. De dolomietformatie was niet alleen zeer compact, maar daarnaast ook sterk gebroken. Beide praktijkvoorbeelden geven duidelijk aan, welke beperkingen het gebruik van praktijkgegevens oplevert bij akoestisch onderzoek. Er zijn teveel verschillende gesteente-eigenschappen per monster om hieruit meer af te kunnen leiden dan een zeer algemene relatie tussen de fysische eigenschappen en het akoestisch gedrag van gesteenten.

Om aan deze problemen te ontsnappen, wordt in het laboratorium kunstmatig zandsteen gemaakt. Losse zandkorrels worden aan elkaar gecementeerd op de korrelcontacten, zodat een poreus zandsteen wordt verkregen dat sterk gelijkt op natuurlijk zandsteen. Deze consolidatiemethode produceert zeer homogene zandsteenmonsters. De gesteente-eigenschappen zijn precies gedefinieerd en kunnen gevarieerd worden. De afmetingen van de monsters zijn in principe onbeperkt.

Drie soorten cement zijn hierbij onderzocht:

- 1 silica cement, gevormd door de reactie van siliciumtetrachloride met capillair gebonden water in het losse, gecompacteerd zand
- 2 silica cement, verkregen met behulp van methylsilicaat
- 3 araldiet cement, een harsachtige substantie

Zowel de eerste als de derde methode leveren een goed geconsolideerd gesteente. De synthetische monsters vertonen petrofysische eigenschappen vergelijkbaar met die van natuurlijk reservoirgesteente. De tweede methode leverde brokkelige monsters.

Er is een theoretisch model ontwikkeld, dat de opgevangen akoestische signalen bij de metingen voorspelt. De configuratie van het model lijkt de opzet van de werkelijke experimenten. Deze bestaat uit een plat stuk poreuze zandsteen, ondergedompeld in een vloeistof. Uitzendende en ontvangende transducenten zijn in de vloeistof boven de steen geplaatst. De voortplanting van de golven in het poreuze gesteente wordt beschreven met behulp van de theorie van Biot. Twee verschillende gevallen komen aan de orde:

- 1 het volledige frequentiebereik met inbegrip van dispersie en demping tengevolge van vloeistofstroming in de poriën
- 2 de hoge frequentielimiet van de theorie van Biot

In het laatste geval is de demping te verwaarlozen.

Berekende microseismogrammen worden gegeven voor verschillende meetopstellingen en verschillende gesteentetypes. De amplitude waarmee de oppervlaktegolven worden opgewekt blijkt afhankelijk van de permeabiliteit van het gesteente.

Een meetopstelling werd gebouwd om ultrasone akoestische experimenten uit te voeren. De opstelling is multi-functioneel en kan zowel voor transmissie- als refractiemetingen gebruikt worden.

Beide types metingen worden uitgevoerd op een serie gesteentemonsters onder atmosferische omstandigheden. De transmissiemetingen maken het mogelijk om op een eenvoudige manier de eigenschappen van de bulk waves in poreuze gesteenten vast te stellen, terwijl de refractiemetingen meer op het normale "loggen" lijken.

NAWOORD

Graag wil ik op deze plaats een woord van dank richten tot al degenen die hebben bijgedragen tot de totstandkoming van dit proefschrift.

Zonder de constante steun en aanmoediging van mijn begeleider Joop van Baaren en de technische ondersteuning van Karel Heller, was het hele onderzoek nooit uitgevoerd.

Zonder de inzet van de promotoren, prof. van der Vuurst de Vries en prof. Ziolkowski, waren niet alle puntjes op de i's gezet.

Zonder mijn vrouw Hella, die doorlopend de tekst van het proefschrift heeft gecorrigeerd en die assisteerde bij het typewerk, was het onderzoek nooit beschreven.

Zonder de hulp van de studenten: H. Koeneman, F. Seegers, M. Schiet, E.-J. Waller, D. Bax, J. Blank en G.-J. Romijn waren bepaalde details niet zo grondig uitgewerkt.

Zonder de fotograaf T. Steenhuis was dit proefschrift zonder illustraties gebleven.

Daarom dank ik alle bovengenoemden voor hun medewerking en steun, en alle niet genoemde leden van de vakgroep Petroleumwinning en Technische Geofysica voor de gezelligheid en vriendschap die ik deze jaren van hen heb ondervonden.

Curriculum vitae

2 jan 1958 geboren te Zeist

1976 diploma gymnasium β
Rijksscholengemeenschap te Heerenveen

1984 diploma mijnbouwkundig ingenieur
afstudeerrichting petroleumwinning
TU Delft

1984 3e prijs European Student Paper Contest
Europec conference, London

1984 Petroleumtechniekprijs, KIVI

1984-1988 wetenschappelijk assistent aan de TU Delft, werkzaam
aan het project: "Acoustic measurements on core material".
Dit proefschrift vormt de neerslag van het werk aan dit
onderzoek.